A tale of serendipity

Quasi-periodic oscillations in pulsating ultraluminous X-ray sources and a search for new candidate X-ray pulsators

Scuola di Dottorato di Tor Vergata

PhD programme in Astronomy, Astrophysics and Space Science (XXXVII cycle)

Matteo Imbrogno

ID number 0308515

Supervisor

Prof. Gian Luca Israel
INAF-OAR
Tor Vergata University of Rome

Co-Supervisor

Prof. Francesco Tombesi
Tor Vergata University of Rome

Coordinators

Prof. Francesco Piacentini

Prof. Giuseppe Bono

Dr. Oscar Straniero

Academic Year 2023/2024

Thesis not yet defended

A tale of serendipity

PhD thesis. Sapienza University of Rome and Tor Vergata University of Rome.

This thesis has been typeset by LaTeX and (a slightly modified version of) the Sapthesis class.

Version: October 27, 2024

Author's email: matteo.imbrogno@inaf.it

Abstract

In the past 10 years, the discovery of pulsating ultraluminous X-ray sources (PULXs) has revealed that accreting neutron stars (NSs) can shine at extreme luminosities, well above their Eddington limit. This finding has caused a shift in the ULX paradigm. Previously thought to consist solely of intermediate-mass black holes, the current view is that the ULX population is more heterogeneous, potentially dominated by NSs accreting at super-Eddington rates, posing significant challenges to our understanding of the physics of accretion onto compact objects. Many questions about this class of sources remain open: Are the extreme luminosities of these NSs really super-Eddington or is geometrical beaming playing a significant role? If they are indeed accreting at super-Eddington rates, how can they sustain this regime over extended periods of time? What is the fraction of ULXs powered by accreting NSs? Are they an exception or do they represent a common X-ray binary phase? Each new (observational and theoretical) insight into their complex phenomenology can bring us closer to a deeper understanding of these fascinating sources.

Given their rarity (only 6 PULXs are known, 11 taking into account transient PULXs too, out of almost 2000 ULXs), every new identified PULX can carry vital information on the whole population. A possible way to achieve this goal is by searching in the archives of X-ray missions with good imaging and timing capabilities. As these archives become larger and larger, a data mining approach, with a systematic and automated search for sources showing coherent pulsations, provides the most efficient method to perform such an analysis in a reasonable time. NGC 7793 P13 and NGC 5907 ULX-1 are two examples of PULXs discovered thanks to data mining projects in the *XMM-Newton* archive. In the process, serendipitous sources (not only PULXs) are always behind the corner, sources that otherwise would have been lost in the archives.

Both the study of PULXs and the search for new X-ray pulsators through data mining have defined the course of my Ph.D. and are the subject of this thesis. In Chap. 1 I first introduce the class of compact objects and the basics of accretion physics, and then describe the main properties and the open questions about (P)ULXs. In Chap. 2 I report my discovery of mHz-QPOs in the flux of two PULXs at super-Eddington luminosities. These mHz-QPOs could represent a signature of super-Eddington accretion and a turning point in our comprehension of PULXs. I describe the data mining project thanks to which NGC 7793 P13 pulsations have been discovered in Chap. 3. I am currently involved in the continuation of this project aimed at searching for previously unidentified X-ray pulsators in the newly published *XMM-Newton* observations. During one of these searches, I discovered a new pulsar in the Large Magellanic Cloud. This source is likely a new candidate magnetar, only the third known outside our Galaxy. I report the details of the discovery in Chap. 4. Finally, I summarise and draw the conclusions of the work of these three years in Chap. 5, where I also outline additional works in progress and possible new directions for my research. A few examples of these and other works I have been involved in are further discussed in Appendix A and Appendix B.

Contents

Chapter 1

Introduction

"Begin at the beginning," the King said, very gravely,
"and go on till you come to the end: then stop."

Lewis Carroll, *Alice in Wonderland*

This chapter gives an overview of the astrophysical sources I have been studying in the last 3 years. In particular, I lay the foundations by introducing the class of compact objects, how these sources can emit in the X-ray band through accretion of matter, and the maximum luminosity they can reach according to the standard theory. I cover only the basics, but I refer the interested reader to the reviews and papers cited in the following sections. The (pulsating) ultraluminous X-ray sources, which represent the main topic of the first half of this thesis, are introduced starting from Sect. 1.4. Unless otherwise stated, all the quantities in this thesis are expressed in the cgs system.

1.1 The class of compact objects

Compact objects, namely white dwarfs (WDs), neutron stars (NSs) and black holes (BHs, see Shapiro and Teukolsky 1986), represent the final stage in the life of most stars[1]. The compactness of these objects arises from the fact that the progenitor star will collapse under its own weight once its nuclear reservoir has run out.

In the case of WDs and NSs, the collapse ends in a new stable configuration. If the initial mass of the star is $0.08\,\mathrm{M}_\odot \lesssim M \lesssim 8\,\mathrm{M}_\odot$ (where $\mathrm{M}_\odot \simeq 1.99 \times 10^{33}\,\mathrm{g}$ is the mass of the Sun) the collapse is halted by the electron degeneracy pressure (Fowler, 1926). The outcome is a WD, with mass $M_{\mathrm{WD}} \sim 1\,\mathrm{M}_\odot$ and radius $R_{\mathrm{WD}} \sim 5000\,\mathrm{km}$. A star with $8\,\mathrm{M}_\odot \lesssim M \lesssim 30\,\mathrm{M}_\odot$, on the other hand, will end its life with a core mainly composed of Fe, Ni, Co. At that point, the nuclear reactions chain ends, the outer layers of the stars will be expelled in a supernova explosion and the core will collapse, until the onset of the neutron degeneracy pressure and the birth of a NS (Baade and Zwicky, 1934). Typical masses and radii are $M_{\mathrm{NS}} \sim 1.4\,\mathrm{M}_\odot$ and $R_{\mathrm{NS}} \sim 10\,\mathrm{km}$. The matter inside a NS can reach densities $\rho_{\mathrm{NS}} > \rho_{\mathrm{nuc}} \simeq 10^{14}\,\mathrm{g\,cm^{-3}}$,

others would say 25

others would say 11-12

[1] I refer the reader interested in stellar evolution to the book by Kippenhahn et al. (2013).

where $\rho_{\rm nuc}$ is the density of an atomic nucleus. The structure of a NS is described by the Tolman-Oppenheimer-Volkoff equations (Tolman, 1939; Oppenheimer and Volkoff, 1939), whose solution depends on the equation of state of the matter (which describes the pressure P as a function of the density ρ) within the NS itself. Unfortunately, the equation of state of the matter at these extreme regimes is still unknown and different possibilities have been proposed (for a collection of possible equations of states, see e.g. Baym et al., 2018, and references therein). For more massive stars, the collapse cannot be halted and a BH is born. A BH has no solid surface, but one can identify its boundaries with the so-called event horizon, within which the gravitational field is so intense that even electromagnetic radiation cannot escape. In the case of non-rotating BH, the radius of this surface is equal to the Schwarzschild radius R_S (Schwarzschild, 1916):

$$R_S = \frac{2GM}{c^2} \simeq 3\frac{M}{M_\odot}\,\mathrm{km} \tag{1.1}$$

where G is the gravtiational constant, and c is the speed of light.

A consequence of the compactness of these objects is the presence of an extreme gravitational field in their proximity. To measure the intensity of these fields we can compute the surface gravity, equal to $GM/(c^2R)$, where M and R are the mass and the radius of the compact object, respectively. For a BH, this ratio is $\sim$1, while for NSs and WDs we obtain $\sim 10^{-1}$ and $\sim 10^{-4}$, respectively. For a comparison, the Sun has a surface gravity $\sim 10^{-6}$.

WDs and NSs, finally, are also characterised by moderate-to-extreme magnetic fields, with $B \sim 10^4 - 10^9\,\mathrm{G}$ and $B \sim 10^8 - 10^{15}\,\mathrm{G}$, respectively (Ferrario et al., 2015; Kaspi, 2010). The origin of these intense fields in WDs and NSs is still unknown, with possible models involving magnetic flux freezing of the progenitor star, thermomagnetic effects and dynamo effects (see e.g. Romani, 1990; Ferrario and Wickramasinghe, 2005, and references therein). Some isolated NSs in the high-B tail are the astrophysical sources with the most intense magnetic fields in the known universe. The emission of these sources, known as magnetars (Duncan and Thompson, 1992; Esposito et al., 2021), is thought to be powered (for the most part) by their internal magnetic fields, which can be as high as $10^{14}\,\mathrm{G} \lesssim B \lesssim 10^{16}\,\mathrm{G}$. A more in-depth discussion about this class of NSs can be found in Chap. 4, where I present the case of a new candidate magnetar discovered during my PhD work.

The existence of NSs was confirmed in 1967 by the then PhD student Jocelyn Bell with the detection of coherent pulsations at a period $P \sim 1\,\mathrm{s}$ in the radio band (Hewish et al., 1968), which can be produced only by a rapidly rotating NS, a so-called pulsar[2]. The first identification of a pulsar in the X-ray band would follow a few years later, with the discovery of pulsations from Cen X-3 (Giacconi et al., 1971). The X-ray flux from NSs and WDs often shows coherent pulsations which arise from the spin motion of the compact object itself. NSs can spin at periods as short as $P \sim 1\,\mathrm{ms}$ (the so-called millisecond pulsar; for a review, see Manchester 2017) thanks to their extreme compactness, which allows them to spin so fast without breaking up.

[2]The first observation of a NS is actually the discovery in X-ray band of Sco X-1 in 1962 (Giacconi et al., 1962). The true nature of the source, however, was not recognised due to the lack of spin pulsations in the flux.

1.2 Accretion-powered X-ray sources: an introduction to the emission mechanisms of X-ray binaries

The study of the sky in the X-ray band has provided a wealth of information on compact objects since the first detection of X-ray sources from outside our Solar System (Giacconi et al., 1964). There are various mechanisms that can lead a compact object to emit mainly in the X-ray band. Here, I will focus on compact objects in binary systems whose X-ray emission arises from the accretion of matter from a companion star[3], i.e. the accretion-powered X-ray sources. These systems are classified either as an X-ray binary (XRB) or a cataclysmic variable (CV) if the accretor is a BH/NS or a WD, respectively. Both XRBs and CVs are powered by the release of gravitational energy from the infalling matter. I will focus on XRBs, although most of the concepts illustrated below are also valid for CVs.

There are two possible mechanisms that can lead a compact object to accrete matter from the companion. A key role is played by the effective gravitational potential in the binary system, which can be written as

$$\Phi = -\frac{GM_1}{r_1} - \frac{GM_2}{r_2} - \frac{\Omega_{\rm orb}^2 r_3^2}{2} \tag{1.2}$$

where r_1 (r_2) is the distance from the star with mass M_1 (M_2), r_3 is the distance to the centre of mass of the system and $\Omega_{\rm orb}$ is the orbital angular velocity (see Section 16.4 of Tauris and van den Heuvel (2006)). Fig. 1.1 shows the equipotential surfaces at the equatorial plane for a binary system with $M_1 = 15\,{\rm M}_\odot$ and $M_2 = 7\,{\rm M}_\odot$. The Roche lobe is identified as the equipotential surface that crosses the first Lagrangian point L_1. In an XRB/CV, the radius of the companion Roche lobe can be expressed as

$$\frac{R_L}{a} = \frac{0.49q^{2/3}}{0.6q^{2/3} + \ln 1 + q^{1/3}} \tag{1.3}$$

where R_L is the radius of the companion's Roche lobe, a the orbital separation between the companion and the accretor, and $q = M_{\rm comp}/M_{\rm acc}$ is the mass ratio of the binary system (Eggleton, 1983).

Depending on the evolutionary stage of the companion, the latter may or may not fill its Roche lobe. In the first case, typical of companions on the main sequence, accretion can happen if winds are launched from the companion itself and the compact object intercepts some of this matter (radial/wind-fed accretion, see Bondi, 1952). If, on the other hand, the companion fills its Roche lobe, the matter can flow through L_1 onto the accretor (Roche-lobe overflow). The infalling matter will have a non-zero (specific) angular momentum and will spiral onto the compact object forming an accretion disk. Fig. 1.2 shows a depiction of a compact object (in this case a NS) accreting from a companion star through a disk.

Historically, wind-fed accretion has been associated with XRBs with a high-mass companion ($M \gtrsim 5\,{\rm M}_\odot$), known as high-mass X-ray binaries (HMXBs, Walter et al. 2015). Evolved low-mass ($M \lesssim 1\,{\rm M}_\odot$) companions, on the other hand, can enter the (super-)giant phase and fill their Roche lobe. XRBs with such a companion

[3]For simplicity, from now on I will refer to the star from which the compact object is accreting as the companion.

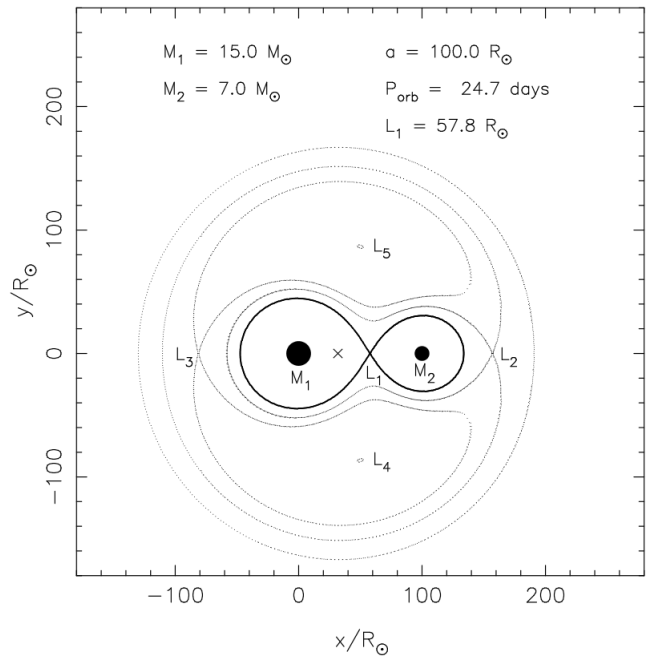

Figure 1.1. Equipotential surfaces in the equatorial plane for an example binary system. The parameters of the system are reported in the plot. The cross represents the centre of mass. The bold black line represents the Roche lobes of the two stars. L_i, with $i = 1, 2, 3, 4, 5$, represents the i-th Lagrangian point. Plot taken from Tauris and van den Heuvel (2006).

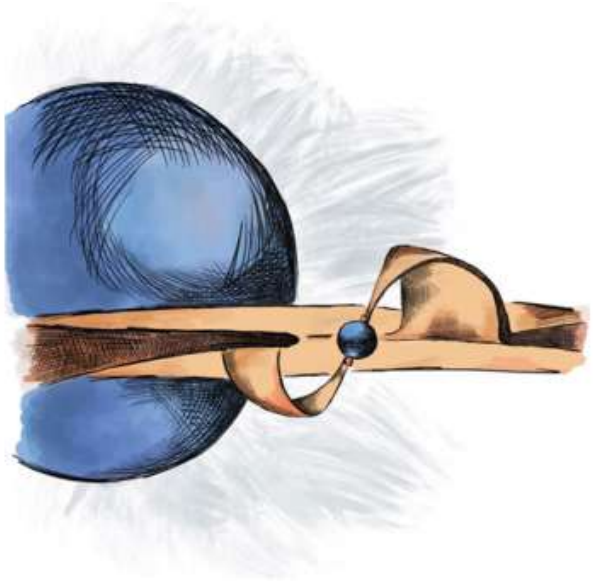

Figure 1.2. Drawing of a NS accreting from a companion through a disk. Graph from Tsygankov et al. (2022).

are known as low-mass XRBs (LMXB, Vaughan et al. 1994). However, we now know that the boundaries between the two systems are more blurred than previously thought, with various examples of HMXBs (LMXBs) showing signs of Roche-lobe overflow (wind-fed accretion). I will focus on the Roche-lobe overflow, responsible for the production of accretion disks. This is the channel through which (pulsating) ultraluminous X-ray sources accretes matter from their companions.

1.2.1 Accretion onto non-magnetised compact objects

The basis of the physics of disk accretion were layed in the early 1970s by the seminal works of Shakura (1973) and Shakura and Sunyaev (1973). Let us consider an element of the disk with mass m falling onto the compact object from infinity with a non-zero angular momentum $L \neq 0$. I will start from a simple case where the accretor is either a BH or a non-magnetic WD/NS. The disk is assumed to be both geometrically and optically thin, i.e. $h \ll r$, where h is the height of the disk at distance r, and $\tau \ll 1$, where τ is the optical depth. The matter will spiral onto the accretor. The motion can be approximated by a sequence of quasi-Keplerian orbits, with

$$v_{\rm K} = \sqrt{\frac{GM}{r}} \tag{1.4}$$

where $v_{\rm K}$ is the Keplerian velocity of the element of the disk, M is the mass of the accretor, and r the distance of the element of the disk from the accretor. The cause of the inspiral is the viscosity between adjacent rings of matter, described by the α parameter in Shakura and Sunyaev (1973). The matter contained in a disk at a distance r will be faster than the matter at a distance $r + \delta r$: the interaction between the two rings will produce a flux of angular momentum towards the outer zone of the disk and the matter at distance r will move to a distance $r - \delta r$ (Vietri et al., 2007).

During this motion, both the angular momentum and the energy of the particle:

$$L = m v_{\rm K} r = m\sqrt{GMr} \tag{1.5}$$

$$E = \frac{1}{2} m v_{\rm K}^2 - \frac{GMm}{r} = -\frac{GMm}{2r} \tag{1.6}$$

will change. During the infall towards the accretor, the particle will lose an energy $E = GMm/(2R)$. For a NS or a WD, R is the radius of the object, while in the case of a BH it is the radius of the innermost stable circular orbit (ISCO) $R_{\rm ISCO} = 6GM/c^2$, where c is the speed of light (Misner et al., 1973). In the case of a NS or a WD, once the particle reaches the surface it will release an additional energy $E = GMm/(2R)$ in the form of electromagnetic radiation. At the same time, the particle will impart its angular momentum $m\sqrt{GMR}$ to the accretor, which will start spinning faster. In this case, the source is said to be spinning-up.

for a non-rotating BH

This simplified description allows us to explain why this mechanism is particularly efficient in the case of accretion onto a compact object. The total energy released by the infalling matter is $E_{\rm TOT} = GMm/R$, which corresponds to a luminosity

$$L_{\rm X} = \frac{GM\dot{m}}{R} \tag{1.7}$$

where $\dot{m}$ is the accretion rate. The efficiency of the emission of radiation will be equal to

$$\epsilon = \frac{L_{\rm X}}{\dot{m}c^2} = \frac{GM}{Rc^2} \tag{1.8}$$

which depends only on the mass M and radius R of the accretor. For a NS $\epsilon \sim 0.1$, while in the case of an accreting WD $\epsilon \sim 10^{-4}$. In the case of an accreting BH the computation is complicated by the fact that the rotation of the BH induces additional effects to the surrounding spacetime (Kerr, 1963). It can be shown, however, that depending on the BH angular momentum $\epsilon \simeq 0.1 - 0.43$. Accretion onto a main-sequence star like the Sun would not be as efficient, since in that case $\epsilon \sim 10^{-6}$. We can also explain why the photon emission peaks in the X-ray band. If we assume that most of the energy is released in the form of black-body radiation, then

$$L_{\rm X} = 4\pi R^2 \sigma T^4 \tag{1.9}$$

where $\sigma = 5.67 \times 10^{-5}\,{\rm erg\,cm^{-2}\,s^{-1}K^{-1}}$ is the Stefan-Boltzmann constant and T is the temperature of the matter. Equating eq. (1.9) and eq. (1.7) and considering typical values, e.g., of the mass and radius of a NS, we obtain $T \sim 10^7\,{\rm K}$. At these temperatures, the peak of the black-body emission is at $E \sim 1\,{\rm keV}$, i.e. in the soft X-ray band.

1.2.2 Accretion onto magnetised compact objects

In a real-life scenario, the non-magnetised accretor assumption can be applied only to BHs. In the case of a WD or a NS, a more accurate description of the accretion process must take into account the presence of intense magnetic fields that define a region, the magnetosphere, within which the matter inflow is strongly influenced by the magnetic field lines (for a review, see e.g. Henrichs, 1983). I will assume a dipolar configuration of the magnetic fields. Although in the case of NSs more complex configurations are expected (see e.g. Kalapotharakos et al., 2021; Kong et al., 2022), at distances $r \gg R_{\rm NS}$ the dominant component is the dipole. This is a result of the less steep dependence of the dipole component on the distance r ($B_{\rm dip} \propto r^{-3}$) with respect to higher order multipoles, where $B_{\rm n} \propto r^{-n-2}$ and $n \geq 2$. Although I will focus on NSs, the general framework depicted in this section works also for WDs.

The magnetosphere is defined by the magnetospheric radius, i.e. the radius at which the magnetic pressure of the NS magnetic field and the ram pressure of the infalling matter are equal. It can be shown that this quantity is equal to:

$$R_{\rm m} = 3.3 \times 10^7 \frac{\xi}{0.5} B_{12}^{4/7} L_{39}^{-2/7} R_6^{10/7} M_{1.4}^{1/7}\,{\rm cm} \tag{1.10}$$

where B is the NS magnetic field strength[4], L its X-ray luminosity, R its radius, and $M_{1.4}$ its mass in units of $1.4\,{\rm M_\odot}$. ξ is a parameter that takes into account the geometry of the accretion flow and in the case of an accretion disk is ≈0.5 (Ghosh and Lamb, 1979b; Wang, 1987; Campana et al., 2018). $R_{\rm m}$ depends not only on

[4]Unless otherwise specified, hereafter I adopt the notation $Q_X = Q/10^X$ to express a quantity Q in the cgs system.

the intensity of the magnetic field (the higher B, the higher R_m), but also on the luminosity, and therefore, through eq. (1.7), on the accretion rate $\dot{m}$: the higher the accretion rate, the lower R_m.

In the presence of a magnetosphere, the particle with mass m will release an energy $GMm/(2R_\mathrm{m})$ during the inspiral until it reaches the magnetosphere, where the particle will release an additional energy $GMm/(2R_\mathrm{m})$. Within R_m the particle is forced to follow the magnetic field lines until it reaches the surface of the accretor, where it releases an additional energy

$$E = GMm\left(\frac{1}{R} - \frac{1}{R_\mathrm{m}}\right) \tag{1.11}$$

in the form of radiation. If $R_\mathrm{m} \gg R$ (as it is often the case with magnetised NSs), the difference with the non-magnetised scenario is negligible.

The transfer of angular momentum from the disk to the accretor, on the other hand, is now more complex. The details of the process depend on the interaction between the magnetic field lines and the accretion disk, which in turn depends on the configuration of the magnetic field and the interactions within the elements of matter in the disk. Unfortunately, the details of these processes are still evading us.

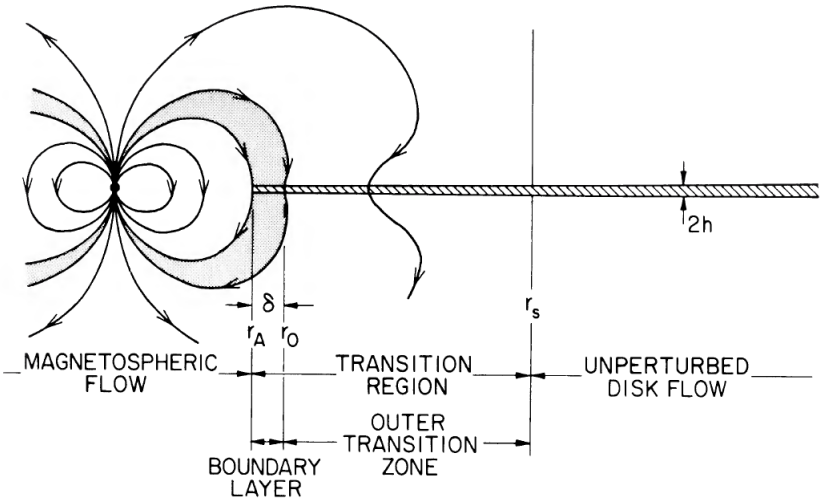

Figure 1.3. Graphical depiction of the disk and the magnetosphere configuration in the model proposed in Ghosh and Lamb (1978). r_A is the magnetospheric radius, labelled in this thesis as R_m.

For the purpose of illustration, I will describe the model proposed by Ghosh and Lamb (Ghosh et al., 1977; Ghosh and Lamb, 1978, 1979a,b, see also Henrichs 1983 for an overview on the model). Fig. 1.3 shows a schematic view of the proposed model in the case of an accreting NS. The disk is assumed as described by Shakura and Sunyaev (1973), i.e. geometrically thin ($h \ll r$). Three regions are identified:

- $r \gg r_s$: r_s is the distance from the NS beyond which the magnetic field is completely screened by the currents produced by the infalling matter. In this region, purely Keplerian orbits with no influence from the magnetic field can be assumed.

- $R_{\rm m} < r < r_s$: this is a transition zone, where the influence of the magnetic field grows stronger and stronger.
- $r < R_{\rm m}$: within the magnetosphere, the matter is forced to flow along the magnetic field lines.

There is another quantity introduced in the model, i.e. the corotation radius. This is the distance from the NS where the angular Keplerian velocity of the accreting matter is equal to the angular velocity of the NS $\Omega_{\rm NS} = 2\pi/P$, where P is the spin period of the NS:

$$v_{\rm K} = \Omega_{\rm NS} r \tag{1.12}$$

Solving for the radius, we obtain:

$$R_{\rm c} = \left(\frac{GM}{\Omega_{\rm NS}^2}\right)^{1/3} \simeq 1.5 \times 10^8 \left(\frac{M}{\rm M_\odot}\right)^{1/3} P^{2/3}\,{\rm cm} \tag{1.13}$$

where P is expressed in units of seconds. For $r < R_{\rm c}$, matter orbits with an angular velocity higher than $\Omega_{\rm NS}$: the magnetic field lines that interact with the disk in this region are dragged by the matter, which will accelerate their rotation. Therefore, they will contribute to spin up the NS itself. For $r > R_{\rm c}$, on the other hand, the magnetic field lines are slowed down by the interacting matter and will slow down the spin motion of the NS. In this case, we refer to this contribution as a spin-down. For $r > r_{\rm s}$, the magnetic field lines are not influenced by the disk. According to the dominant component, therefore, the NS will either spin up or spin down.

Let us first consider the case in which the magnetic field is strong and/or the accretion rate low: in this case, $R_{\rm m} > R_{\rm c}$. When the matter reaches the magnetosphere it will be accelerated to a velocity higher than the one given by its Keplerian orbit. The centrifugal force will dominate, the matter will be expelled and the X-ray luminosity of the source will drop. The source is said to be in the propeller regime (Illarionov and Sunyaev, 1975; Lovelace et al., 1999) and the luminosity drop jump is $\Delta L_{\rm X} \sim 170 P^{2/3}$ (Corbet, 1996). The magnetosphere will be decelerated by the interaction with the disk and the NS will spin down.

On the other hand, for $R_{\rm m} \ll R_{\rm c}$ the spin-down component is negligible and the accretor will spin up. Assuming an accretion rate $\dot{m}$ and a specific angular momentum for the accreting matter l, the NS angular momentum will evolve according to

$$\frac{\rm d}{{\rm d}t}(I\Omega_{\rm NS}) = I\dot{\Omega}_{\rm NS} = \dot{m} l \tag{1.14}$$

where I neglected the first derivative of the NS moment of inertia I. If the disk extends all the way down to $R_{\rm m}$ and assuming that on the disk's inner radius the matter orbits at the Keplerian velocity given by eq. (1.4), the specific angular momentum of the matter at the magnetospheric radius is equal to

$$l = R_{\rm m} v_{\rm K}(R_{\rm m}) = \sqrt{GMR_{\rm m}} \tag{1.15}$$

This is the angular momentum per units of mass that will be transferred to the accreting NS. Assuming a constant accretion rate $\dot{m}$, the NS will spin up on a

timescale τ equals to

$$\frac{1}{\tau} = -\frac{\dot{P}}{P} = 8.5 \times 10^{-5} \left(\frac{M}{M_\odot}\right)^{-3/7} R_6^{6/7} L_{37}^{6/7} \mu_{30}^{2/7} I_{45}^{-1} P\,\mathrm{yr}^{-1} \tag{1.16}$$

where $I_{45} \simeq 1$, $\mu = BR^3$ is the magnetic dipole moment and $\dot{P}$ is the spin period derivative. A higher (lower) luminosity, i.e. a higher (lower) accretion rate, corresponds to a higher (lower) spin-up rate $\dot{P}$. Moreover, given P, $\dot{P}$ and L_X, one can derive the magnetic field strength B.

In their papers, Ghosh and Lamb showed that in the general case:

$$\frac{\mathrm{d}}{\mathrm{dt}}(I\Omega_\mathrm{NS}) = I\dot{\Omega}_\mathrm{NS} = \dot{m}ln(\omega_s) \tag{1.17}$$

where

$$\omega_s = \frac{\Omega_\mathrm{NS}}{\Omega_\mathrm{K}(R_\mathrm{m})} = \left(\frac{R_\mathrm{m}}{R_\mathrm{c}}\right)^{3/2} \tag{1.18}$$

is the fastness parameter. $n(\omega_s)$ is a dimensionless, monotonically-decreasing function that is equal to 1.4 for $\omega_s \ll 1$ and negative for $\omega_s \gtrsim 0.5$. Fast rotators (with $\omega_s \simeq 1$) can therefore show spin-down phases even during accretion, since $n(\omega_s \simeq 1) < 1$ and both $\dot{m}$ and l in eq. (1.17) are positive (see Ghosh and Lamb, 1979b, and references therein). For $\omega_s \simeq 0.5$ the NS is at equilibrium, with a spin period

$$P_\mathrm{eq} = 3.9\mu_{30}^{6/7} \left(\frac{M}{M_\odot}\right)^{-2/7} R_6^{-3/7} L_{37}^{-3/7}\,\mathrm{s} \tag{1.19}$$

Accreting NSs with spin periods $P \simeq P_{eq}$ will alternate spin-down and spin-up phases.

1.2.3 On the origin of spin pulsations from a NS

The presence of the magnetosphere is crucial for the production of coherent pulsations at the spin period. Near the magnetic poles, the inflowing matter is forced to follow the closed magnetic field lines and, thus, forms accretion columns. The accretion onto the NS surface will happen only in the form of hot spots, from which the X-ray radiation is emitted. Although the details of the process are uncertain, the radiation is supposed to be produced in the form of beams that are visible to the observer only when they cross their line of sight. Fig. 1.4 shows a schematic representation of the process.

1.3 The Eddington limit

There is one last quantity I need to define in order to understand the ultraluminous X-ray source phenomenology. Let us consider a simple case: radial accretion of pure-hydrogen plasma onto a compact object of mass M. The plasma will be subjected to two, competing forces. The plasma will be pulled towards the accretor by the gravitational attraction of the compact object itself. Since $m_p \simeq 1800 m_e \simeq 1.67 \times 10^{-24}\,\mathrm{g}$, where m_p and m_e are the mass of the proton and the electron,

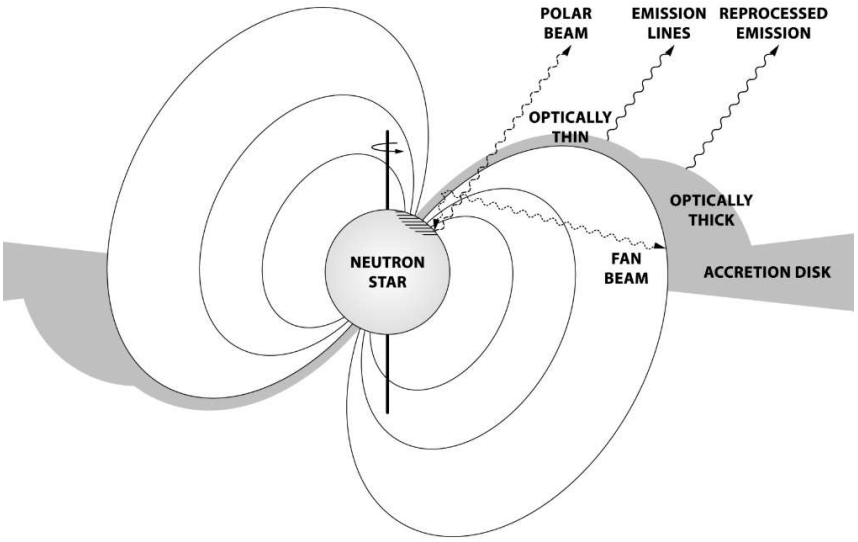

Figure 1.4. Graphical representation of the proximity of a magnetised NS during accretion. Plot taken from Koliopanos and Vasilopoulos (2018)

respectively, we can neglect the gravitational attraction onto the electrons. The gravitational force exerted onto each proton will be:

$$F_{\rm grav} = \frac{GMm_p}{r^2} \tag{1.20}$$

At the same time, the photons emitted by the accretion process will exert an outward pressure onto the particles. Assuming that the main interaction process is the Thomson scattering, we can neglect the contribution of the radiative force onto the protons since the cross-section $\sigma \propto m^{-4}$. The electrons, instead, will be subjected to a radiative force

$$F_{\rm rad} = \frac{L\sigma_{\rm T}}{4\pi r^2 c} \tag{1.21}$$

where $\sigma_{\rm T} = 6.65 \times 10^{-25}\,{\rm cm}^{-2}$ is the Thomson cross-section for an electron. Through the Coulomb interaction, the protons (electrons) will drag the electrons (protons) toward (away from) the accretor. Equating eq. (1.20) and eq. (1.21) we obtain the luminosity for which the forces balance each other:

$$L_{\rm Edd} = \frac{4\pi GMm_p}{\sigma_{\rm T}} \simeq 1.3 \times 10^{38} \frac{M}{M_\odot}\,{\rm erg\,s^{-1}} \tag{1.22}$$

This limit, derived for the first time by Eddington (1925), is known as the Eddington limit, or the Eddington luminosity, and it represents a limit to the accretion process, according to the standard theories. For luminosities $L > L_{\rm Edd}$, the radiative force dominates over the gravitational attraction and accretion is inhibited. We can use eq. (1.8) to express this limit in terms of the accretion rate $\dot{m}$. In the

case of an accreting NS with $\epsilon \simeq 0.1$ we obtain

$$\dot{m}_{\rm Edd} \simeq 2.3 \times 10^{-8} \frac{M}{M_\odot} \, {\rm M}_\odot \, {\rm yr}^{-1} \tag{1.23}$$

The higher the mass of the accretor, the stronger the gravitational attraction, the higher $L_{\rm Edd}$ (or, equivalently, $\dot{m}_{\rm Edd}$). For a $1.4\,{\rm M}_\odot$ NS, for example, $L_{\rm Edd} \sim 10^{38}\,{\rm erg\,s^{-1}}$, while for a BH with $M = 10\,{\rm M}_\odot$ we obtain $L_{\rm Edd} \sim 10^{39}\,{\rm erg\,s^{-1}}$.

1.4 Ultraluminous X-ray Sources

Since the 1970s, the study of (Galactic) XRBs has confirmed the basic phenomenological interpretation outlined in the previous sections. We now know of 360 LMXBs (Avakyan et al., 2023) and 172 HMXBs (Neumann et al., 2023) within our Galaxy[5]. Meanwhile, additional phenomenological (sub-)classes have been identified (for a general description of the known classes of accreting compact objects, their formation, and evolution see Belloni and Schreiber, 2023, and references therein). Although derived in the approximation of spherical simmetry and accretion of pure-hydrogen matter, the Eddington limit has always been verified for all these classes of XRBs, with very few systems rarely surpassing this limit. The relation expressed in eq. (1.22) has been proven multiple times to be useful in the study and characterization of the XRB population in the Galaxy and the Magellanic Clouds, even for those XRBs accreting from a disk (Dage and Kovlakas, 2024, and references therein). The diagram in Fig. 1.5 reflects the variety of accreting pulsar classes identified since the 1970s.

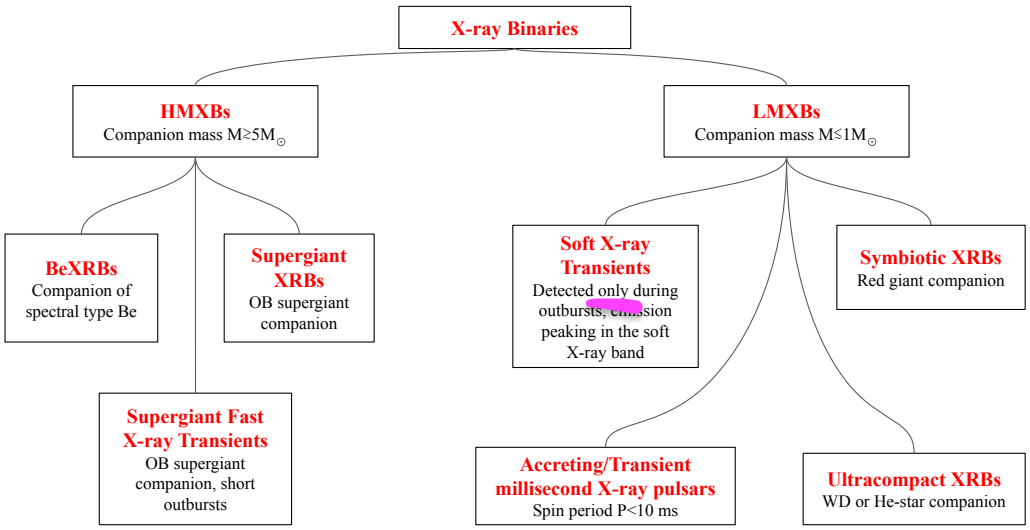

Figure 1.5. Exemplary diagram of XRBs classes that host accreting NSs. Some of these classes can also host BHs. A basic description is provided in each box.

[5]For the most recent catalogues of Galactic XRBs see the XRBCats at the following link: http://astro.uni-tuebingen.de/~xrbcat/index.html.

When the *Einstein Observatory* obtained the first resolved images of external galaxies in the X-ray band, a few X-ray sources stood out for their extreme luminosities, which under the assumption of isotropic emission were found to be $L_X \gtrsim 10^{39}\,\mathrm{erg\,s^{-1}}$ (Long et al., 1981; Fabbiano, 1989). Makishima et al. (2000) were the first to classify these extragalactic XRBs as Ultraluminous X-ray Sources (hereafter ULXs). They are point-like, accreting sources, far enough from the nucleus of the host galaxy, so that the possibility of accreting super-massive BHs (SMBHs) can be ruled out. Currently, we know more than 1800 (confirmed and candidate) ULXs (Walton et al., 2022; Tranin et al., 2024). In this section, I am going to describe the main properties, the state-of-art, and the open questions on ULXs.

The study of ULXs is not restricted to the X-ray band alone and intersects with numerous branches of astrophysics. Both radio (Kaaret et al., 2003) and optical/IR/UV counterparts and nebulae around them (see e.g. Pakull and Mirioni, 2002, 2003; Khan and Middleton, 2023; Gúrpide and Segura, 2024) have been detected. Recently, Mondal et al. (2020) showed that approximately 50 per cent of merging BH–BH progenitors have evolved through a ULX phase. The study of ULXs, therefore, can improve our understanding of the gravitational-waves sources. Finally, ULXs could also have had a non-negligible role in the reionization of the Universe through extreme ultraviolet and soft X-ray radiation (Garofali et al., 2024, and references therein). For a more thorough discussion on the ULXs phenomenology as a whole, I refer the interested reader to recent reviews (Kaaret et al., 2017; Fabrika et al., 2021; King et al., 2023; Pinto and Walton, 2023; Gilfanov et al., 2022; Dage and Kovlakas, 2024), where the topic is addressed from both theoretical and observational perspectives.

1.4.1 ULXs as sub-Eddington intermediate-mass BHs

The classification of a source as a ULX is purely phenomenological: Makishima et al. (2000) classified an XRB as a ULX if $L_X \gtrsim 10^{38}\,\mathrm{erg\,s^{-1}}$ (the Eddington limit of a NS). The common threshold in use today is $L_X \gtrsim 10^{39}\,\mathrm{erg\,s^{-1}}$, i.e. the Eddington limit for an accreting BH with $M \simeq 10\,\mathrm{M_\odot}$, as one can see from eq. (1.22). In the standard accretion theory, the Eddington luminosity is considered a hard limit that an XRB can only momentarily surpass. Even in this case, the maximum luminosity is expected to be greater than L_{Edd} of a factor of only a few. If $L_X < L_{\mathrm{Edd}}$, the source is said to be in the sub-Eddington regime.

If one assumes that a ULX with $L_X \gtrsim 10^{39}\,\mathrm{erg\,s^{-1}}$ is accreting at sub-Eddington rates ($\dot{m} < \dot{m}_{\mathrm{Edd}}$), then the accretor must be a BH with $M_{\mathrm{BH}} \gtrsim 10\,\mathrm{M_\odot}$. This is heavier than the most massive BHs known in the Galaxy (Remillard and McClintock, 2006). Since ULX luminosities are in the range $L_X \sim 10^{39} - 10^{42}\,\mathrm{erg\,s^{-1}}$, under the sub-Eddington assumption they would suggest the presence of accreting BHs with $M_{\mathrm{BH}} \sim 10 - 10^4\,\mathrm{M_\odot}$. Such masses are the one predicted for the intermediate mass BHs (IMBHs), the long-sought seeds of (primordial) SMBHs. Historically, sub-Eddington accretion onto IMBHs was the first model proposed to explain ULX luminosities (see e.g. Colbert and Mushotzky, 1999). The best IMBHs candidates are the so-called hyperluminous X-ray sources (HLXs), a subclass of ULXs having X-ray luminosities $L_X > 10^{41}\,\mathrm{erg\,s^{-1}}$ (Gao et al., 2003). Among them, the best example of an HLX is ESO 243–39 HLX-1 (Farrell et al., 2009), which reaches a peak

luminosity $L_X \sim 10^{42}\,\mathrm{erg\,s^{-1}}$. However, its spectral states are more similar to those of sub-Eddington XRBs hosting BHs rather than common ULXs, with outbursts lasting $\sim 100\,\mathrm{d}$ and with a recurrence period of $\sim 400 - 800\,\mathrm{d}$. Lin et al. (2020) have shown that the long-term evolution of these outbursts is consistent with that expected from failed tidal-disruption events, supporting the IMBH scenario for this source.

1.4.2 ULXs as super-Eddington accretors

An alternative explanation for the ULXs extreme luminosities is accretion above the Eddington limit. In this case, the source is said to be in the super-Eddington regime, or that it is accreting at super-Eddington rates. The possibility of super-Eddington accretion was already explored by Shakura and Sunyaev (1973) (SS73 from now on). Subsequent works addressed the topic in more depth, taking into account, for instance, photon trapping and exploring the possibility of advection-dominated disks.

A detailed discussion of the different super-Eddington accretion models (see e.g. Abramowicz et al., 1988; Abramowicz, 2005; Poutanen et al., 2007, and references therein) is outside the scope of this thesis. Here, I will briefly describe the accretion disk structure in the super-Eddington regime as presented in SS73. The key point is that the Eddington limit always applies locally. Any excess material is expected to be launched from the disk in the form of winds. This happens when the accretion rate exceeds a critical value

$$\dot{m}_{\mathrm{crit}} > \frac{9}{4}\dot{m}_{\mathrm{Edd}} \tag{1.24}$$

The outer parts of the disk, where $\dot{m} < \dot{m}_{\mathrm{crit}}$, remain geometrically thin, down to the spherization radius

$$R_{\mathrm{sph}} = \frac{\dot{m}}{\dot{m}_{\mathrm{Edd}}} R_{\mathrm{in}} \tag{1.25}$$

where R_{in} is the inner radius of the accretion disk. Within R_{sph}, the radiation pressure inflates the disk and becomes geometrically thick. The winds are launched in this region. At the inner edge of the disk the accretion rate is expected to be $\sim \dot{m}_{\mathrm{Edd}}$ thanks to the loss of matter caused by the winds. The X-ray radiation will not be emitted isotropically, since the launched material is optically thick and produces a funnel that collimates the X-ray radiation from the accretor. If we define the beaming factor b as the fraction of the sphere within which the radiation is emitted, it can be shown that REF

$$L \simeq \frac{L_{\mathrm{Edd}}}{b}\left[1 + \ln \frac{\dot{m}}{\dot{m}_{\mathrm{Edd}}}\right] \tag{1.26}$$

Fig. 1.6 shows a diagram of the disk structure in the proximity of the accretor. Travelling from the outer regions of the disk, R_{ph} is the outer edge of the photosphere, the radius at which the optical depth τ starts being greater than unity; R_{sph} is the spherization radius expressed in eq. (1.25); finally, $R_{\mathrm{ph,in}}$ is the inner edge of the photosphere, where τ drops back to unity.

A prediction of this model is that observers with different lines of sight will observe different regions of the disk and, therefore, observe different spectral emissions. An

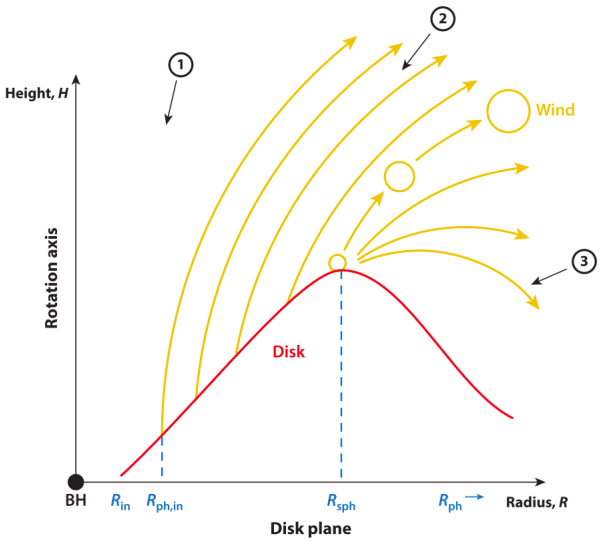

Figure 1.6. Representation of a super-Eddington disk. The different radii and zones are explained in the text. The winds launched by the disk are represented by the yellow lines and clumps, while the red line shows the accretion disk. Plot taken from Kaaret et al. (2017).

observer along the line of sight labelled with the number 3 will see the outer edge of the photosphere, where the temperature is lower and the emission peaks in the UV range. At intermediate angles (line of sight 2), the emission is dominated by the optically thick winds, whose energy spectrum is a soft thermal component with a temperature similar to the one of the disk at $R_{\rm sph}$. Finally, an observer along line of sight 1 will see the inner disk and the central accretor. In this case, the energy spectrum is harder. A change in the line of sight can result in a change in the energy spectrum of the source.

Some words of warning are needed before I continue: although the super-Eddington scenario depicted in SS73 is routinely applied to accreting BHs and NSs alike, the model was originally developed only for accreting BHs. Care is needed when applying the relations shown in this section to super-Eddington NSs. Deviations are expected in the case of an accreting NS, due to the presence of a solid accreting surface and intense magnetic fields in the proximity of the NS itself. In particular, eq. (1.26) does not take into account the presence of a magnetosphere and should not be applied blindly to PULXs (as it was done, for example, by King et al. 2017).

1.4.3 Pieces of evidence in support of super-Eddington accretion

It is not accidental that the first works proposing that ULXs are stellar-mass, super-Eddington NSs and BHs came out in the early 2000s (King et al., 2001; Poutanen et al., 2007; Zampieri and Roberts, 2009). At the end of the last century, both NASA and ESA launched the first X-ray telescopes with higher effective area and better spatial resolution than previous X-ray missions. *Chandra* (Weisskopf et al.,

2000) and *XMM-Newton* (Jansen et al., 2001) greatly improved our understanding and characterization of ULXs. A few years later, the launch of *NuSTAR* (Harrison et al., 2013) allowed for the first time to study and characterise these sources at energies $E > 10\,\mathrm{keV}$. With these telescopes, the first pieces of evidence supporting the super-Eddington interpretation started to emerge.

First of all, the spatial capabilities of these instruments (*Chandra* in particular) led to the first population studies of extragalactic XRBs, ULXs included. ULXs are predominantly found in late-type galaxies with high star formation rates (SFRs) and low metallicity (Kovlakas et al., 2020), preferentially in or near star-formation regions (Colbert et al., 2004; Mineo et al., 2013). These suggest that ULXs represent a subclass, or more likely a high-accretion phase (Wiktorowicz et al., 2017), of HMXBs. Fig. 1.7 shows the X-ray luminosity function (XLF) of XRBs in both elliptical and star-forming galaxies (Kaaret et al., 2017). In the latter, the lack of significant breaks until $L_\mathrm{X} \simeq 10^{40}\,\mathrm{erg\,s^{-1}}$ suggests that ULXs represent the high-luminosity tail of the "normal" XRBs population. At the same time, this finding clashes with the accreting IMBHs scenario: in this case, the abundance of these systems is expected to be smaller with respect to standard XRBs. As a consequence, one would expect a break in the XLF at lower luminosities, $L_\mathrm{X} \simeq 10^{39}\,\mathrm{erg\,s^{-1}}$.

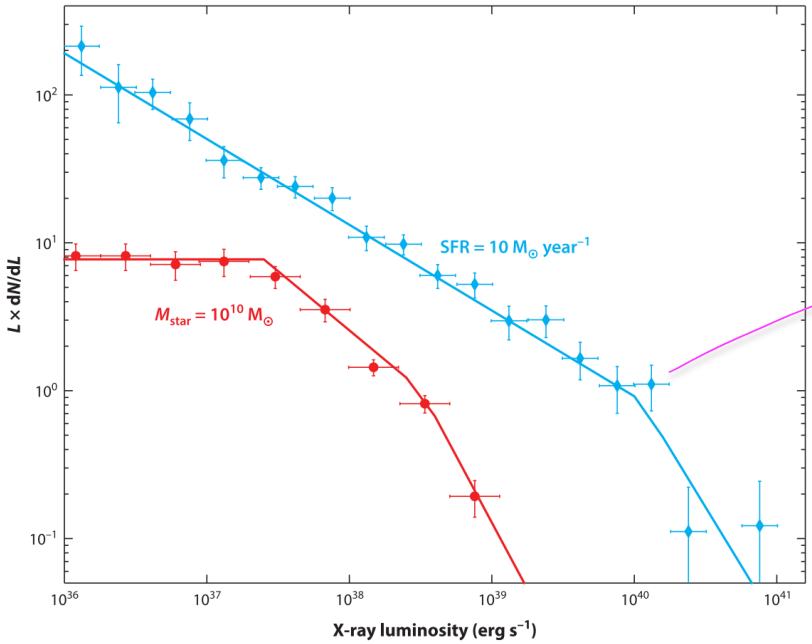

see my comment before, these might be all "normal" BHs

Figure 1.7. X-ray luminosity function (XLF) of point-like sources in star-forming (blue upper line/markers) and elliptical (red lower line/markers) galaxies. SFR stands for star formation rate. Plot taken from Kaaret et al. (2017).

for

Chandra and *XMM-Newton* allowed also high-resolution spectroscopy of extragalactic XRBs for the first time. The ULXs at lower luminosities (just above the $10^{39}\,\mathrm{erg\,s^{-1}}$ threshold) show spectral features similar to the one of Galactic XRBs during their brightest outbursts, further supporting an overlap, a sort of continuum between the two populations (Dage and Kovlakas, 2024). More interestingly, at

this is the point! Not just a number (10^39) but a real change in the spectral properties

higher luminosities the energy spectra of ULXs differ significantly from those of sub-Eddington XRBs, strengthening the super-Eddington interpretation: simple power-law models and/or standard multicolour disk black-body are excluded by virtually all long-exposure observations with sufficiently good spectral quality (Kaaret et al., 2017). High-quality *XMM-Newton* observations showed not only that two components are usually required to fit the spectra in the $0.3-10\,\mathrm{keV}$ band, but also that the hard emission (at energies $\gtrsim 2\,\mathrm{keV}$) shows a peculiar curvature (Stobbart et al., 2006). The curvature becomes even steeper at energies $> 10\,\mathrm{keV}$, with spectral slopes $\Gamma \sim 3$, as found by *NuSTAR* (Walton et al., 2018, 2020).

Gladstone et al. (2009) and Sutton et al. (2013) were the first to introduce a classification of the different spectral states observed in ULXs. Fig. 1.8 shows one example for each identified state. The broadened disk is a ultraluminous state in which the emission can be described by a single thermal component. It is called broadened disk because the spectrum is well-fitted with a p-free disk, where $T(R) \propto R^{-p}$. For the thin, SS73 disk $p = 0.75$, while for these sources $p \simeq 0.5-0.6$ (supporting a non-standard disk around these sources), which corresponds to a disk with a broader range of temperatures. The trademark of ULX spectra, however, are the hard and soft ultraluminous (HUL and SUL, respectively) states, in which the spectra can be fitted by either two thermal components or a thermal plus a power-law component. In the HUL state, the ULX spectrum is dominated by the harder component (with the X-ray emission peaking in the 2–10 keV range), while in the SUL it is the softer component to dominate the emission, which peaks at energies $\lesssim 1\,\mathrm{keV}$. A sub-class of ULXs shows a very super-soft ultraluminous (SSUL) state, with the emission peaking at 1 keV. These ULXs are referred to as super-soft ULXs or ultraluminous supersoft X-ray sources (SSULXs, or ULSs). Their spectra are often described by a black-body component with $kT \simeq 100\,\mathrm{eV}$ and a power-law with $\Gamma \sim 2-4$ (Liu and Di Stefano, 2008).

Maybe you can add the similauted spectra to show the differences

The different spectral states can be explained with the geometry of the disk described in Sect. 1.4.2 and shown in Fig. 1.6. According to the inclination of the binary system along the line of sight, an observer will view different regions of the disk. An SSUL could correspond to the emission from a ULX observed along line of sight 3, where only the outer/colder regions of the disk are visible. HUL and SUL, on the other hand, would correspond to 1 and 2, which allow the observer to see the inner regions of the disk, with 1 pointing directly towards the accretor. Some ULXs appear to (quasi-periodically) change spectral state in time (see e.g. Pintore et al., 2017; Rodríguez Castillo et al., 2020, and references therein). This is probably caused by a precessing disk (see e.g. Middleton et al., 2018), with the different spectral states being associated with a change in the geometry of the system as seen along our line of sight.

Is there any relation with the observed luminosity?

super-orbital modulation?

Finally, atomic emission and absorption lines associated with powerful winds have now been detected in the X-ray spectra of various ULXs (Pinto et al. 2016; Kosec et al. 2018, 2021; Pinto and Kosec 2023; see also Fig. 1.9 for an example). The emission and absorption lines seem to be produced by different mechanisms. Unlike the absorption lines, which show a velocity shift $v \sim 0.2-0.3c$, the emission lines are observed at rest-frame wavelengths and are probably associated with collisional shocks between the outflowing winds (where the absorption lines originate) and the circumsystem gas (Pinto et al., 2016). The presence of these winds is another feature

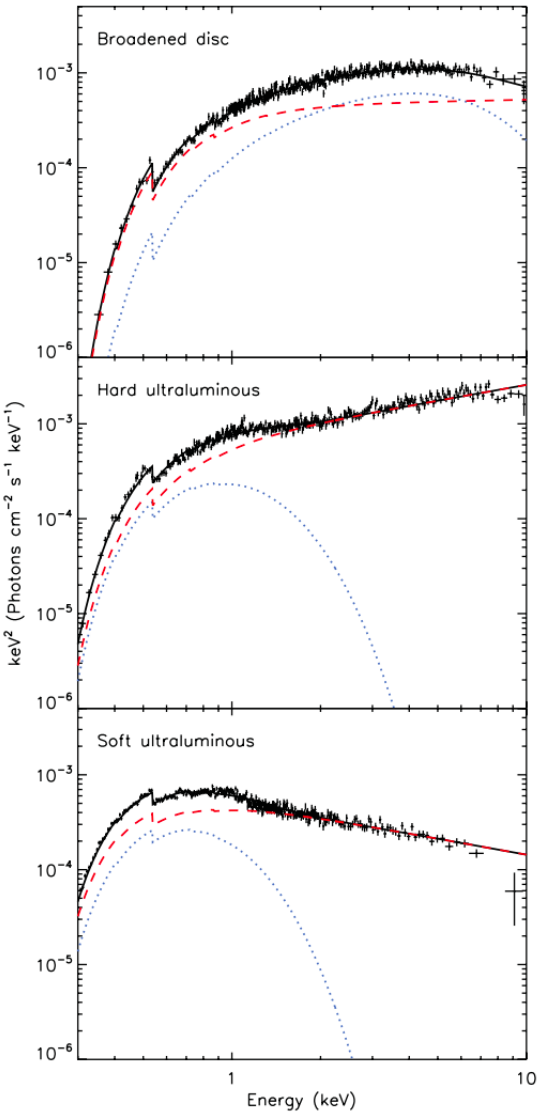

Figure 1.8. Example of different ULXs showing the three spectral states identified by Gladstone et al. (2009) and Sutton et al. (2013). From top to bottom: NGC 1313 X-2 in the broadened disk state; Ho IX X-1 in the hard ultraluminous state; NGC 5408 X-1 in the soft ultraluminous state. Blue dotted line: multi-colour disk component. Red dashed line: power-law component. Black continuous line: whole model. Plot taken from Sutton et al. (2013).

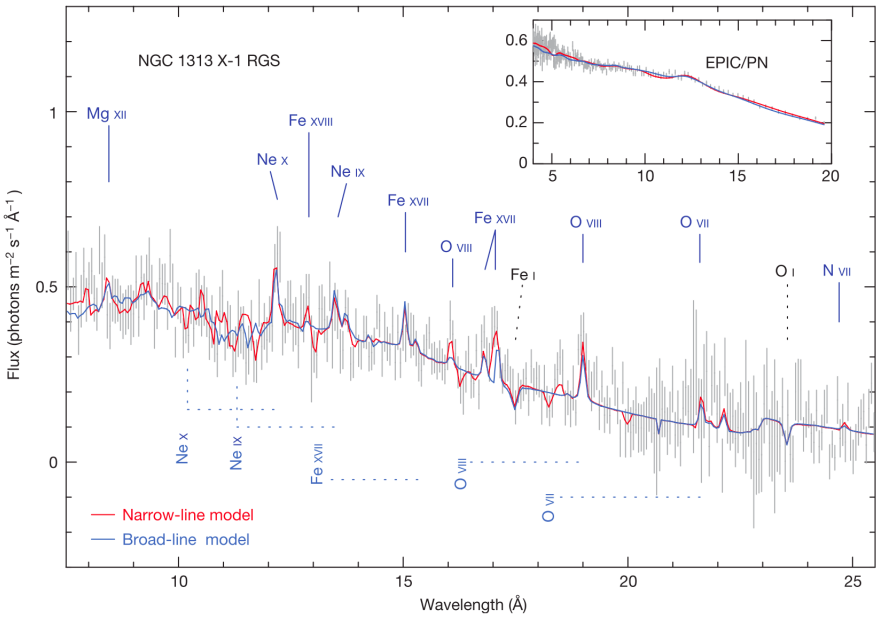

Figure 1.9. Spectral fits of the stacked *XMM-Newton* RGS (main panel) and EPIC PN (inset) data of NGC 1313 X-1. *XMM-Newton* observed the source multiple times in the span of 15 years. Rest-frame wavelengths and velocity shifts are highlighted. Plot taken from Pinto et al. (2016).

easily explained in the super-Eddington scenario. As described in Sect. 1.4.2, winds are expected to be launched within $R_{\rm sph}$, where the local accretion rate exceeds the Eddington rate $\dot{m}_{\rm Edd}$.

Somewhere you should give a rough census of how many ULX are known and how (still roughly) they are distributed in luminosity.

1.5 Pulsating ULXs

The definitive evidence that (at least some) ULXs are powered by super-Eddington accretors arrived in 2014, when Bachetti et al. (2014) discovered coherent pulsations with a period $P \simeq 1.37\,$s in the flux of M82 X-2. The source had been previously identified as a candidate IMBH (Feng et al., 2010, see Chap. 2), but the presence of pulsations at these timescales is only possible if the source is an accreting NS, with a mass $M_{\rm NS} \simeq 1.4\,{\rm M}_{\odot}$. This source can reach X-ray luminosities in the 0.3–10 keV band as high as $\sim 2 \times 10^{40}\,{\rm erg\,s^{-1}}$, about 100 times the Eddington limit for an accreting NS. M82 X-2, therefore, represents the archetypal pulsating ULX, or PULX[6]. The discovery of this PULX opened an unprecedented window on this extreme luminosity (accretion) regime.

1.5.1 The PULX population and main properties

Since 2014, a total of 14 (11 confirmed and 3 candidates) PULXs have been discovered. Tab. 1.1 summarizes the main characteristics of the PULX population.

[6]The reader may also find the acronym ULXP, from ultraLuminous X-ray pulsar (see e.g. Chashkina et al., 2019). In this thesis, I will follow the convention presented in the main text and

Table 1.1. Main properties of the known (canonical, occasional and candidate) PULXs. Adapted from Table 2 of King et al. (2023).

PULX	P (s)	$\dot{P}^a_{\rm sec}$ ($\rm s\,s^{-1}$)	$P_{\rm orb}$ (d)	$L^b_{\rm max}$ ($10^{39}\,\rm erg\,s^{-1}$)	$M^c_{\rm com}$ ($\rm M_\odot$)
			Canonical		
M82 X-2	1.4	1×10^{-11}	2.5	20	$\gtrsim 5.2$
NGC 5907 ULX-1	1.1	-8×10^{-10}	5.7[d]	200	–
NGC 7793 P13	0.4	-4×10^{-11}	64	10	18–23 (B9I)
M51 ULX-7	2.8	-1×10^{-9}	2	10	> 8
NGC 300 ULX-1	31.6	-6×10^{-7}	> 290	5	8–10 (RSG)
NGC 1313 X-2	1.5	1.2×10^{-12}	< 4	20	–
			Occasional		
SMC X-3	7.8	-4×10^{-9}	45	3	> 3.7 (Be)
NGC 2403 ULX	18	3.4×10^{-10}	60–100	1.2	– (Be?)
Swift J0243.6+6124	9.9	2.2×10^{-10}	28.3	1.5	– (Be?)
RX J0209.6-7427	9.3	1.2×10^{-10}	> 50	2	– (Be)
NGC 1313 PULX	765.6	–	–	1.6	– (Be?)
			Candidate		
M51 ULX-8[e†]	–	–	–	2	– (Be?)
NGC 7793 ULX-4[f†]	0.4	–	–	3.4	–
NGC 2403 XMM4[g†]	0.3	–	–	1.0	–

Always neglected, there is also the Be transient A0538-66 in the LMC with 69ms spin period, reaching ~1e39

Notes.
[a] Secular spin-up/down rate.
[b] Maximum observed luminosity in the 0.3–10 keV band.
[c] Mass of the companion star. In parentheses I report the spectral classification of the companion, when available.
[d] See recent estimate in Belfiore et al. (2024).
[e] Identified as a candidate PULX by Brightman et al. (2018), thanks to the detection of an absorption line at 4.5 keV probably arising from cyclotron resonance scattering. No spin signal has been detected yet.
[f] Quintin et al. (2021): the detection of the spin signal has a low significance. Note also that, if the signal is confirmed, the available data show that this source is an occasional PULX.
[g] Luangtip and Roberts (2024): the source luminosity may be lower than $10^{39}\,\rm erg\,s^{-1}$, the common threshold to classify an XRB as a ULX.
[†] Candidate PULX.

Apart from their extreme luminosities, PULXs are characterised by particularly high short-term (within the timespan of an observation) spin-up rates. Bachetti et al. (2014) found a short-term spin-up rate $\dot{P} \simeq -2 \times 10^{-10}\,\mathrm{s\,s^{-1}}$ for M82 X-2. Other PULXs show similar short-term spin-up rates, typically in the range $-10^{-10}\,\mathrm{s\,s^{-1}} \lesssim \dot{P} \lesssim -10^{-11}\,\mathrm{s\,s^{-1}}$. Some notable exceptions are NGC 5907 ULX-1 (Israel et al., 2017a) and NGC 300 ULX-1 (Carpano et al., 2018), which have shown the highest spin-up rates known, $-5 \times 10^{-9}\,\mathrm{s\,s^{-1}}$ and $-6 \times 10^{-7}\,\mathrm{s\,s^{-1}}$, respectively. For comparison, typical local spin-up rates for accreting NSs are $-10^{-12}\,\mathrm{s\,s^{-1}} \lesssim \dot{P} \lesssim -10^{-14}\,\mathrm{s\,s^{-1}}$. M82 X-2 has also shown periods of spin-down rates during accretion, suggesting that this source is close to spin equilibrium (Bachetti et al., 2020).

Among the confirmed PULXs, despite their low number, there is a hint for at least two distinct classes based on a phenomenological approach. The first 6 PULXs in Tab. 1.1 are observed to sustain super-Eddington luminosities for extended periods of time. I will refer to these 6 sources as the canonical PULXs and focus the discussion on them. The remaining 5 confirmed PULXs, on the other hand, are observed at super-Eddington luminosities only during outbursts that usually last for a few weeks or months. Additionally, while all the canonical PULXs are found in external galaxies, 3 out of these 5 remaining PULXs are found in the local group. I will refer to these 5 sources as the occasional PULXs.

they are also dimmer

For the 4 canonical PULXs for which the orbital solution is known, the mass of the companion has to be $\gtrsim 5\,\mathrm{M_\odot}$. In the case of NGC 5907 ULX-1 and M51 ULX-7, the mass of the companion has been inferred from the orbital parameters. NGC 7793 P13 and NGC 300 ULX-1 are the only two PULXs for which the optical/IR counterpart has been identified. The former has a companion of spectral type B9I, with a mass $M \simeq 18 - 23\,\mathrm{M_\odot}$ (Motch et al., 2011, 2014), while for the latter the companion has been identified in the IR band as a red supergiant with $M \simeq 8 - 10\,\mathrm{M_\odot}$ (Heida et al., 2019). These findings further support the hypothesis that (P)ULXs represent a high-accretion phase of HMXBs.

Among the 5 occasional PULXs, the only one with a classified companion (a Be-type star) is SMC X-3 (Edge et al., 2004). This system is a BeXRB, with X-ray luminosity during outbursts that can barely surpass the ULX threshold (Townsend et al., 2017; Koliopanos et al., 2017). BeXRBs outbursts usually have lower peak luminosities (Type I outbursts, with $L_\mathrm{X} \sim 10^{36}\,\mathrm{erg\,s^{-1}}$) and occur periodically, when the NS passes through the companion decretion disk. However, BeXRBs can also sporadically show Giant or Type II outbursts, during which the luminosity can be $L_\mathrm{X} \gtrsim 10^{38}\,\mathrm{erg\,s^{-1}}$ (Okazaki et al., 2013). Although the companion is not known for the other occasional PULXs, it is likely that NGC 2403 ULX (Trudolyubov et al., 2007), NGC 1313 PULX (Trudolyubov, 2008), RX J0209.6-7427 (Vasilopoulos et al., 2020b), and Swift J0243.6+6124 (Wilson-Hodge et al., 2018) are also BeXRBs which occasionally show extremely bright Type II outbursts.

Another feature that distinguishes canonical and occasional PULXs is the maximum luminosity they can reach. As one can see from Tab. 1.1, the first can reach higher luminosities, with NGC 5907 ULX-1 sporadically reaching even the hyperluminous X-ray source threshold of $10^{41}\,\mathrm{erg\,s^{-1}}$ (Israel et al., 2017a). Occasional PULXs, on the other hand, are found at lower maximum luminosities $\sim$ few $10^{39}\,\mathrm{erg\,s^{-1}}$.

always use the acronym PULX.

From a spectral point of view, it is almost always impossible to identify the nature of the accretor in a ULX system. Walton et al. (2018) analysed a sample of bright ULXs and compared their spectra with those of known PULXs. They concluded that the spectral models commonly used for *XMM-Newton*+*NuSTAR* data of PULXs can describe equally well the energy spectra of other ULXs, suggesting that there could be a larger population of hidden PULXs. Pintore et al. (2017) found that PULXs tend to have harder spectra, a result later confirmed by Gúrpide et al. (2021), suggesting that the best ULXs to look for candidate PULXs are those whose emission peaks at energies $\gtrsim 2\,\mathrm{keV}$. Gúrpide et al. (2021) also found that ULXs show two different tracks in the hardness-intensity diagram. They concluded that the different types of tracks could indicate a different nature of the accretor, i.e. BH vs NS, providing a potential method to distinguish between NS– and BH–ULXs.

A notable example of a candidate PULX identified through spectral analysis is M51 ULX-8. Brightman et al. (2018) found a narrow absorption feature in the energy spectrum of this source at 4.5 keV. The best explanation for this line is that it is a cyclotron resonance scattering feature (CRSF), suggesting that the accretor is a neutron star (NS) with a magnetic field of either $B \sim 10^{11}\,\mathrm{G}$ (if the CRSF is produced by scattering electrons), or $B \sim 10^{15}\,\mathrm{G}$ (if produced by scattering protons). No spin signal has been detected from this source yet.

1.5.2 Why it is hard to find new PULXs

The conclusion that PULXs may represent a consistent fraction of ULXs (see e.g. Walton et al., 2018) may seem to be at odds with the fact that only a handful of PULXs out of more than 1800 ULXs has been discovered in the last 10 years. However, there are some factors that hinder our capability of detecting the spin signal from a PULX. First of all, the emission from a NS is expected to be beamed both by the magnetic field and the wind cone. Therefore, we can detect pulsations only from those PULXs whose beam is pointing towards us. The main obstacle to the detection of spin pulsations, however, is the high spin-up rates exhibited by these sources.

One of the most frequently used tools for detecting periodic variability in the flux of a source is the power density spectrum (PDS), which relies on the discrete Fourier transform. A detailed discussion on the Fourier analysis is outside the scope of this thesis. I refer the interested reader to van der Klis (1989a), from which most of this section is adapted.

Let us consider the observation of a NS with a known spin period P. Its flux evolution in time, i.e. its light curve or time series, can be decomposed in the sum of N sinusoidal function through the Fourier transform. In the practical cases, the X-ray instruments detect each photon individually. The flux history of a source will therefore result in a descrete series of N values x_k that correspond to the number of photons in the k-th time bin, with $k = 0, 1, ..., N-1$. If the observation has a length T and each time bin has the same length $\delta t = T/N$ (i.e. the time series is equidistant and the instrument has a constant sampling time), we can write the

discrete Fourier transform (DFT) of the light curve in exponential notation as

$$a_j = \sum_{k=0}^{N-1} x_k e^{2\pi i j k/N} \quad j = -\frac{N}{2}, ..., \frac{N}{2} - 1 \tag{1.27}$$

where x_k is the number of photons detected at a time $t_k = kT/N$ and the DFT is the ensemble of all the a_j. Each a_j will refer to a frequency $\nu_j = j/T$ known as Fourier frequency, with a frequency step between two adjacents Fourier frequencies $\delta\nu = 1/T$. The maximum frequency that the DFT can sample is the Nyquist frequency

$$\nu_{\rm Nyq} = \frac{N}{2T} = \frac{1}{2\delta t} \tag{1.28}$$

equal to half the sampling frequency. From the DFT, we can compute the PDS as the set of powers

$$P_j \equiv \frac{2}{N_{\rm ph}} |a_j|^2 \tag{1.29}$$

where $N_{\rm ph} = \sum_{k=0}^{N-1} x_k$ is the total number of photons detected during the observation. In the ideal case, where the light curve is purely sinusoidal at a spin frequency $\nu = 1/P$ of the NS, we would expect a single peak in the PDS at frequency $\nu_j \simeq \nu$ and with power $P_j = 0.5N^2A^2/N_{\rm ph}$, where A is the amplitude of the spin signal.

In a real-life scenario, noise will always be present. Therefore, we must define a procedure to establish the detection of a signal peak at a given confidence level in the presence of noise. For the definition of P_j, I adopted the Leahy normalization (Leahy et al., 1983), which is the one commonly used in X-ray astrophysics. The reason behind this choice is that, as a first approximation, the dominant noise component in an X-ray observation is the Poissonian counting noise. With this normalization, the Poissonian noise has a known distribution of powers, which is a χ^2 with 2 degrees of freedom (d.o.f.), in the case of a single PDS[7]. The Poissonian noise is independent of the analysed frequency, which is why it is commonly referred to as white noise. The integral probability of the powers arising from white noise is given by

$$Q(P|2) = e^{-P/2} \tag{1.30}$$

Given a confidence level α, the probability $\eta = 1 - \alpha$ that at a given frequency the power $P_{\rm noise}$ will be greater than a threshold $P_{\rm det}$ will simply be $\eta = Q(P_{\rm det}|2) = e^{-P_{\rm det}/2}$. Therefore, we can set $P_{\rm det}$ to match the desired confidence level: if the PDS shows a peak at a power $P_j > P_{\rm det}$, we can claim the detection of a real signal with a confidence level α. In more realistic cases, additional, "coloured" noise components are present and a simple constant threshold cannot be used. I refer the reader to Israel and Stella (1996) for a method to compute a frequency-dependent detection threshold which takes into account red noise (an excess of power with a power-law distribution $P_j \propto \nu_j^{-\alpha}$ at the low-frequency tail of the PDS).

The problem with the PDS is that it assumes that the period of the signal is constant with time. This is not the case for PULXs, which have extremely high spin-up rates. A detailed discussion on the effects of $\dot{P}$ on the PDS can be found in

[7] If the PDS is the result of $N_{\rm PDS}$ averaged PDSs, the number of d.o.f. is $2N_{\rm PDS}$.

Ransom et al. (2002). For a simpler approach, let us assume a source with a constant spin-up rate $\dot{P}$ and a spin period P at the beginning of an observation which lasts for a time T. During the observation, the spin frequency $\nu = 1/P$ will change of a factor $\dot{\nu}T$, which is equal to a number of Fourier frequencies $\dot{\nu}T^2$. The power of the spin signal, therefore, will be diluted (often below the detection threshold) over multiple Fourier frequencies as soon as $\dot{\nu}T^2 > 2$. Considering the case of NGC 5907 ULX-1, with a spin-up rate of $-5 \times 10^{-9}\,\mathrm{s\,s^{-1}}$ the spin frequency will have moved of about 8 Fourier frequencies after only $T \simeq 40\,\mathrm{ks}$ (a typical length for *XMM-Newton* observations), a change that can lead to a misdetection. This estimate does not take into account the additional effect of orbital Doppler, which further dilutes the signal (Anderson et al., 1990; Johnston and Kulkarni, 1991; Vaughan et al., 1994; Ransom et al., 2001).

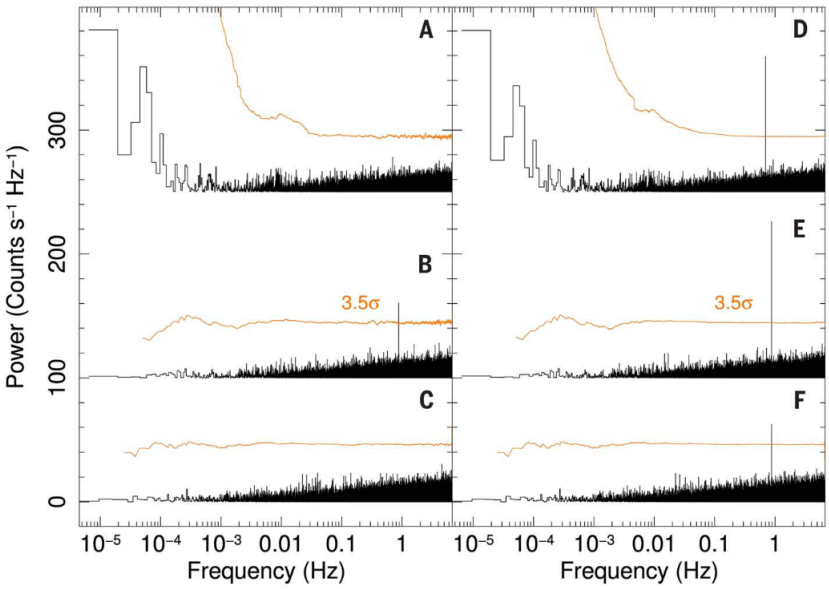

Figure 1.10. PDSs of NGC 5907 ULX-1 before (A, B, and C) and after (D, E, and F) the $\dot{P}$ correction. Plot taken from Israel et al. (2017a). PDSs A, B, D, and E are arbitrarily shifted on the y-axis for visual purposes. The frequency-dependent detection thresholds were computed following Israel and Stella (1996).

A possible solution comes from the application of the accelerated search techniques, which take into account the acceleration of the spin period. Wood et al. (1991) has shown that, as a first approximation, the orbital Doppler can be approximated with an additional spin derivative $\dot{P}_{\mathrm{add}}$. Following Ransom et al. (2002), we can correct the arrival times of each photon according to

$$t' = t + \frac{1}{2}\frac{\dot{\nu}}{\nu}t^2 = t - \frac{1}{2}\frac{\dot{P}_{\mathrm{tot}}}{P}t^2 \tag{1.31}$$

where $\dot{P}_{\mathrm{tot}}$ includes both the intrinsic spin-up rate $\dot{P}$ and $\dot{P}_{\mathrm{add}}$. I have also assumed that $\dot{P}_{\mathrm{tot}}$ is constant in time, or equivalently that for the length of the observation higher-order derivatives have negligible effects. At this point, a possible approach is the one described in Israel et al. (2017a) and Rodríguez Castillo et al. (2020): for

most of these sources, both $\dot{P}$ and the orbital parameters are unknown. Therefore, we can systematically correct the arrival times with different $\dot{P}_{\rm tot}/P$ values, compute the PDS for each value of this ratio and look for significant peaks. Once we have a detection, we can compute $\dot{P}_{\rm tot}$ and with a similar search on the orbital parameters disentangle $\dot{P}$ and $\dot{P}_{\rm add}$. Fig. 1.10 shows the case of NGC 5907 ULX-1, whose spin signal was detected in 2 out of 3 observations only after the application of this approach (Israel et al., 2017a).

Even after taking into account the spin-up rate and the orbital Doppler, the spin pulsations can still elude our detection. PULXs have spin signals that can appear and disappear, that is dramatically change the pulsed fraction, even within a single observation (Bachetti et al., 2020). Sathyaprakash et al. (2019), for example, analysed 6 *XMM-Newton* observations of NGC 1313 X-2 (for a total exposure of ~ 720 ks) and detected the spin signal only during two segments, for a total of 90 ks. In principle, one should apply the approach described above not only to the whole observation, but on several chunks of it, which can be time-consuming. Another problem is that the lower the pulsed fraction (i.e., the amplitude in normalized count rates) of the spin signal, the higher the number of photons needed to detect the pulsation in the PDS (see equation 9 in Leahy et al., 1983). At a confidence level of 3.5σ, the relation is

$$\mathrm{PF}_{\rm min} = \sqrt{\frac{P_j}{2M}\frac{4}{0.773 N_{\rm ph}}\frac{(\pi j/N_{\rm ph})^2}{\sin^2(\pi j/N_{\rm ph})}} \tag{1.32}$$

where M is the number of averaged PDSs and j is the Fourier index. Typical pulsed fractions for PULXs are of the order of 5–15%, which require ~ 10000 photons to be detected at a confidence level of 3.5σ. In 2020, the PULXs consisted of a remarkable $\sim 25\%$ of the population of ULXs with more than 10000 detected photons (Earnshaw et al., 2019; Rodríguez Castillo et al., 2020) and since then the ratio has remained stable. These findings support the conclusion of Walton et al. (2018) that more PULXs must be hidden in the ULX population.

1.6 PULX emission models

The discovery of PULXs has opened an unprecedented window on the super-Eddington regime. However, since the discovery of pulsations from M82 X-2 in 2014, it has been a matter of debate whether PULXs accrete indeed at such high accretion rates, or if PULXs are intrinsically fainter.

King et al. (2001) proposed that ULXs are XRBs with stellar-mass accretors accreting only at mildly super-Eddington rates. The extreme luminosities we infer for these sources would be the consequence of particularly pronounced geometrical beaming. The expression for the X-ray luminosity of an accreting NS in eq. (1.7) assumes that the NS isotropically emits the X-ray radiation over the whole sphere. From the fact that we observe pulsations, we know that this cannot be true, otherwise we would see a constant emission. I already introduced in eq. (1.26) the beaming factor b, which is the fraction of the sphere within which the radiation is emitted. In the case of (P)ULXs, we expect some form of beaming from the funnel produced by

the winds launched at $R_{\rm sph}$ (for a graphical depiction, see Fig. 1.11, from Mushtukov et al. 2019).

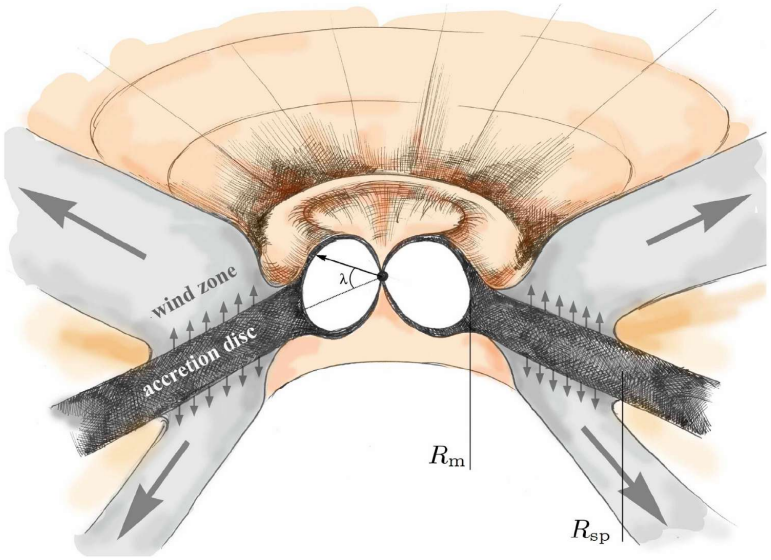

Figure 1.11. Graph by Mushtukov et al. (2019). Drawing of an accretion disk near a PULX, with winds launching from $R_{\rm sph}$.

In the case of isotropic emission, $b = 1$. If $b < 1$, $L_{\rm real} = bL_{\rm X}$ and by computing $L_{\rm X}$ under the assumption of isotropic emission one would overestimate the real, intrinsic luminosity $L_{\rm real}$ of a source by a factor $1/b$. In the case of ULXs, King (2009) found that the beaming factor can be linked with the aperture of the wind funnel, which in turn depends on the accretion rate. He derived for b the expression $b \simeq 73/\dot{m}_0^2$ for $\dot{m}_0 \gtrsim 8.5$, where $\dot{m}_0 = \dot{m}/\dot{m}_{\rm Edd}$. The higher the accretion rate, the lower b, the higher the degree of anisotropy of the emission. This relation was later extended to the case of PULXs in King et al. (2017) and King and Lasota (2020).

According to this model, PULXs would be only mildly super-Eddington sources, which appear much brighter due to geometrical beaming. It is intrinsically harder to see the pulsations from a source with a stronger beaming, which could explain the low number of detected PULXs, even though binary evolution models predict a dominance of NSs in the whole ULX population (Wiktorowicz et al., 2017). The presence of extreme beaming could also explain why eclipses and dips in the X-ray flux have been observed only for a few ULXs (Middleton and King, 2016; Fabrika et al., 2021).

It is difficult, however, to reconcile many observational pieces of evidence with this model. First of all, PULXs spin signals have highly sinusoidal profiles, which is a sign of very low beaming (Mushtukov et al., 2021). Also, from eq. (1.7) and (1.16), the spin-up rate of an accreting NS and the accretion rate are correlated. The spin-up rates observed in PULXs and the observed luminosities are both (at least) 2–3 orders of magnitude higher than the one observed in other XRBs, suggesting that PULXs are indeed accreting at highly super-Eddington rates. In the case of NGC 5907 ULX-1, a beaming factor $b \simeq 10^{-2}$ would be required to

explain luminosities $L_X \sim 10^{41}\,\mathrm{erg\,s^{-1}}$, a value never observed in any pulsar (Israel et al., 2017a). The detection of nearly-isotropic optical nebulae around (P)ULXs, originating from the X-ray radiation coming from the accretor, is another argument against the presence of strong beaming (Belfiore et al., 2020; Gúrpide et al., 2024; Gúrpide and Segura, 2024).

An alternative is that PULXs are, indeed, NSs accreting up to $\sim 500 - 1000$ times their Eddington limit. This would easily explain the main properties we observe: their luminosities, their spin-up rates, and the spectral differences with respect to sub-Eddington XRBs. Bachetti et al. (2022) measured a decay of the orbit of M82 X-2 $\dot{P}_{\rm orb}/P_{\rm orb} = -8 \times 10^{-6}\,\mathrm{yr^{-1}}$. This orbital decay is consistent with the system being driven by extreme mass transfer >150 times the limiting one set by $L_{\rm Edd}$ (see Tauris and van den Heuvel 2006 and Appendix B in Bachetti et al. 2022). Correspondingly, the mass available to the NS is more than enough to justify the observed luminosity, with no need for (extreme) beaming. A possible concern with this computation is that the $\dot{P}_{\rm orb}$ should be computed over time scales longer than the time needed for the Roche lobe to move one scaleheight within the companion, which in the case of M82 X-2 should be $t_H \sim 1000\,\mathrm{yr}$ (see Section 3.18 of King et al., 2023).

I would rather say not eject the accreting matter

In the highly super-Eddington scenario, the main issue is that it is not still clear how a NS can sustain such a high accretion rate for so long. The vast majority of theoretical works on the super-Eddington regime dating prior to the discovery of the first PULX focused on the case of a stellar-mass BH as an accretor. This is mainly due to the fact that modelling the interaction between the accretion disk and the NS magnetosphere is historically a hard task. Driven by the discovery of PULXs, a few works have faced this challenge in the last 10 years (see e.g. Mushtukov et al., 2017; Chashkina et al., 2017, 2019; Chen and Dai, 2024; Flexer and Mushtukov, 2024; Mushtukov et al., 2024).

not exactly: there are two polarisation modes and (only) one has a much lower cross section than sigma_T (if I rember correctly)

Highly-magnetized ($B \gtrsim 10^{14}\,\mathrm{G}$) NSs could overcome the Eddington limit as computed in eq. (1.22) for two reasons: first of all, at high magnetic fields the interaction cross-section between the photons and the electrons is $\sigma < \sigma_{\rm T}$. Secondly, in the proximity of the NS, the radiation is balanced by the magnetic pressure instead of gravity, allowing much higher luminosities. An intense magnetic field ($B \gtrsim 10^{14}\,\mathrm{G}$) could help the NS reach luminosities as high as $\simeq 10^{40}\,\mathrm{erg\,s^{-1}}$, well within the range of most PULXs (Mushtukov et al., 2015a,b). In this case, however, Israel et al. (2017a) noted that with the spin periods and luminosities reported in Tab. 1.1 most PULXs should constantly be in the propeller regime, which is not the case. A possibility, proposed to explain NGC 5907 ULX-1 extreme luminosities, is that the magnetic field of the accreting NS is composed of a dipolar component with $B_{\rm dip} \sim 10^{12}\,\mathrm{G}$ and a multipolar component $B_{\rm multi} \sim 10^{14}\,\mathrm{G}$. Tiengo et al. (2013) and Borghese et al. (2015, 2017) had previously found evidence of a multipolar component through the detection of cyclotron resonance scattering features in the X-ray spectra of a magnetar (SGR 0418+5729) and two isolated NSs (RX J0720.4–3125 and RX J1308.6+2127), respectively. Later, *NICER* observations of the millisecond pulsar PSR J0030+0451 showed that the emission spots on the surface of the NS are far from antipodal, strongly suggesting a dominant multipolar component for the magnetic field (Bilous et al., 2019; Miller et al., 2019; Riley et al., 2019). In the case of NGC 5907 ULX-1, a weaker dipolar component allows for smaller $R_{\rm m}$, avoiding

I understand the meaning (because I already know), but it is difficult as it is written

please, add a note to explain what it is

for

non definito

the propeller regime, while a strong multipolar component near the surface of the NS helps reach luminosities $L_{\rm X} \sim 10^{41}\,{\rm erg\,s^{-1}}$. Finally, in this case, there is no need to invoke particularly high beaming factors, with $b \simeq 0.04 - 0.2$ sufficient to explain the observed properties.

la figura dell'articolo del tuo relatore su Science, ci starebbe proprio bene! con un po' di discussione

Chapter 2

The discovery of QPOs in PULXs

Who ordered that?

Isidor Isaac Rabi about the muon

We have seen that the X-ray flux of magnetised NSs is characterised by periodic variability, with coherent pulsations caused by the spin motion of the NS. The nature of the accretion flow onto a compact object, however, is highly chaotic: density fluctuations are ubiquitous and the forces exerted among different elements of the accretion flow can influence the motion of the matter itself. The rate of matter lost from the companion, moreover, can be variable. In the case of accreting NSs, the complex interactions between the magnetosphere and the accretion disk also affect the matter infall towards the compact object. As a result, the X-ray flux of XRBs often shows different kinds of aperiodic variability, with various degrees of coherence.

A particular class of these stochastic signals is represented by quasi-periodic oscillations (QPOs), which are the subject of the next section. I recently discovered QPOs in the X-ray flux of two PULXs at super-Eddington luminosities, i.e. M51 ULX-7 and NGC 7793 P13 (Sect. 2.4 and 2.5.2). While QPOs had been previously detected in the X-ray flux of some ULXs, before these discoveries M82 X-2 was the only PULX known to show QPOs at super-Eddington luminosities. Their interpretation was deeply affected by the fact that, at the time, M82 X-2 spin pulsations had not been detected yet. These findings have huge implications for our knowledge of the PULX population. I will discuss these implications in Sect. 2.4.

2.1 Quasi-periodic oscillations: an introduction

Since the first detection in the X-ray and optical light curve of GX 339-4 by Motch et al. (1983), QPOs have been observed in a large number of BH- and NS-XRBs (see van der Klis 1989b for a historical review, Motta 2016 and Ingram and Motta 2019 for more recent reviews). They are best studied in the Fourier domain, in particular in a PDS, where they appear as broad (but not too much) peaks (see Fig. 2.1, taken from Motta et al. 2011).

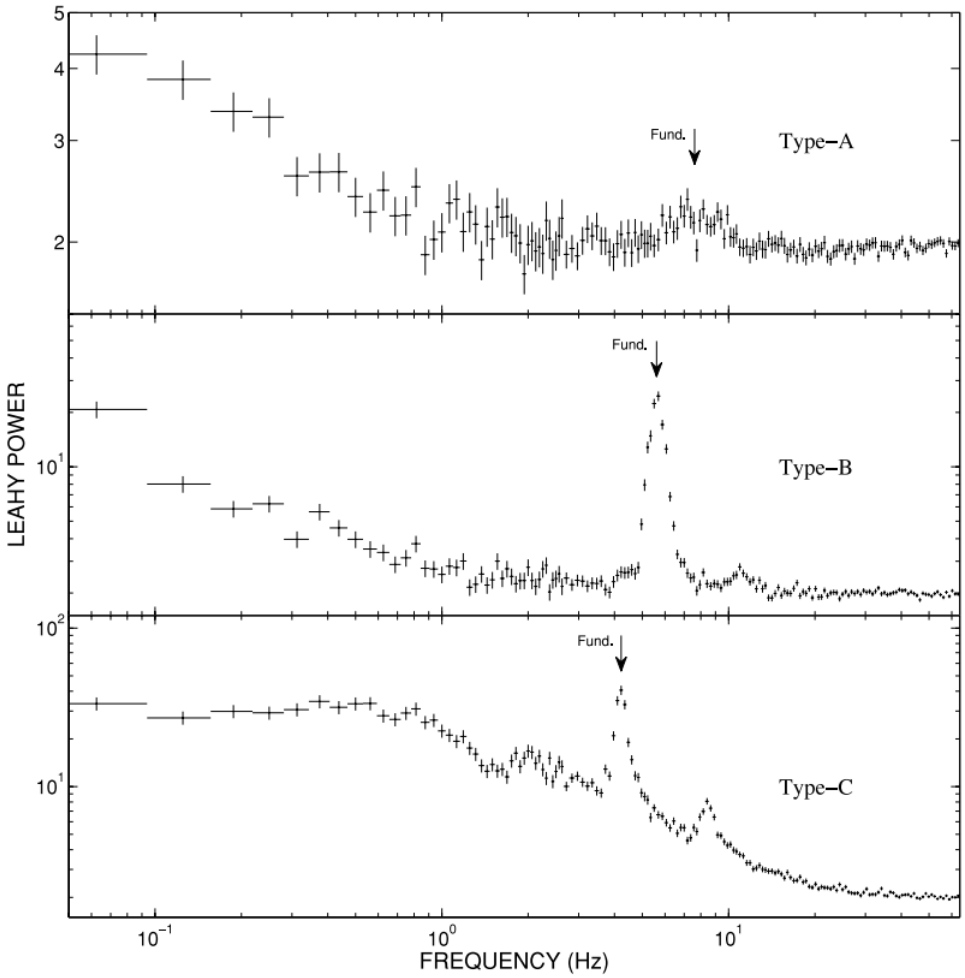

Figure 2.1. From top to bottom, example of type-A, -B, and -C QPOs detected in three different *RXTE* observations of GX 339-4. Plot taken from Motta et al. (2011).

The choice as to which broad feature in a PDS can be classified as a QPO and which is (broad-band) noise is somewhat arbitrary (van der Klis, 1989b). Usually, broad features in a PDS are modelled with a sum of Lorentzians, defined as:

$$L(\nu) = K\frac{\Delta\nu}{2\pi}\frac{1}{(\nu-\nu_0)^2+(\Delta\nu/2)^2} \tag{2.1}$$

where K is the normalization factor, equal to the integral of $L(\nu)$ from $\nu = 0$ to $\nu \to \infty$, ν_0 is the centroid frequency of the Lorentzian and $\Delta\nu$ its full width at half maximum. From ν_0 and $\Delta\nu$ we can define the quality factor as:

$$Q = \frac{\nu_0}{\Delta\nu} \tag{2.2}$$

The narrower the feature, the higher Q. A feature in the PDS is usually defined as a QPO when its quality factor $Q = \nu/\Delta\nu$ is $Q \gtrsim 2$. The quality factor can be also seen as an estimate of the number of cycles after which the modulation loses coherence. In the ideal case of a perfectly coherent signal, $\Delta\nu = 0$ and $Q \to \infty$. and in a real case?

QPOs are usually split according to the centroid frequency ν_0. In the case of Galactic XRBs hosting a BH, QPOs with $\nu_0 \lesssim 30$ Hz are classified as low-frequency QPOs (LFQPOs) and QPOs with $\nu_0 \gtrsim 60$ Hz high-frequency QPOs (HFQPOs) (Belloni, 2010). As we will see, ULX QPOs are found in the 1–100 mHz range. ULX QPOs, therefore, have been usually classified as LFQPOs. In the following, I will focus on LFQPOs. HFQPOs are much rarer and they have been detected only in a handful of sources. They are usually detected in pairs, with a 3:2 or 3:1 frequency ratio (Belloni et al., 2012).

LFQPOs are usually distinguished in three main types, first identified for XTE J1550-564 (Wijnands et al., 1999; Homan et al., 2001; Remillard et al., 2002): type-A, type-B and type-C QPOs (see Section 2.2 of Ingram and Motta, 2019). Fig. 2.1 shows an example for each type of LFQPOs. Type-A QPOs are very weak (fractional rms $\sim$ few percent) and extremely rare features, with only ~ 10 detections in the whole *RXTE* archive. They have broad peaks ($Q \lesssim 3$) and are found in the 6–8 Hz range. They are usually associated with low-amplitude red noise. Type-B QPOs, on the other hand, have narrower profiles ($Q \gtrsim 6$) and appears in the 1–6 Hz frequency range with a fractional rms up to $\sim 5\%$. They generally appear together with red noise at lower frequencies and often show a weak second harmonic. Sometimes they also show a sub-harmonic, which can have an amplitude comparable to the fundamental, in a cathedral-like shape (Casella et al., 2004). Finally, type-C QPOs have centroid frequencies that can range from ~ 1 mHz up to ~ 10 Hz. They have high amplitudes (fractional rms up to $\sim 20\%$) and narrow profiles ($Q \gtrsim 8$). They are, by far, the most common QPO type observed in BH-XRBs. As one can see from the bottom panel of Fig. 2.1, they are often associated with "flat-top" noise at low frequencies, possibly caused by fluctuations in the mass accretion rate (Lyubarskii, 1997).

In the case of NS-XRBs, we can apply a similar distinction, but the classification is more complex (see Section 2.4 of Ingram and Motta 2019). QPOs in accreting NSs are usually observed at higher frequencies with respect to those detected in BH-XRBs, with high-frequency and low-frequency QPOs in the $100 - 1000$ Hz and $0.1 - 100$ Hz range, respectively. The former are generally referred to as kHz QPOs

(Strohmayer et al., 1996; van der Klis et al., 1996; Ingram and Motta, 2019). kHz QPOs are often found in pairs, like HFQPOs, but they are much more common and they have much larger amplitudes and quality factors. The equivalent of LFQPOs in NS-XRBs are more difficult to classify, due to a much richer phenomenology with respect to BH-XRBs. Historically, in the case of Z-sources (LMXBs accreting at or near the Eddington limit; Hasinger and van der Klis 1989), three different types of QPOs have been identified (van der Klis, 2006): flaring branch oscillations, normal branch oscillations, and horizontal branch oscillations. They are usually considered the equivalent of type-A, type-B, and type-C QPOs, respectively. However, there are also types of QPOs with no equivalent in BH-XRBs, such as QPOs at ~ 1 Hz in Atoll sources (LMXBs accreting at lower accretion rates; see e.g. Altamirano et al. 2008). Although QPOs in NS-XRBs are more common in LMXBs (van der Klis, 2006), they have been detected also in HMXBs at the mHz range (see e.g. Paul and Naik, 2011; Sidoli et al., 2016).

We have seen in Chap. 1 that a peak in the PDS associated with the spin motion of an XRB can give us direct information on the accretor and the system. The physical interpretation, therefore, is usually straightforward, depending on the time scales of the periodicity. Unfortunately, QPOs and other broad features in the PDS can arise from a plethora of phenomena, most of them possibly occuring at the same time. As a consequence, it is harder to understand the underlying physical process(es) simply from the study of the properties of a QPO. Different models have been proposed to describe how QPOs are produced and some of them are discussed in Sect. 2.4 for the case of M51 ULX-7, but the general consensus is that they are related to instabilities and/or geometrical changes in the accretion disk (see e.g. Stella and Vietri, 1998; Stella et al., 1999; Tagger and Pellat, 1999; Ingram et al., 2009). For a general review on the different QPO models I refer the interested reader to Ingram and Motta (2019) and references therein. A model that has been applied and verified multiple times for NS-XRBs in the sub-Eddington regime is the beat frequency model (Lamb et al., 1985; Angelini et al., 1989). In this scenario, the QPO centroid frequency is given by the beating between the orbital frequency $\nu_{\rm orb}$ of the matter at the inner radius of the accretion disk and the spin frequency $\nu_{\rm spin}$ of the accreting NS, that is $\nu_{\rm QPO} = \nu_{\rm orb} - \nu_{\rm spin}$ (see e.g. Dugair et al., 2013, for the case of the QPO at ~ 41 mHz in the BeXRB 4U 0115+634). The beat frequency model can also explain the mHz-QPOs detected in the Galactic PULX Swift J0243.6+6124 when at sub-Eddington luminosities (Wilson-Hodge et al., 2018; Chhotaray et al., 2024). I will show in Sect. 2.4.3 that the model, in its present form, does not work well in the case of M51 ULX-7, suggesting the presence of a different mechanism producing the observed QPOs at super-Eddington luminosities.

This usually explains kHz QPOs in LMXBs

2.2 QPOs in ULXs

First for HFQPOs (Aschenbach, 2004; Remillard and McClintock, 2006) and then for type-C QPOs (Casella et al., 2005, 2008) of BH-XRBs, the presence of QPOs has been proposed to provide a tool for an indirect estimate of the BH mass through timing analysis. In this case, the QPO centroid frequencies are supposed to be linked with nodal precession (LFQPOs), and periastron precession and orbital

frequency (HFQPOs) of the accretion disk. Fig. 2.2 shows an example of these relationships for a selection of detected QPOs. Briefly, the QPO frequencies are expected to scale $\propto 1/M_{\rm BH}$, with lower frequencies at higher BH masses.

The relationships shown in Fig. 2.2 have an important consequence: QPOs in the sub-Hz range, and in particular mHz-QPOs, could indicate that the accretor is a long-sought IMBH. It is for this reason that the detection of mHz-QPOs in M82 X-1 and NGC 5408 X-1 in the early 2000s (Strohmayer and Mushotzky, 2003; Strohmayer et al., 2007; Mucciarelli et al., 2006) was soon interpreted as a confirmation of the IMBH scenario for ULXs. A few years later, Pasham et al. (2014) detected a pair of QPOs for M82 X-1 with a 3:2 frequency ratio. This led them to identify these couple as a scaled-down version of HFQPOs in stellar-mass BHs, thus deriving an estimated mass for the accretor of $M_{\rm BH} \simeq 400\,{\rm M}_\odot$ (see hollow/solid couple of square points in Fig. 2.2). The detection of similar QPOs in other ULXs further strengthened the IMBH scenario. Pasham et al. (2015), for instance, found a similar pair of QPOs in the flux of NGC 1313 X-1, deriving an accretor mass of $M_{\rm BH} \simeq 5000\,{\rm M}_\odot$.

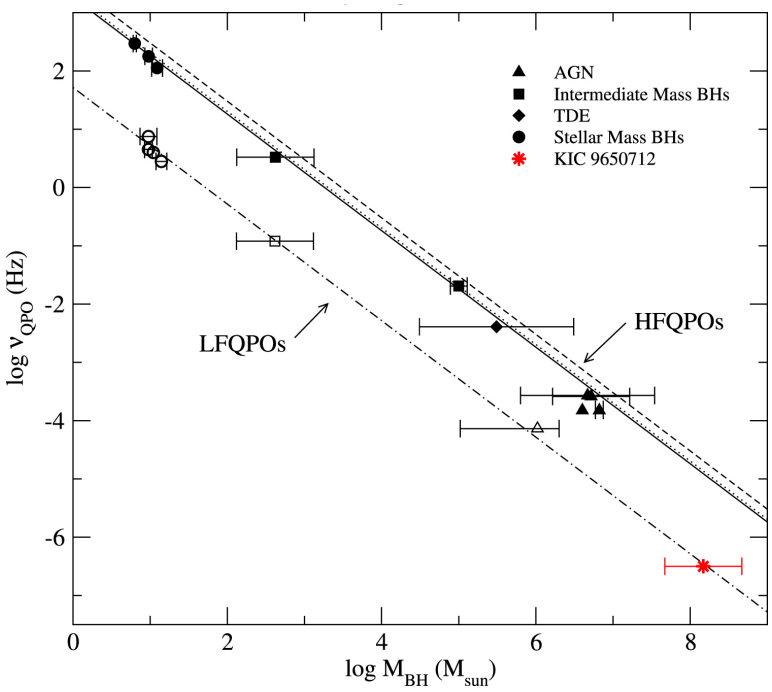

Figure 2.2. Known L(H)FQPOs, represented by the hollow (solid) points, as a function of the BH mass. The solid, dotted and dashed lines show different models of frequency-mass relationship for HFQPOs (Aschenbach, 2004; Remillard and McClintock, 2006), while the dot-dashed line is a fit on LFQPOs performed by Smith et al. (2018). The red point is the candidate QPO analysed in the original paper. Plot taken from Smith et al. (2018).

Pairs of simultaneous QPOs, however, are rarely observed. In most cases when only one mHz-QPO is observed in a ULX, they have been interpreted as the low-frequency equivalent of type-C QPOs in Galactic BH-XRBs. Following the relations shown in Fig. 2.2, one could potentially derive the mass of the accretor from the values shown by Galactic BH-XRBs (which have $M \sim 10\,{\rm M}_\odot$ and typically show

type-C QPOs at frequencies $\nu_0 \sim 1 - 10\,\mathrm{Hz}$). Atapin et al. (2019) reported a collection of ULXs showing both QPOs and flat-top noise, a combination often observed in type-C QPOs. Agrawal and Nandi (2015), for example, reported a QPO at 642 mHz in the X-ray flux of IC 342 X-1 and derived a mass of $\sim 20 - 65\,\mathrm{M}_\odot$. NGC 6946 X-1 shows flat-top noise below 3 mHz and a QPO at 8.5 mHz, which led Rao et al. (2010) to derive a mass $\sim 1000\,\mathrm{M}_\odot$.

There are some problems and caveats with the use of QPO frequencies as a mass proxy, in particular in the case of ULXs, which I will discuss in more detail in Sect. 2.4.3. The best example of the limitations of this method is probably the case of the archetypal PULX, M82 X-2. Until our discovery, M82 X-2 was the only PULX for which a QPO had been detected at super-Eddington luminosities. Feng et al. (2010) reported the discovery of a mHz-QPO in its X-ray flux (source X42.3+59 in their article). The QPO had a centroid frequency $\nu_0 \simeq 3$–$4\,\mathrm{mHz}$, which led them to identify this source as an IMBH with a mass of ∼12,000–43,000 $\mathrm{M}_\odot$. The discovery of pulsations from M82 X-2, however, demonstrates that the source is an accreting NS with a mass $M \simeq 1.4 - 2\,\mathrm{M}_\odot$, casting doubts on other estimates of the mass of ULX accretors through the measure of QPO frequencies.

2.3 M51 ULX-7

We can now turn our attention to the first of the two PULXs I am going to discuss in the remainder of this chapter. First detected by the *Einstein Observatory* (Palumbo et al., 1985), over the years M51 ULX-7 has been also labelled as NGC 5194 X-7 (Roberts and Warwick, 2000), CXOM51 J133001.0+47134 (Terashima and Wilson, 2004), and NGC 5194/5 ULX-7 (Liu and Mirabel, 2005). In the following, I will always refer to this source as ULX-7. It is a well-studied PULX, observed multiple times by X-ray observatories such as *XMM-Newton*, *Swift*, *Chandra* and *NuSTAR* (see Section 2.4.1). It is located in M51, a system of two interacting galaxies, specifically in the larger of the two (also known as the Whirlpool galaxy). The system has a particularly high number of ULXs (at least 9), probably due to the interaction between the two galaxies (Terashima and Wilson, 2004).

add distance of M51
add figure and position of ULX-7 in M51

2.3.1 Spin and orbital parameters

ULX-7 was identified as a PULX when Rodríguez Castillo et al. (2020) discovered coherent pulsations at a period $P_{\mathrm{spin}} \simeq 2.8\,\mathrm{s}$ and a spin-up rate $\dot{P}_{\mathrm{spin}} \simeq -2.4 \times 10^{-10}\,\mathrm{s\,s^{-1}}$ in three out of four *XMM-Newton* observations performed in 2018. The left and middle panels in Fig. 2.3 show the PDSs of the three *XMM-Newton* observations before and after the corrections for the spin-up rate and the orbital Doppler. The temporal solution was found thanks to accelerated search techniques like the one described in Sect. 1.5.2. It is one of the four PULXs, together with NGC 7793 P13 (Fürst et al., 2018, 2021), M82 X-2 (Bachetti et al., 2022) and NGC 5907 ULX-1 (Israel et al., 2017a; Belfiore et al., 2024), with a confirmed orbital solution. Rodríguez Castillo et al. (2020) estimated an orbital period $P_{\mathrm{orb}} \simeq 2\,\mathrm{d}$ and a projected semi-major axis $a_{\mathrm{x}} \sin i \simeq 28\,\mathrm{lt\text{-}s}$ for the system. Assuming a mass $M_{\mathrm{NS}} \simeq 1.4\,\mathrm{M}_\odot$ for the NS, they derived a lower limit for the mass of the companion of $M_{\mathrm{com}} \gtrsim 8\,\mathrm{M}_\odot$ (see also Table 1.1). The orbital period was later confirmed by the detection of periodic

dips in the X-ray flux, suggesting a system inclination angle of $i \sim 60°$ (Hu et al., 2021; Vasilopoulos et al., 2021). This makes ULX-7 the PULX with the shortest known orbital period.

Then you can weight the companion assuming a NS mass in the, e.g., 1.4-2 Msun range

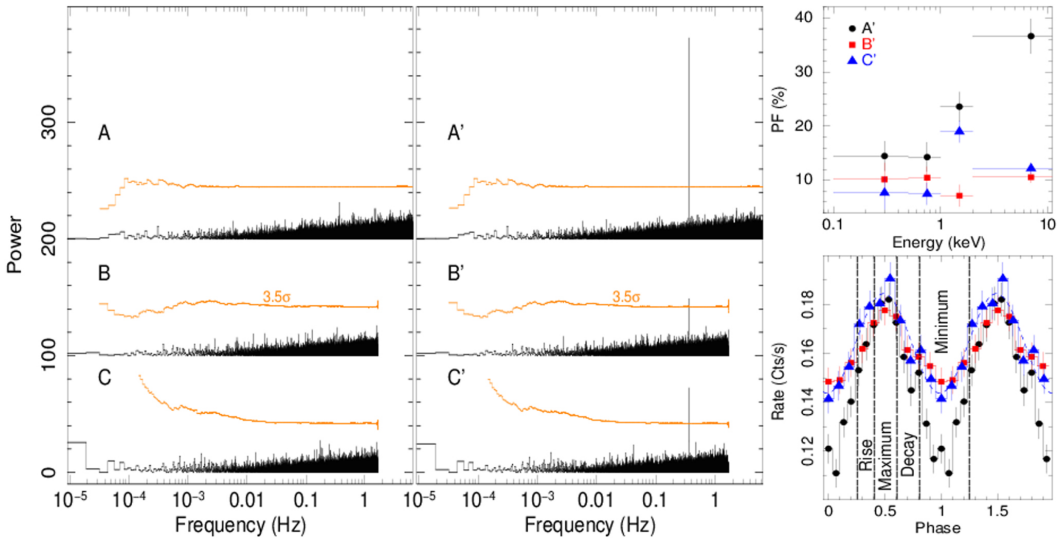

Figure 2.3. Left panel: PDSs of the original 0.1–12 keV ULX-7's light curves of the 2018 *XMM-Newton* observations (A, B, C) during which the pulsations were detected. Middle panel: PDSs of the same light curves after correcting the photon arrival times for both the first period derivative and the orbital Doppler (A', B', C'). The PDSs A, B, A', and B' are arbitrarily shifted along the y-axis for visual purposes. The orange lines represent the 3.5σ detection threshold for each PDS. Right panels: PF of the spin signal as a function of the energy (top) and pulse shape (bottom) during the three 2018 *XMM-Newton* observations. Plot taken from Rodríguez Castillo et al. (2020).

how is it computed?

Among the three observations when pulsations were detected, Rodríguez Castillo et al. (2020) found an average pulsed fraction of the spin signal PF$\sim 5-10\%$. However, the pulse shape is highly variable both in energy and time, as one can see from the right panels in Fig. 2.3. In particular, while below $\simeq 1$ keV the PF of the pulsations is constant and shows little variation among the three observations, this does not hold true at higher energies. Above 1 keV the pulsed fraction can drastically change and be as high as $\sim 40\%$, although during one observation (B' in the plot) its value is consistent with the one at lower energies ($\simeq 10\%$). Fig. 2.4 shows the energy spectra during the four observations of the 2018 *XMM-Newton* campaign. Observation L is the only 2018 observation during which Rodríguez Castillo et al. (2020) did not detect the spin pulsations. It is evident the absence of the hard component in the energy spectrum during observation L. Together with the high variability of the pulsed fraction of the spin signal at high energies, this finding strongly suggests that the pulsations originate from the hard component.

By applying accelerated search techniques to the archival *XMM-Newton* observations, Rodríguez Castillo et al. (2020) found the 2.8 s-long pulsations in two older observations, deriving a secular spin-up rate $\dot{P}_{\rm sec} \simeq -10^9\,{\rm s\,s^{-1}}$. Brightman et al. (2022) later reported the detection of the spin pulsations in a *XMM-Newton* observations performed in 2019, finding a secular spin-up rate consistent with the

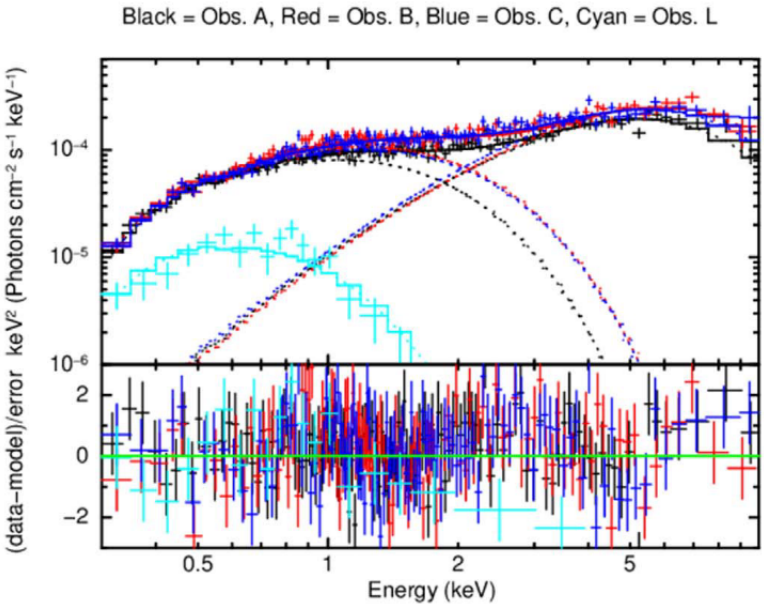

Figure 2.4. ULX-7 unfolded spectra of the four *XMM-Newton* observations performed in 2018. It is clear the absence of the hard component in the energy spectra of observation L, the only one out of the four during the spin pulsations were not detected. Plot taken from Rodríguez Castillo et al. (2020).

one reported by Rodríguez Castillo et al. (2020) and in line with those usually found in other PULXs. Their work also represents the last time ULX-7's pulsations have been detected.

2.3.2 An evolving superorbital period

The X-ray flux of ULX-7 also shows a super-orbital modulation, discovered thanks to a *Swift* monitoring campaign[1] started in 2018. This is a common property among (P)ULXs (see e.g. Lin et al., 2015; Weng and Feng, 2018), with the other PULXs showing a super-orbital modulation being M82 X-2 ($\sim$ 55 d Kong et al., 2016), NGC 5907 ULX-1 ($\sim$ 68 d Walton et al., 2016a), and NGC 7793 P13 ($\sim$ 65 d, Hu et al., 2017; Fürst et al., 2018). Brightman et al. (2020) and Vasilopoulos et al. (2020a) independently estimated a super-orbital period of $\simeq$ 38 d for ULX-7. Rodríguez Castillo et al. (2020) planned and performed the four 2018 *XMM-Newton* observations in two different phases of the modulation, with observations A, B, and C taking place at the peak and observation L at the minimum of the flux.

Brightman et al. (2022) later studied the long-term evolution of ULX-7's super-orbital modulation. The top panel of Fig. 2.5 shows the light curve of the source using data from the first 3 years of the *Swift* monitoring campaign. They found that the initially estimated period of $\simeq$ 38 d had evolved towards longer time scales ($\simeq$ 44 d) after the first 500 days of the campaign. This evolution is reflected in the bottom panel of Fig. 2.5, where the quality of the residuals of the data to the profile gets increasingly worse after 500 days. Through spectral analysis, they also

[1] PI: M. Brightman. The campaign is still ongoing.

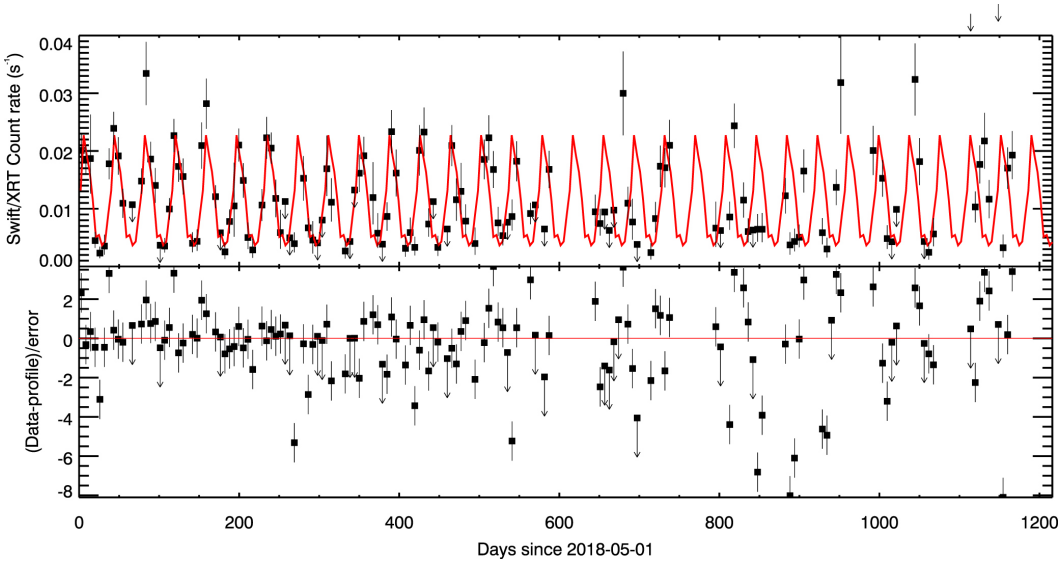

Figure 2.5. Top panel: *Swift* light curve of ULX-7 during the first 3 years of the monitoring program. Superimposed in red is the 38 d-long modulation, with the period estimated using data from the first 500 days. Bottom panel: residuals of the data to the profile. From the residuals, it is clear the change in the super-orbital period happened after about 500 days. Plot taken from Brightman et al. (2022).

found that the inclination of the disk components are dependent on the analysed super-orbital phase. Together with the drastic change in the energy spectrum at the minimum of the modulation (observation L), all these findings suggest the presence of a disk affected by Lense-Thirring precession (see e.g. Middleton et al., 2018).

why? You might give the physical idea here.

2.3.3 2021-2022 *XMM-Newton* campaign

As part of the *XMM-Newton* Large Program "Too B or not too B" (LP hereafter) we observed the field of ~~view of~~ M51, with ULX-7 on-axis, three times (ObsID 0883550101, 0883550201, and 0883550301) between November 2021 and January 2022, for a total (nominal) exposure time of about 390 ks (3x130 ks). Hereafter, I will refer to observations 0883550101, 0883550201, and 0883550301 as observations LPA, LPB, and LPC, respectively. The goal of the LP was to obtain the first estimate of P and $\dot{P}$ since 2019, and to study the evolution of the orbital parameters, in particular $\dot{P}_{\rm orb}$. As shown by Bachetti et al. (2022), this measure can be used as an independent test of the super-Eddington nature of PULXs.

Fig. 2.6 shows a close-up view of the *Swift* long-term light curve of ULX-7 around the time of the LP observations, marked by the grey dashed lines. All three observations were performed at the peak of the super-orbital modulation, when the flux of the source is at its maximum. LPA and LPB were separated by 2 days, while LPC was performed 44 days later, to cover the subsequent cycle. We chose this strategy for several reasons. All the observations were scheduled at the peak of the super-orbital modulation to detect $\sim$ 20000 photons in the PN camera during each 130 ks-long observation. *XMM-Newton* is the best telescope to perform this kind of studies, thanks to a highly elliptical orbit that allows for long, continuous

pn (the EPIC detector pn is lowercase)

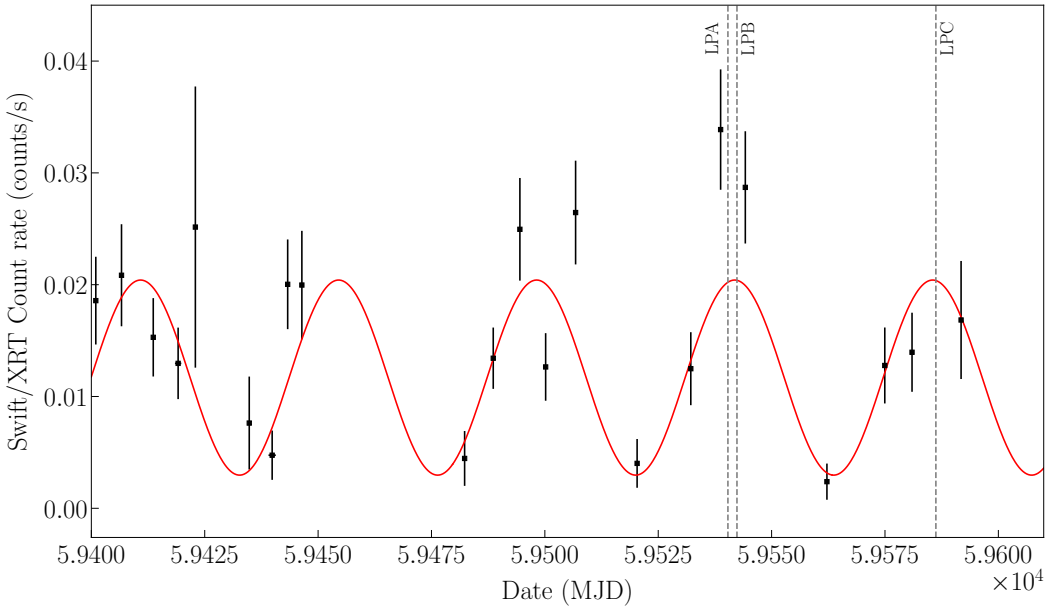

Figure 2.6. Close-up view of the *Swift* light curve of ULX-7 around the time of the three LP's observations. The grey dashed lines show when the observations have been performed. Superimposed in red is the fit of the 44 d-long modulation, to show where are the peaks of the flux. A few cycles are shown to guide the eye. Light curve adapted from the *Swift* monitoring campaign reported in Brightman et al. (2020) and Brightman et al. (2022).

observation of a target up to more than 100 ks (see Section 3.1). Such a long baseline was also needed to maximise the capability of separating a variable $\dot{P}$ component from orbital effects. Given the short orbital period of the system, coincidentally very close to the orbital period of *XMM-Newton*, ULX-7 is the best source to perform this kind of studies. Two close observations at the same peak of the modulation (LPA and LPB) better constrain the local spin-up rate. At the same time, a third distant pointing (LPC) is needed to increase the orbital parameter accuracy at the level required to estimate $\dot{P}_{\rm orb}$ ($\Delta P_{\rm orb} < 0.8$ s).

2.4 Skipping a beat: discovery of persistent QPOs associated with pulsed fraction drop of the spin signal in M51 ULX-7 Imbrogno et al. (2024)

In this paper, we reported on the timing and spectral analyses of the three *XMM-Newton* observations of ULX-7 introduced in the previous section, together with a timing re-analysis of *XMM-Newton*, *Chandra* and *NuSTAR* archival observations. I investigated the spin signal by applying accelerated search techniques and studied the power spectrum through the Fast Fourier Transform, looking for (a)periodic variability in the source flux. We analysed the energy spectra of the 2021–2022 observations and compared them to the older ones.

I discovered a recurrent, significant ($>3\sigma$) broad complex at mHz frequencies in the power spectra of ULX-7. I did not detect the spin signal, setting a 3σ upper limit on the pulsed fraction of $\lesssim 10\%$ for the single observation. These findings represent the first unambiguous detection of QPOs in this source (with tens of cycles sampled) over a baseline of about one month. The complex is significantly detected also in five *Chandra* observations performed in 2012.

ULX-7 represents the second PULX for which we have a significant detection of mHz-QPOs at super-Eddington luminosities. These findings are a reminder that one should avoid using the observed QPO frequency to infer the mass of the accretor in a ULX. The absence of spin pulsations when the broad complex is detected suggests that the mechanism responsible for the aperiodic modulation also dampens the spin signal's pulsed fraction. If true, this represents an additional obstacle in the detection of new PULXs, suggesting an even larger occurrence of PULXs among ULXs.

2.4.1 Observations and data reduction

The M51 field has been observed 45 times with relatively deep, pointed X-ray observations, including 14 observations from *XMM-Newton* (Jansen et al., 2001), 27 from *Chandra* (Weisskopf et al., 2000) and 4 from *NuSTAR* (Harrison et al., 2013). For the analysis, I excluded those observations during which ULX-7 was not detected or detected with less than 100 counts. I also excluded observations lasting less than 20 ks, to ensure the detection of a significant number of cycles of the modulation highlighted above, and observations whose PDSs were dominated by *Chandra* dithering, which introduces spurious signals at $P_{\rm spurious} \simeq 700 - 1000\,{\rm s}$[2] (see e.g. Section 2.3 of Nichols et al., 2010). In Table 2.1 we list the remaining 27 observations (12 from *XMM-Newton*, 14 from *Chandra* and 1 from *NuSTAR*) we analysed and discuss in the following. I used the *Chandra* position (R.A. = $13^{\rm h}30^{\rm m}01\overset{\rm s}{.}02$, Dec = $47°13'43\overset{''}{.}8$, J2000; Kuntz et al. 2016) to convert the event arrival times to the barycentre of the Solar System and extract source events for both *XMM-Newton* and *Chandra*. Unless otherwise stated, in the following the reported errors correspond to 1σ (68.3%) confidence ranges.

XMM-Newton

During observations LPA, LPB, and LPC, ULX-7 was always detected in all the three CCD cameras, with the EPIC PN (Strüder et al., 2001) operated in Full Frame mode (time resolution $\delta t = 73.4$ ms) and both EPIC MOS (Turner et al., 2001) in Small Window mode (time resolution $\delta t = 0.3$ s for the central CCD) to resolve the 2.8 s-long spin pulsations. I used SAS (Gabriel et al., 2004) v21.0.0 with the latest *XMM-Newton* calibrations and applied standard data reduction procedures to prepare the raw data for both timing and spectral analysis. I selected only the events with `PATTERN` ≤ 4 from the EPIC PN data and events with `PATTERN` ≤ 12 from the EPIC MOS data. I considered events in the 0.3–10 keV band for both our timing and spectral analysis. Considering the presence of nearby sources, I selected events for both timing and spectral analysis from a circular region with

[2] https://cxc.cfa.harvard.edu/ciao/why/dither.html

Table 2.1. Log of *XMM-Newton* and *Chandra* observations of M51 ULX-7 analysed in this work.

Satellite	ObsID	Start Date	Exposure[a] (ks)
XMM-Newton	0112840201	2003 Jan 15	20.9
Chandra	3932	2003 Aug 07	48.0
XMM-Newton	0212480801	2005 Jul 1	49.2
XMM-Newton	0303420101	2006 May 20	54.1
XMM-Newton	0303420201	2006 May 24	36.8
Chandra†	13813	2012 Sep 9	179.2
Chandra†	13812	2012 Sep 12	157.5
Chandra†	15496	2012 Sep 19	41.0
Chandra†	13814	2012 Sep 20	189.9
Chandra†	13815	2012 Sep 23	67.2
Chandra	13816	2012 Sep 26	73.1
XMM-Newton	0824450901	2018 May 13	78.0
XMM-Newton	0830191401	2018 May 25	98.0
XMM-Newton	0830191501	2018 Jun 13	63.0
XMM-Newton	0830191601	2018 Jun 15	63.0
NuSTAR	60501023002	2019 Jul 10	162.0
XMM-Newton	0852030101	2019 Jul 12	77.0
Chandra	23472	2020 Oct 13	33.6
Chandra	23474	2020 Dec 21	36.1
Chandra	23475	2021 Jan 28	34.5
Chandra	23476	2021 Mar 1	34.4
Chandra	23479	2021 Jun 7	35.0
Chandra	23480	2021 Jul 13	34.5
XMM-Newton†	0883550101[b]	2021 Nov 22	130.4
XMM-Newton†	0883550201[b]	2021 Nov 24	130.2
XMM-Newton†	0883550301[b]	2022 Jan 7	131.4

Notes.
[a] Pre-flare filtering exposure time. plase add also the post-flare exposure
[b] Observations analysed for the first time for this paper.
† Observations that show the ks-long aperiodic modulation in the power density spectrum with a significance $\geq 3\sigma$.

20″-radius centred on the source position. To properly take into account the diffuse emission in the proximity of ULX-7 and a close chip gap, the background was estimated from an annular region centred on the source position and with inner and
an image, please outer radii equal to 21″ and 39″, respectively. There are X-ray sources within this region, which were excluded from the event selection. Such a small inner radius is usually not recommended for the background region, due to the *XMM-Newton* point spread function. We verified that the contamination from the source is acceptable by considering other circular background regions further away from ULX-7. We found that both the background-subtracted light curve count rates and the spectra parameters are consistent with the ones produced using the annular region. Since the latter better describes the diffuse emission surrounding ULX-7, we preferred our initial choice for the annular background region.

I extracted the high energy ($E > 10$ keV) light curves of the entire field of view to verify the presence of high-background particle flares. To correct for the high-flaring background our observations were affected by, we adopted two different criteria for the timing and spectral analysis. In the first case, considering that the background does not affect the search for the spin signal and to avoid introducing too many gaps in the light curve, I removed only the particle flares at the beginning and/or at the end of the observation. The effective exposure time of our three observations is then reduced to 117.0, 114.1, and 127.1 ks, respectively. The event arrival times were barycentred to the source coordinates using the SAS task `barycen`. The data for timing analysis were background-corrected by the means of the SAS task `epiclccorr`. For the spectral analysis of observations LPB and LPC, we further removed high background intervals occurring in the midst of the observations. As a consequence, the net exposure time for the spectral analysis is further reduced to 72.0, 101.5 and 102.6 ks during observation LPB for the EPIC PN, EPIC MOS1 and EPIC MOS2 data, respectively. In observation LPC, the net exposure is 93.3, 121.3 and 122.9 ks for the EPIC PN, EPIC MOS1 and EPIC MOS2 data, respectively. We discarded the spectra of observation LPA due to a particularly high particle flare contamination. I created response matrices and ancillary files with the SAS tasks `rmfgen` and `arfgen`. Spectra were binned with a minimum of 25 counts per energy bin to allow for fits with a χ^2 statistics. I followed the same data reduction procedure (PATTERN selection, background filtering, barycentric correction and energy spectra extraction) for the archival *XMM-Newton* observations reported in Table 2.1.

Chandra

I downloaded the latest version of the archival data of the M51 field observations. For the data reduction of *Chandra* observations, I employed the *Chandra* Interactive Analysis of Observations (CIAO) software v4.15 (Fruscione et al., 2006) and v4.10.7 of the calibration database. I reprocessed the data with the task `chandra_repro` and I applied the barycentric correction with `axbary`. I then used the `wavdetect` script to verify that ULX-7 had been detected during the observation and to estimate the source extraction region. I extracted the source events by the means of the task `dmcopy`. I considered events in the 0.5–10 keV band for our timing analysis. The radius of the source extraction region depends on the observation, but I verified

give a range

that it was always smaller than 5″. Therefore, I evaluated the background using an annular region centred on ULX-7 and with inner (outer) radius 5″ (20″) for all the observations.

Is this (almost) in continuity with the source extraction region?

NuSTAR

For the data reduction of the *NuSTAR* observation of ULX-7, I followed Brightman et al. (2022). I used `nupipeline` with `saacalc=3`, `saamode=OPTIMIZED`, and `tentacle=yes` to produce cleaned and calibrated events of observation 60501023002, resulting in a net exposure time of 162.0 ks. I selected these settings to account for enhanced background during passages of the South Atlantic Anomaly. I extracted source events in a circular region with a radius of 30″, while background events were extracted from a circular region on the same chip with a radius of 100″. I applied the barycentric correction to the event times of arrival using the `barycorr` task.

2.4.2 Data analysis and results

Timing analysis

I first produced the 0.3–10 keV PN+MOS light curves for each *XMM-Newton* LP observation, with a bin time of 100 s. We report the three light curves in Fig. 2.7, where each column corresponds to a different observation. A recurring, ks-long flaring feature is clearly visible in all three light curves. To study its evolution in energy I considered a soft 0.3–1.5 keV band and a hard 1.5–10 keV band and produced the corresponding light curves following the same procedure. I chose to divide the two bands at 1.5 keV for several reasons. First of all, with this choice each band includes approximately half of the detected events. Secondly, as one can see from Fig. 2.11, it is also approximately the energy at which the curvature of the energy spectra changes, suggesting that the hard component is starting to dominate the emission. The soft (hard) band, therefore, allows us to probe the outer (inner) regions of the disk.

below

I computed the hardness ratio $HR = C_{\rm h}/C_{\rm s}$, where $C_{\rm h}$ ($C_{\rm s}$) is the count rate in the hard (soft) band. The time evolution of the hardness ratio is consistent with it being constant in time. Other choices for the soft/hard band (0.3–1/1–10 keV, 0.3–2/2–10 keV) show the same trend, suggesting that the available data do not allow us to identify a spectral evolution.

In Fig. 2.8 we report the 0.3–10 keV power density spectra (PDSs) corresponding to each of the three LP observations, generated with the `powspec` task in the XRONOS package (Stella and Angelini, 1992), included in the HEASoft v6.32.1[3]. The PDSs were computed with a bin time of 5 s for two reasons: 1) to have a range of frequencies where I could constrain the white noise component of the fit and 2) to avoid cutting the right shoulder of the broad feature, which extends up to ∼0.01 Hz. For these PDSs, I adopted the Leahy normalization (Leahy et al., 1983) and a logarithmic rebin factor of 1.20 (i.e. each bin is 20% larger than the previous one). A broad feature in the (sub-)mHz range, likely associated with the flare-like activity in the light curves, is present in each PDS. I converted the PDSs in XSPEC

[3] https://heasarc.gsfc.nasa.gov/docs/software/lheasoft/

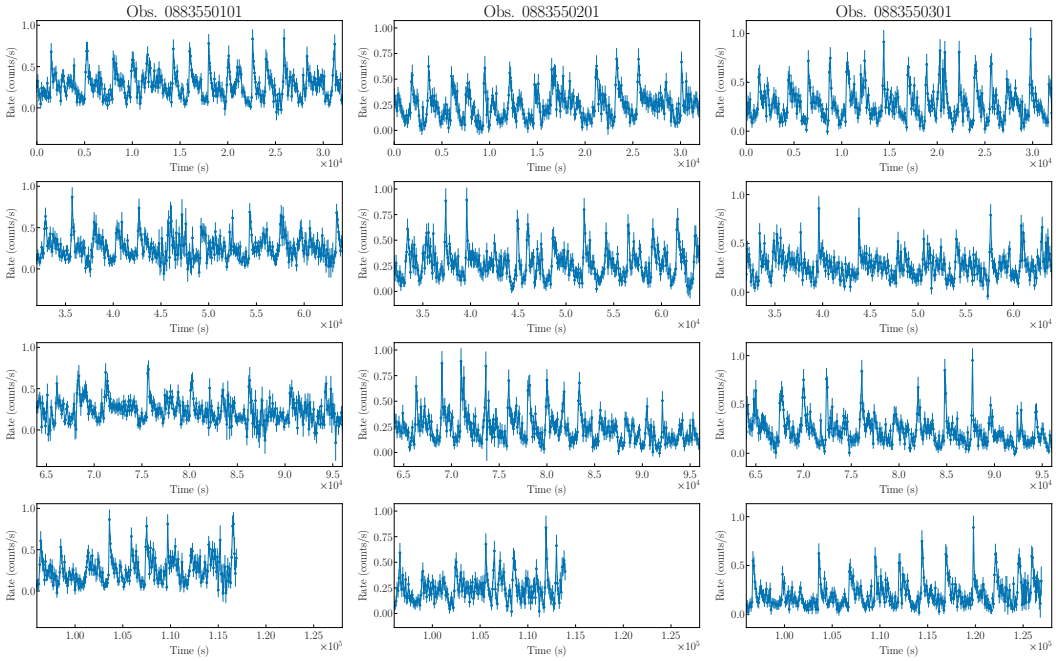

Figure 2.7. PN+MOS light curve of ULX-7 in the 0.3–10 keV band in the three observations of our LP (bin time of 100 s). Each column corresponds to a different observation, while each row shows 32 ks-long chunks of the corresponding observation. From left to right: observations LPA, LPB, LPC.

format to fit them with XSPEC (Arnaud, 1996) v12.13.1, included in the same HEASoft distribution.

I used the χ^2 statistics to estimate the best-fit parameters. I modelled the complex in the mHz range with two Lorentzians, to better describe both the broad shoulder at higher frequencies and the sharper peak at lower frequencies. To model the whole PDS I also considered a constant in order to account for the white noise component that dominates at frequencies $\nu \gtrsim 0.1$ Hz, and a power-law for the red noise component dominant at frequencies $\nu \lesssim 1 \times 10^{-5}$ Hz. The final model used to fit the PDSs is described by the following equation:

$$P(\nu) = \mathrm{const}_{\mathrm{WN}} + K_{\mathrm{RN}}\nu^{\Gamma_{\mathrm{RN}}} + \sum_{i=1}^{2} K_i \frac{\Delta\nu_i}{2\pi} \frac{1}{(\nu-\nu_i)^2 + (\Delta\nu_i/2)^2} \tag{2.3}$$

where $P(\nu)$ is the power P at the frequency ν, the first two terms on the right-hand side describe the white and red noise, respectively, and the summation describes the two Lorentzians. ν_i is the centroid frequency of the Lorentzian and $\Delta\nu_i$ its full width at half maximum (FWHM). In all our fits I found that the white-noise constant and the red-noise, power-law index are consistent with the expected values (using the Leahy normalization) of $\mathrm{const}_{\mathrm{WN}} = 2$ and $-2 \lesssim \Gamma_{\mathrm{RN}} \lesssim -1$, respectively (see e.g. van der Klis, 1989b).

To estimate the significance of the Lorentzians I used two different, independent methods: the F-test as implemented in XSPEC (see e.g. Strohmayer et al. 2007; Strohmayer and Mushotzky 2009), and a procedure similar to the one described in

Motta et al. (2015). For the latter, I converted the PDSs to the square fractional rms normalization (Belloni and Hasinger, 1990) and computed the integral of the power of each Lorentzian. In Motta et al. (2015), they computed the ratio of the integral over the associated negative 1σ error (see footnote 6 in the original work). To take into account any possible non-Gaussianity in the errors, for each Lorentzian component I computed the negative Nσ error for which each integral was consistent with 0. I will first describe the results obtained with the F-test and then those obtained with the Nσ method.

For the F-test, I started from a model with only white and red noise. I found that this model results in unacceptable fits for every observation. I then added a Lorentzian to model the broad shoulder and computed its significance. I found that the fit strongly requires the broad shoulder, with a 4.8σ, 5.5σ, and 6.5σ significance in observation LPA, LPB, and LPC, respectively. With the available data, we cannot exclude that the broad feature is actually an unresolved sum of harmonics, given the highly non-sinusoidal shape of the modulation (see e.g. Angelini et al., 1989). The inclusion of a second Lorentzian to model the sharper peak with respect to the previous model is not strictly required, with a 2.9σ, 2.5σ and 2.8σ significance in observation LPA, LPB, and LPC, respectively. However, we note that if we add the second Lorentzian we consistently obtain better residuals at $\simeq 0.5$ mHz (see lower panels of Fig. 2.8).

It is known that the F-test may provide incorrect results in the case of lines (Protassov et al., 2002). By using the integral approach described above, I found that both Lorentzians (the broad shoulder and the sharper peak) are significant. The broad shoulder is detected with a 3.6σ, 5.0σ, and 4.3σ significance in observation LPA, LPB, and LPC, respectively. The sharper peak is detected at similar confidence levels, with a 3.6σ, 3.2σ, and 4.3σ significance in observation LPA, LPB, and LPC, respectively. Thus, we conclude that we detect both features with a significance $\geq 3\sigma$.

(Motta et al. 2015)

The results of our fits regarding the two Lorentzians, together with the corresponding rms fractional variability, are shown in Tab. 2.2 for the three observations (LPA, LPB, and LPC) separately. Given the little variability shown by the Lorentzians among the three observations, I also fitted the three PDSs simultaneously (LPA+LPB+LPC). The low-frequency feature centred at $\nu_{\rm QPO} \simeq 0.5$ mHz can be classified as a QPO, since $Q_{\rm QPO} \gtrsim 2$ in every observation (and up to 10). The high-frequency feature, on the other hand, always has $Q_{\rm broad} < 2$, therefore I refer to this component as a broad shoulder, or simply as a broad feature. The rms fractional variability of each component is $\mathrm{rms}_{\rm QPO} \simeq 30\%$ and $\mathrm{rms}_{\rm broad} \simeq 40\%$, respectively, and appears stable among the observations. In Tab. 2.2 we also reported for each component the characteristic frequency $\nu_{\rm char} = \sqrt{\nu^2 + (\Delta\nu/2)^2}$ (see e.g. Section 2 of Ingram and Motta, 2019). Although the flare-like activity could lead us to describe the feature as quasi-periodic flarings (QPFs), we opted for the terminology used for other ULXs and classified them as QPOs.

why this is important?

To study the energy evolution of these features I computed the PDSs in the soft (0.3–1.5 keV) and hard (1.5–10 keV) band. We report the results of our fits in Tab. 2.2. In the case of observation LPA, I adopted a geometric rebin of 30%, due to poorer statistics (this observation is highly affected by particle flares). The values found for the different parameters are consistent among the different energy bands.

Table 2.2. Parameters of the Lorentzians obtained from the fit of the 0.3–10 keV, 0.3–1.5 keV and 1.5—10 keV PDSs of our LP observations. ν_x: centroid frequency of the Lorentzian x. $\Delta\nu_x$: full width at half maximum (FWHM) of the Lorentzian x. $\nu_{\mathrm{char},x}$: characteristic frequency of the Lorentzian x. $Q_x = \nu_x/\Delta\nu_x$: approximate quality factor of the Lorentzian x. rms_x: rms fractional variability of the Lorentzian x. Errors given at 1σ (68.3%) confidence level. Two additional components have been added to the fit to take into account the white and red noise at high and low frequencies, respectively.

ObsID	ν_{QPO} (mHz)	$\Delta\nu_{\mathrm{QPO}}$ (mHz)	$\nu_{\mathrm{char,QPO}}$ (mHz)	Q_{QPO}	$\mathrm{rms}_{\mathrm{QPO}}$ (%)	ν_{broad} (mHz)	$\Delta\nu_{\mathrm{broad}}$ (mHz)	$\nu_{\mathrm{char,broad}}$ (mHz)	Q_{broad}	$\mathrm{rms}_{\mathrm{broad}}$ (%)	χ^2/dof
0.3–10 keV											
LPA	$0.449^{+0.019}_{-0.022}$	$0.088^{+0.054}_{-0.035}$	$0.451^{+0.019}_{-0.022}$	5.1	$29.0^{+3.8}_{-4.0}$	$1.20^{+0.26}_{-0.27}$	$2.60^{+0.67}_{-0.53}$	$1.77^{+0.30}_{-0.27}$	0.5	$37.9^{+2.7}_{-2.6}$	27.74/35
LPB	$0.470^{+0.012}_{-0.017}$	$0.046^{+0.053}_{-0.046}$	$0.470^{+0.011}_{-0.017}$	10.2	27.4 ± 4.3	$0.92^{+0.18}_{-0.14}$	$1.65^{+0.31}_{-0.26}$	$1.24^{+0.17}_{-0.13}$	0.6	$38.6^{+2.6}_{-2.7}$	24.23/35
LPC[a]	$0.519^{+0.036}_{-0.033}$	$0.183^{+0.069}_{-0.061}$	$0.527^{+0.036}_{-0.033}$	2.8	32.0 ± 3.6	$1.56^{+0.25}_{-0.23}$	$2.74^{+0.53}_{-0.43}$	$2.08^{+0.26}_{-0.22}$	0.6	40.3 ± 2.6	46.66/37
LPA+LPB+LPC	$0.565^{+0.034}_{-0.036}$	$0.269^{+0.067}_{-0.054}$	$0.581^{+0.034}_{-0.035}$	2.1	29.5 ± 2.4	1.34 ± 0.17	$2.45^{+0.37}_{-0.31}$	$1.81^{+0.18}_{-0.16}$	0.5	36.1 ± 1.8	128.31/124
0.3–1.5 keV											
LPA[b]	$0.534^{+0.024}_{-0.027}$	$0.148^{+0.062}_{-0.081}$	$0.539^{+0.025}_{-0.028}$	3.6	$32.9^{+3.4}_{-4.0}$	$1.48^{+0.18}_{-0.20}$	$1.56^{+0.76}_{-0.53}$	$1.67^{+0.24}_{-0.22}$	0.9	$32.3^{+2.5}_{-3.4}$	32.26/24
LPB	$0.467^{+0.014}_{-0.017}$	$0.061^{+0.052}_{-0.035}$	$0.468^{+0.014}_{-0.017}$	7.6	$29.7^{+4.2}_{-4.5}$	$1.04^{+0.40}_{-0.18}$	$1.21^{+0.76}_{-0.48}$	$1.20^{+0.39}_{-0.19}$	0.9	$29.7^{+3.7}_{-3.5}$	43.13/35
LPC	$0.484^{+0.031}_{-0.028}$	$0.184^{+0.058}_{-0.063}$	$0.493^{+0.031}_{-0.028}$	2.6	$31.8^{+3.5}_{-3.6}$	$1.54^{+0.21}_{-0.24}$	$1.81^{+0.43}_{-0.42}$	$1.79^{+0.21}_{-0.24}$	0.9	33.8 ± 3.2	25.33/35
1.5–10 keV											
LPA[b]	$0.509^{+0.072}_{-0.044}$	$0.25^{+0.22}_{-0.10}$	$0.525^{+0.075}_{-0.045}$	2.0	$36.9^{+5.1}_{-5.5}$	$1.52^{+0.26}_{-0.43}$	$1.21^{+0.66}_{-0.63}$	$1.64^{+0.27}_{-0.42}$	1.3	$32.7^{+7.6}_{-6.3}$	34.30/23
LPB	$0.469^{+0.014}_{-0.022}$	$0.047^{+0.067}_{-0.047}$	$0.470^{+0.014}_{-0.022}$	9.9	25.8 ± 5.3	$1.03^{+0.19}_{-0.18}$	$1.68^{+0.38}_{-0.31}$	$1.33^{+0.19}_{-0.17}$	0.6	$46.3^{+3.8}_{-3.3}$	22.67/35
LPC	$0.538^{+0.028}_{-0.041}$	$0.26^{+0.12}_{-0.10}$	$0.553^{+0.030}_{-0.042}$	2.1	34.6 ± 5.4	$1.27^{+0.71}_{-0.53}$	$4.08^{+0.98}_{-0.81}$	$2.40^{+0.55}_{-0.44}$	0.3	$47.5^{+3.9}_{-4.9}$	34.71/35

Notes.
[a] Due to poor statistics at low frequencies, we froze red-noise parameters at the best-fit values estimated before the addition of the two Lorentzians.
[b] Geometric rebin changed to a factor 30%, due to poor statistics.

Could it be moved earlier?

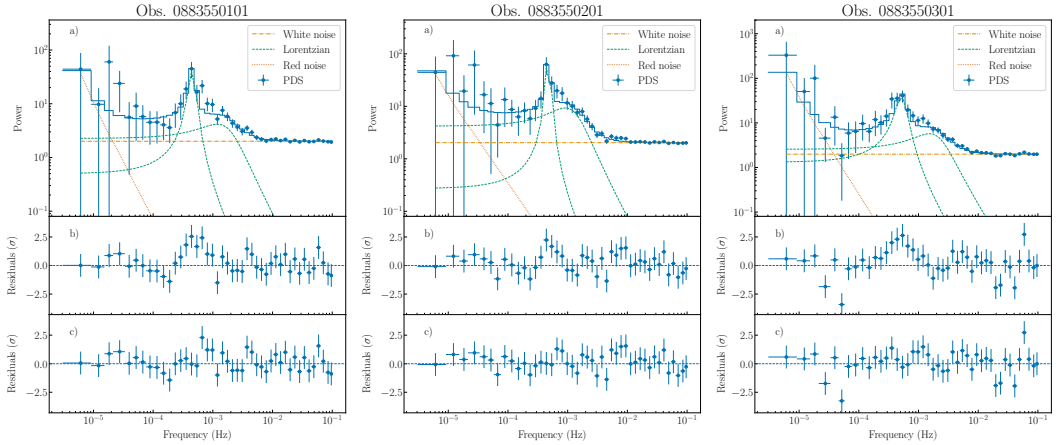

Figure 2.8. PDSs in the 0.3–10 keV band of the LP observations LPA (left), LPB (centre), LPC (right). Panel a: PDS with the components used for the fit. Panel b: residuals of the model without the second Lorentzian. Panel c: residuals of the final model with two Lorentzians. For each observation, we combined data from both PN and MOS cameras. The PDSs are computed using the Leahy normalization. The model we used to fit the PDSs is described by equation (2.3).

I looked for the presence of the 2.8-s spin signal by using acceleration algorithms and also including a first-period derivative component (see Rodríguez Castillo et al. 2020 for more details), but I found no peak associated with a periodic signal, within a reasonable period interval (see below the range for $P_{\rm exp}$), in any of the three PDSs. To derive an upper limit on the pulsed fraction PF of the spin signal, I started from the timing solutions of Brightman et al. (2022) ($P = 2.78674(4)$ s, the last time ULX-7 spin signal was detected, on 2019 July 12) and Rodríguez Castillo et al. (2020) ($P \simeq 2.79771475(25)$ s, on 2018 June 14). From these values I derived a secular spin period derivative $\dot{P} \simeq -3.23(1) \times 10^{-10}\,{\rm s\,s^{-1}}$. In the search I considered a conservative value of $\left|\dot{P}\right| < 10^{-8}\,{\rm s\,s^{-1}}$. The expected spin signal period is, therefore, in the $2.78458 < P_{\rm exp} < 2.7889$ s. Finally, I followed the procedure described by Israel and Stella (1996) to compute the frequency-dependent detection threshold and the 3σ upper limit on $\mathrm{PF}_{\rm range}$ in the 0.350–0.374 Hz range (equivalent to the 3σ confidence range on $\nu_{\rm exp}$), obtaining $\mathrm{PF}_{\rm range} \lesssim 10\%$. The single trial PF upper limit on a sinusoidal signal at $\nu_{\rm exp}$ is $\mathrm{PF}_{\rm single} \lesssim 6\%$.

Could this be put into another sub-section before the spectral analysis?

I then searched for other occurrences of this mHz-complex in the PDSs of the archival X-ray observations I selected according to the criteria outlined in Sect. 2.4.1. The timing analysis of *NuSTAR* observation 60501023002 was already performed by Brightman et al. (2022): neither ULX-7 spin signal nor the mHz-QPOs were detected during this observation.

In Tab. 2.1 we highlighted the observations for which the complex at mHz range has a significance $\geq 3\sigma$. I found 5 consecutive *Chandra* observations, performed between 2012 September 9 and 2012 September 23, during which it was detected. To compute the PDSs, I used a bin time of 3.14 s, equal to *Chandra* time resolution, and close to the 5 s bin time used for the *XMM-Newton* observations. I adopted a logarithmic rebin factor of 1.20 for the three longer observations (ObsIDs 13813, 13812 and 13814). The two shorter observations (ObsIDs 15496 and 13815) needed

Table 2.3. Parameters of the Lorentzian obtained from the fit of the 0.5–10 keV PDSs of the *Chandra* archival observations showing the broad feature in the mHz range. ν_0: centroid frequency of the Lorentzian. $\Delta\nu$: full width at half maximum (FWHM) of the Lorentzian. $\nu_{\rm char}$: characteristic frequency of the Lorentzian. $Q = \nu/\Delta\nu$: approximate quality factor of the Lorentzian. rms: rms fractional variability of the Lorentzian. Errors given at 1σ (68.3%) confidence level. Two additional components have been added to the fit to take into account the white and red noise at high and low frequencies, respectively, unless otherwise stated.

ObsID	ν_0 (mHz)	$\Delta\nu$ (mHz)	$\nu_{\rm char}$ (mHz)	Q	rms (%)	χ^2/dof
13813	$0.97^{+0.11}_{-0.10}$	$1.51^{+0.44}_{-0.32}$	$1.23^{+0.16}_{-0.13}$	0.6	33.1 ± 2.0	29.08/42
13812[a]	$0.94^{+0.10}_{-0.10}$	$1.34^{+0.33}_{-0.26}$	$1.15^{+0.13}_{-0.11}$	0.7	39.8 ± 2.1	45.25/44
15496[ab]	$0.66^{+0.44}_{-0.12}$	$0.8^{+1.5}_{-0.4}$	$0.78^{+0.54}_{-0.15}$	0.8	$31.6^{+6.4}_{-4.2}$	18.90/25
13814	0.83 ± 0.11	$1.17^{+0.39}_{-0.27}$	$1.02^{+0.15}_{-0.12}$	0.7	33.8 ± 2.6	25.27/42
13815[b]	$0.39^{+0.10}_{-0.12}$	$0.60^{+0.27}_{-0.20}$	$0.49^{+0.11}_{-0.12}$	0.7	$41.5^{+2.2}_{-4.3}$	16.39/26

Notes.
[a]For this observation a two-component model (white noise plus Lorentzian in the mHz range) was sufficient to model the PDS.
[b]Geometric rebin changed to a factor 30%, due to poor statistics.

a logarithmic rebin factor of 1.30 for a better fit due to poorer statistics. This is probably a consequence of the shorter exposure times. For these observations, only one Lorentzian was required by the fit. To model the whole PDSs I considered again a constant and a power-law component to account for the white and red noise, respectively. The final model used to fit the *Chandra* PDSs is described by the following equation:

$$P(\nu) = \mathrm{const}_{\mathrm{WN}} + K_{\mathrm{RN}}\nu^{\Gamma_{\mathrm{RN}}} + K\frac{\Delta\nu}{2\pi}\frac{1}{(\nu-\nu_0)^2+(\Delta\nu/2)^2} \tag{2.4}$$

Are these QPOs significant?

where $P(\nu)$ is the power P at the frequency ν, the first two terms on the right-hand side describe the white and red noise, respectively, and the last term is the Lorentzian. ν_0 is the centroid frequency and $\Delta\nu$ its full width at half maximum. The only difference from equation (2.3) is the absence of the summation term, as we are considering just one Lorentzian component instead of two.

We report the results of our fits in Tab. 2.3. Given the low quality factor I derive for the Lorentzian (see Tab. 2.3), we associated it with the broad feature. In Fig. 2.9 we show the evolution of the centroid frequency and the fractional rms of the broad feature and the QPO. Both the frequency and the rms show little variability between the two epochs, albeit separated by almost 10 years.

We also confirmed a different type of variability, first reported by Earnshaw et al. (2016), in an archival *XMM-Newton* observation (ObsID 0303420201), for which we show the 0.3–10 keV light curve and the associated PDS with a logarithmic rebin factor of 1.32 in the top and bottom panel of Fig. 2.10, respectively. In this case, I found that red noise at the low-frequency end of the PDS was not required by the fit. Instead, I fitted the low-frequency tail of the PDS with a Lorentzian centred at 0, finding a width $\Delta\nu = 4.2^{+1.2}_{-1.1}$ mHz (χ^2/dof= 14/24).

Spectral analysis

We analysed ULX-7 spectra from observations LPB and LPC with the XSPEC package (Arnaud, 1996) also used for the fitting of the PDSs. We stress again that we excluded observation LPA for our spectral analysis due to particularly high particle flare contamination. For the computation of the absorption column densities we adopted the element abundances and cross sections of Wilms et al. (2000) and Verner et al. (1996), respectively. The uncertainties reported for the parameters of the considered spectral models represent a 90% confidence range. We computed the absorbed and unabsorbed fluxes in the 0.3–10 keV band using the pseudo-model CFLUX. To derive the unabsorbed luminosities we considered a distance from the source of 8.58 Mpc (McQuinn et al., 2016).

We modelled the spectra with two absorbed multi-temperature disk black bodies (following the approach of previous works, e.g. Gúrpide et al. 2021 and Brightman et al. 2022) using the XSPEC component DISKBB (Mitsuda et al., 1984). For the absorption, we considered two separate TBABS components for the Galactic and intrinsic column densities. The former was fixed to 3.3×10^{20} cm^{-2} (HI4PI Collaboration et al., 2016), while the latter was left free to vary. At first, we fitted the two spectra separately and found the best-fit parameters consistent with each other, indicative of the same spectral state. Hence, we fitted them simultaneously,

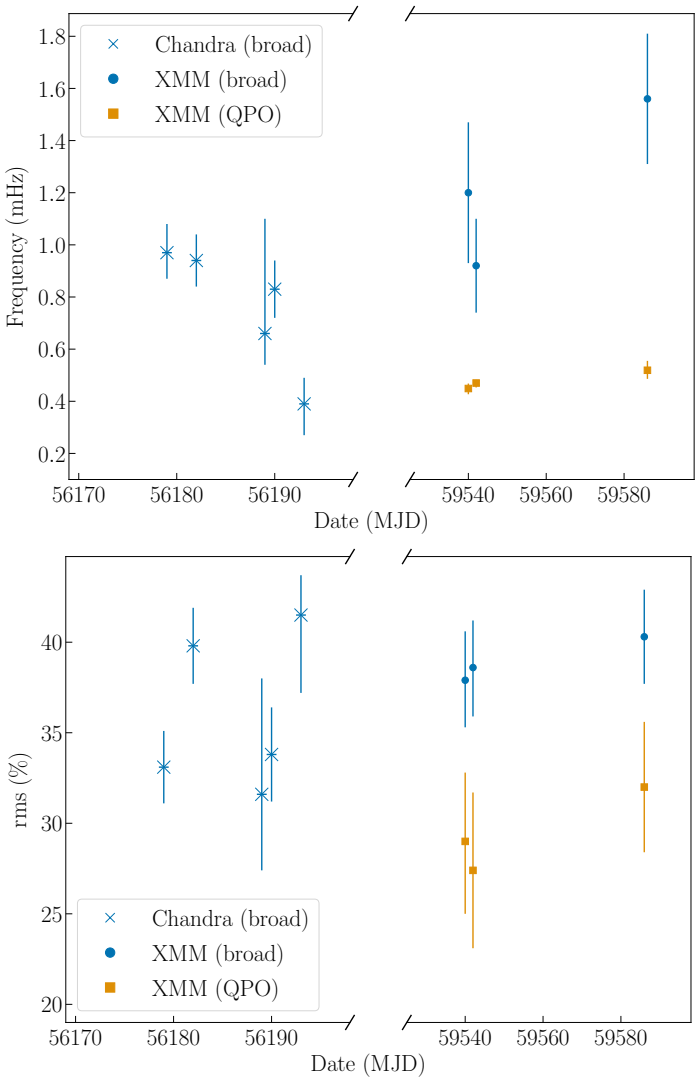

Figure 2.9. Top panel: evolution of the centroid frequency ν. Bottom panel: evolution of the fractional rms. Cross markers represent the values for the broad feature in *Chandra* data, while blue circles and orange squares represent the values for the broad feature and the candidate QPO, respectively, in the latest *XMM-Newton* observations. For *Chandra* we considered events in the 0.5–10 keV band, while for *XMM-Newton* events in the 0.3–10 keV band.

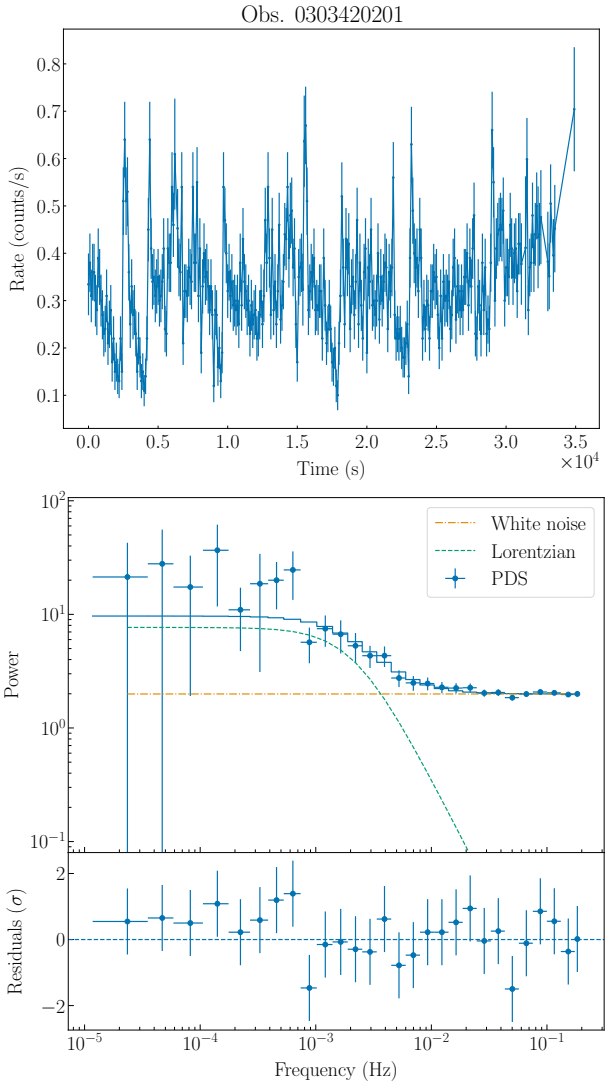

Figure 2.10. Top figure: PN+MOS light curve of ULX-7, *XMM-Newton* observation 0303420201. The bin time is 100 s, as in the three LP light curves. Bottom figure: PDS in the 0.3–10 keV band of *XMM-Newton* observation 0303420201 (top panel) and residuals of the white noise plus single Lorentzian model used for this observation (bottom panel). We combined data from PN and MOS cameras. The PDS is computed using the Leahy normalization.

from the diskbb normalisation (modulo a correction factor) it is possible to estimate the disc size (knowing the distance and the inclination)

to increase the precision on the best-fit parameters. This latter fit resulted in a χ^2/d.o.f. = 607.21/651 and a null hypothesis probability n.h.p.= 0.889, with best-fit temperatures of the two disks of 0.3 keV and $\sim$ 2.7 keV, respectively. All best-fit results are reported in Table 2.4. Both temperatures are consistent with those found for other ULXs (e.g., Gúrpide et al., 2021). A check for intercalibration issues between the cameras, with a multiplicative renormalisation constant in the model, led to non-significant differences in the best-fit parameters, nor in the goodness of the fit.

value and error NH?

We tested the hypothesis of a third spectral component at higher energies, as observed in some ULXs (see e.g. Walton et al., 2018). Following Brightman et al. (2022), who analysed simultaneous *XMM-Newton*+*NuSTAR* observations of ULX-7, we added a cutoff power law to the spectral model (CUTOFFPL). Due to the lack of data at energies above 10 keV, we froze the power law photon index and cutoff energy to the best-fit values of Brightman et al. (2022) of $\Gamma = 0.8$ and $E_{\rm cut} = 8.1$ keV, respectively. This new fit did not significantly improve the statistics compared to the previous one (χ^2/d.o.f. = 607.21/650 and n.h.p.= 0.884), with an upper limit on the power law normalisation of 8×10^{-6} photons keV^{-1} cm^{-1} s^{-1}. Hence, we decided to keep just the two thermal components. Rodríguez Castillo et al. (2020) reached an identical conclusion for previous observations of ULX-7 when only *XMM-Newton* data were available. In general, the cutoff power law is needed only when data above 10 keV are available, and in the case of a NS accretor this component is associated with the emission from the accretion column (see e.g. Walton et al., 2018). We report the spectra of observations LPB and LPC, together with the double-disk model resulting from the simultaneous fit of the two observations, in Fig. 2.11.

For purpose of comparison with Rodríguez Castillo et al. (2020), we also fitted the spectra with a black body spectrum (BBODYRAD) in place of the harder multi-temperature black body component. Also in this case, we first verified that the best-fit parameters were consistent between the two observations and successively we fitted tying all of them together. We obtained a intrinsic absorption of $(5.2^{+1.3}_{-1.2}) \times 10^{20}$ cm^{-2}, a disk black body temperature of 0.48 ± 0.03 keV and a black body temperature of 1.47 ± 0.05 keV. The best-fit statics are χ^2/d.o.f. = 609.66/651 and n.h.p.= 0.875. All values are consistent with the results of the phase-resolved spectroscopy of Rodríguez Castillo et al. (2020), but specifically, the black body temperatures are more consistent with the phases of minimum and raise/decay of the source.

We also noticed marginal evidence for excess residuals at about 1 keV during observation LPB (see Fig.2.11, middle panel). Those residuals are common to ULXs and are interpreted as blended, unresolved spectral lines caused by disk outflows at fractions of the speed of light (see e.g. Middleton et al., 2015) thanks to their unambiguous identification in high-resolution X-ray spectra (see e.g. Pinto et al., 2016; Pinto and Kosec, 2023).

To check for significant spectral differences between different phases of the aperiodic modulation, we extracted the spectra in two different intensity intervals. We defined a "peak" phase whenever the background-subtracted count rate was higher than 0.2 and 0.07 counts s^{-1} in the PN and MOS1/2 camera, respectively, and a "no-peak" phase whenever the count rate was lower. We chose these values since they are a good match to the plateau which can be seen sometimes between a peak and the subsequent minimum in the light curve.

Table 2.4. Best-fit spectral parameters of the latest *XMM-Newton* observations with the double-disk model.

Parameter	LPB	LPC	LPB+LPC
$n_{\rm H}{}^a$ ($10^{20}\,{\rm cm}^{-2}$)	$9.1^{+3.1}_{-2.7}$	$8.1^{+2.5}_{-2.3}$	$8.5^{+1.7}_{-1.8}$
$kT_{\rm soft}$ (keV)	$0.32^{+0.04}_{-0.03}$	0.33 ± 0.03	0.33 ± 0.02
Norm. (soft)	$0.7^{+0.6}_{-0.3}$	$0.6^{+0.4}_{-0.2}$	$0.6^{+0.3}_{-0.2}$
$kT_{\rm hard}$ (keV)	$2.63^{+0.20}_{-0.17}$	$2.78^{+0.21}_{-0.17}$	$2.71^{+0.13}_{-0.12}$
Norm. (hard) (10^{-4})	$5.7^{+1.5}_{-1.3}$	$4.6^{+1.2}_{-1.0}$	$5.0^{+0.9}_{-0.8}$
Flux^b ($10^{-13}\,{\rm erg\,cm^{-2}\,s^{-1}}$)	5.37 ± 0.08	5.37 ± 0.07	5.37 ± 0.05
Lum.^{c} ($10^{39}\,{\rm erg\,s^{-1}}$)	5.34 ± 0.08	5.31 ± 0.07	5.33 ± 0.05
χ^2/dof	297.93/309	306.91/337	607.21/651
n.h.p.	0.664	0.879	0.889

Notes.
[a] The Galactic absorption component was fixed to $n_{\rm H,gal} = 3.3 \times 10^{20}\,{\rm cm}^{-2}$ (HI4PI Collaboration et al., 2016).
[b] Observed flux in the 0.3–10 keV band.
[c] Unabsorbed luminosity in the 0.3–10 keV band.

We fitted the spectra of the observations with the double-disk model used above, first individually and then together. The results of our fits are reported in Tab. 2.5. We found no significant difference in the spectral shape, with the best-fit parameters being consistent with each other within the error bars between the two phases. There is a systematic shift in the normalisations, especially in the soft disk component, albeit barely significant, but this is expected given the choice of the phases based on the count rate. We also computed the unabsorbed flux in the 0.3–10 keV band of the soft and hard disk components separately and in both the peak and no-peak phases. We derived $F^{\rm soft}_{\rm peak} = (1.77 \pm 0.07) \times 10^{-13}\,{\rm erg\,cm^{-2}\,s^{-1}}$ and $F^{\rm soft}_{\rm no-peak} = (1.01 \pm 0.03) \times 10^{-13}\,{\rm erg\,cm^{-2}\,s^{-1}}$ for the soft disk in the two phases, while for the hard disk we derived $F^{\rm hard}_{\rm peak} = (6.68 \pm 0.16) \times 10^{-13}\,{\rm erg\,cm^{-2}\,s^{-1}}$ and $F^{\rm hard}_{\rm no-peak} = (4.12 \pm 0.07) \times 10^{-13}\,{\rm erg\,cm^{-2}\,s^{-1}}$. Both components increase their flux in the peak phase of a factor $\sim$1.7, suggesting that the overall shape of the spectrum remains unaltered.

The spectral analysis of the archival observations showing the broad variability feature has been already performed by Earnshaw et al. (2016). Their results show that ULX-7 has always been detected at a super-Eddington luminosity (few $10^{39}\,{\rm erg\,s^{-1}}$)

Table 2.5. Best-fit parameters of the spectra during the peaks and the minima (no-peak) of the modulation of the latest *XMM-Newton* observations. We considered the same double-disk model as before.

Observation	$n_{\rm H}{}^a$ ($10^{20}\,{\rm cm}^{-2}$)	$kT_{\rm soft}$ (keV)	Norm.	$kT_{\rm hard}$ (keV)	Norm. (10^{-4})	Flux^b ($10^{-13}\,{\rm erg\,cm^{-2}\,s^{-1}}$)	Lum.^{c} ($10^{39}\,{\rm erg\,s^{-1}}$)	χ^2/dof	n.h.p.
LPB									
peak	$10.0^{+5.8}_{-4.7}$	$0.31^{+0.07}_{-0.05}$	$1.1^{+2.0}_{-0.7}$	$2.7^{+0.4}_{-0.3}$	$7.0^{+3.6}_{-2.7}$	7.4 ± 0.2	7.4 ± 0.2	159.28/162	0.546
no-peak	$7.8^{+3.5}_{-3.1}$	$0.34^{+0.05}_{-0.04}$	$0.5^{+0.5}_{-0.3}$	2.8 ± 0.3	$4.0^{+1.7}_{-1.3}$	4.67 ± 0.09	4.61 ± 0.09	288.73/255	0.072
LPC									
peak	$10.8^{+5.1}_{-4.3}$	$0.30^{+0.05}_{-0.04}$	$1.4^{+1.9}_{-0.8}$	$2.9^{+0.4}_{-0.3}$	$5.7^{+2.8}_{-2.1}$	7.30 ± 0.18	7.46 ± 0.18	175.12/180	0.589
no-peak	$5.8^{+3.0}_{-2.6}$	$0.36^{+0.05}_{-0.04}$	$0.32^{+0.28}_{-0.15}$	$2.8^{+0.3}_{-0.2}$	$4.0^{+1.4}_{-1.1}$	4.62 ± 0.08	4.45 ± 0.08	277.37/277	0.482
LPB+LPC									
peak	$10.5^{+3.7}_{-3.2}$	$0.31^{+0.04}_{-0.03}$	$1.3^{+1.2}_{-0.6}$	$2.8^{+0.3}_{-0.2}$	$6.2^{+2.1}_{-1.7}$	7.35 ± 0.13	7.45 ± 0.13	337.69/347	0.63
no-peak	$6.6^{+2.2}_{-2.0}$	$0.35^{+0.04}_{-0.03}$	$0.39^{+0.23}_{-0.14}$	$2.76^{+0.20}_{-0.17}$	$4.0^{+1.0}_{-0.8}$	4.64 ± 0.06	4.52 ± 0.06	567.63/537	0.174

Notes.
[a] The Galactic absorption component was fixed to $n_{\rm H,gal} = 3.3 \times 10^{20}\,{\rm cm}^{-2}$ (HI4PI Collaboration et al., 2016).
[b] Observed flux in the 0.3–10 keV band.
[c] Unabsorbed luminosity in the 0.3–10 keV band.

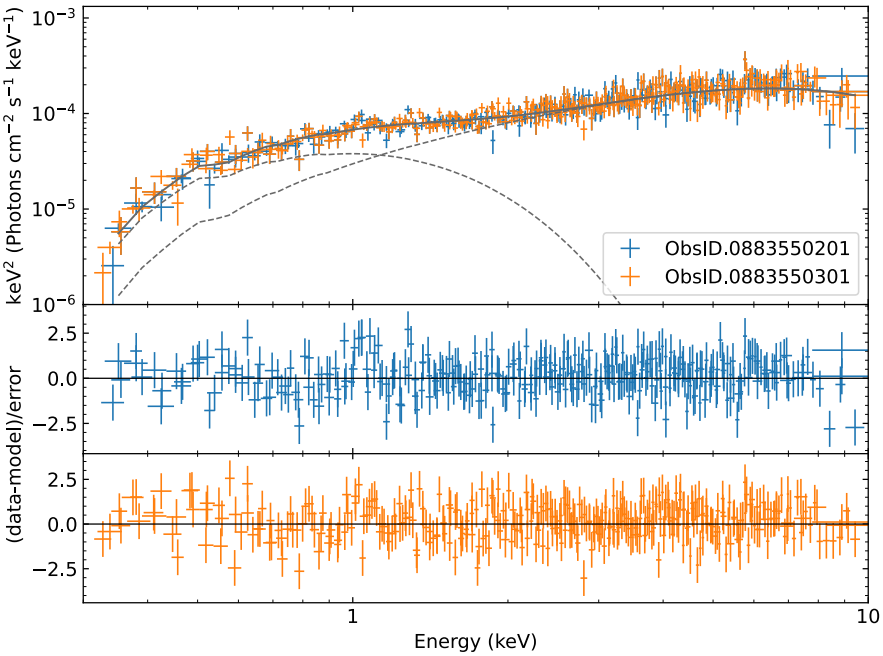

Figure 2.11. Top panel: Simultaneous fit of the two PN+MOS spectra from observations LPB (blue) and LPC (orange) with the double-disk model. Bottom panels: Residuals of the fit in units of standard deviation. Spectra of each colour include PN, MOS1 and MOS2 data (not summed) from the same observation.

in all those observations during which the broad feature in the PDS is detected. They also found that the spectrum of observation 0303420201 (the one showing the different type of variability) can be well described (χ^2/dof = 172.3/182) by a single power-law component with spectral index $\Gamma \simeq 1.45$. The same model, when applied to observations LPB and LPC, results in a worse reduced χ^2, and structured residuals are visible, leading us to rule out the model. With the available data, however, we cannot assess a significant variation in the spectral state. We found that the spectrum in observation 0303420201 can be described equally well (χ^2/dof = 166.9/179) by our double disk model, with parameters consistent with the ones found in observations LPB and LPC. Moreover, other models (such as a blackbody plus power-law model) work equally well for observation 0303420201, suggesting that the statistics are not robust enough to favour one model over the others.

2.4.3 Discussion

The detection of a broad complex in the mHz-range of the PDSs of the 2021-2022 *XMM-Newton* observations marks ULX-7 as the second PULX showing QPOs at super-Eddington luminosities. Moreover, it is the first time this feature is detected in multiple observations over more than one month of baseline, suggesting that, when present, these QPOs are rather stable. By inspecting archival *Chandra* observations, spanning two weeks in 2012 (marked with a dagger in Tab. 2.1), we significantly

($>3\sigma$) detected QPOs with similar properties. It is interesting to note that, even though the two epochs are separated by more than 10 years, the QPOs seem to show very little variation in both the centroid frequency and the fractional rms. Furthermore, observation 0303420201 is the only observation out of 25 during which a flat-top noise best describes the low-frequency variability centred at 0 Hz (see also Earnshaw et al., 2016). The flickering pattern shown by the light curve during this observation was recently noticed also by Kovačević et al. (2022), who suggested a quasi-periodic origin. However, with the available data, we cannot tell whether ULX-7 was observed in a different state or the difference in the PDS arises from the shorter length of the observation (36 ks, compared to our three 130 ks-long observations).

Feng et al. (2010) reported a similar (lack of) evolution in the QPO of M82 X-2. They detected a 3-mHz-QPO in three different *Chandra* observations, performed in 2005, 2007, and 2008, respectively. For our discussion, we do not consider the two *XMM-Newton* observations analyzed by Feng et al. (2010) since, as already pointed out by the authors in their original work, *XMM-Newton* does not have the angular resolution needed to resolve M82 X-2 and M82 X-1 and contamination is always present. For the same reasons, caution is needed when interpreting the tentative detection of 8-mHz-QPOs in M82 X-2 with *XMM-Newton* reported by Caballero-García et al. (2013). The centroid frequency $\nu_{\rm QPO}$, the FWHM $\Delta\nu$ and the fractional rms are all consistent with each other among the three *Chandra* observations analyzed by Feng et al. (2010). The presence of a mHz-QPO with little to no evolution among different epochs, therefore, might represent an interesting property of the PULXs when at super-Eddington luminosities. Given the small sample, we emphasize that at the moment this is only a (tantalizing) hypothesis, to be confirmed by searching for QPOs in other PULXs. To draw a comparison with other super-Eddington pulsars, the Galactic PULX Swift J0243.6+6124 shows QPOs at $\simeq$30–40 mHz only when in the sub-Eddington regime (Wilson-Hodge et al., 2018; Chhotaray et al., 2024). This fact could indicate that PULXs consistently observed at super-Eddington luminosities (such as M82 X-2 and ULX-7) and PULXs showing shorter outbursts at these luminosity levels (such as Swift J0243.6+6124) behave differently.

Although we restricted our analysis to ULX-7 observations where QPOs have a significance $>3\sigma$, it is worth mentioning that other *Chandra* and *XMM-Newton* observations show similar variability in both the light curves and the PDSs. The light curve of *Chandra* observation 354 shows two cycles of a modulation at $\simeq$7620 s (Liu et al., 2002), later confirmed by Yoshida et al. (2010), while *XMM-Newton* observation 0112840201 shows a modulation at a different period ($\simeq$5900 s, Dewangan et al. 2005). Besides, *Chandra* observation 23474 shows 4 cycles of a 10-ks long modulation. In all these observations the significance of the modulation is below the 3σ threshold. For most of them, however, the low significance probably arises from the short length of the observations themselves (typically $\lesssim$ 50 ks), during which very few cycles of the modulation can be probed. 6 out of 8 observations where QPOs were significantly detected are longer than 100 ks.

You should state somewhere (before) how many ULXs have shown QPOs and at which frequency.

Comparison with other sources and possible explanations

The flare-like activity shown in the three light curves of Fig. 2.7 is reminiscent of the heartbeat shown by 4XMM J111816.0–324910 (J1118, see Motta et al., 2020) and of the quasi-periodic "whispers" shown by 4XMM J140314.2+541806 (J1403, see Urquhart et al., 2022). Both sources are ULXs and they both show QPOs at super-Eddington luminosities, the former at a centroid frequency $\nu_{\rm QPO} \simeq 0.4$ mHz and the latter at $\nu_{\rm QPO} \simeq 1.5$ mHz, but neither of them are known to host a pulsar. In the case of J1118, the PDS showed a structured feature, composed of different peaks at 0.3–0.7 mHz, with a low-frequency shoulder at 0.2 mHz. The striking similarity with the heartbeat shown by the Galactic BH binary GRS 1915+105 (see the ρ class variability in Belloni et al., 2000) suggests that limit-cycle instability driven by Lightman-Eardley radiation pressure instability (Lightman and Eardley, 1974) is the source of the modulation. For J1403, several models have been proposed to explain the QPOs: Lense-Thirring precession of an outflow from the inner regions of the disk (Middleton et al., 2019, M19 hereafter); marginally stable He burning from matter accreted on different regions of the surface of the NS (Heger et al., 2007); Lightman-Eardley instability again; beating between the NS spin frequency and the Keplerian frequency ($\nu_{\rm QPO} = \nu_{\rm orb} - \nu_{\rm spin}$) at the inner radius of a disk extending down to the magnetospheric radius $R_{\rm m}$, smaller than the corotation radius $R_{\rm co}$ in order to accrete matter onto the NS. This last model was also proposed to explain the mHz-QPOs seen during super-Eddington flares of LMC X-4 (Moon and Eikenberry, 2001). LMC X-4 is a high-mass X-ray binary (HMXB) that shows parameters similar to ULX-7, with a binary period ≈1.4 d, hosting a NS spinning with a period of ≈13.5 s, spin–up/–down phases at a rate up to $|\dot{P}| \leq 10^{-10}$ s s^{-1}, and a superorbital period ≈30.5 d (see Molkov et al., 2017; Moon and Eikenberry, 2001; Urquhart et al., 2022, and references therein).

This secton is somewhat difficult to follow. Maybe you should discuss each mechanism at a time
* LE instability...
* beat...
...

The Lightman-Eardley instability is hard to reconcile with the differences we see in ULX-7 with respect to J1118. ρ class variability is characterised by a more stable variability pattern than the one we see in the ULX-7 light curves. Besides, we do not see the expected spectral variation in the different phases of the modulation. Our spectral analysis of ULX-7 observations shows no clear evolution in the spectral parameters between the peaks and the valleys of the modulation, apart from a (barely significant) change in the absorption column $n_{\rm H}$, which is higher at the peak of the modulation. J1118, on the other hand, shows a clear evolution among the different phases of the modulation. A higher column density could be the sign of outflows/winds from a slim disk. The presence of winds in ULXs is well established (see e.g. Pinto et al., 2016; Pinto and Kosec, 2023) and excess residuals at $\simeq 1$ keV during observation LPB can be interpreted as an unresolved wind (Middleton et al., 2015). Similar winds from slim disks are also observed in Galactic sources at (super-)Eddington luminosities, such as V404 Cyg (King et al., 2015; Motta et al., 2017). In this scenario, the flares would correspond to quasi-periodic phases where the disk is puffed up and launching the wind, while the out-of-flare emission corresponds to phases when the disk is thinner and not outflowing. This sort of quasi-periodic behaviour would explain the flaring we see in the light curve and the presence of a broad shoulder accompanying the QPOs. It could also explain why, compared with J1118, the flares are less regular and show a higher degree of diversity among

different cycles. A similar scenario was invoked to explain the quasi-periodic dipping observed on 5-10 ks timescales, i.e. matching our findings, in the soft/supersoft source NGC 247 ULX-1 (Alston et al., 2021).

Theoretical works on He burning models predict higher QPOs frequencies ($\sim$ 10 mHz) and a higher rms at lower energies, which we do not detect. Therefore, we will not discuss this possibility any further. Two possible alternative scenarios for the observed QPOs remain to be discussed: Lense-Thirring precession (M19) and the beat frequency model (BFM; see e.g. Lamb et al. 1985; Angelini et al. 1989). We first need to compute magnetospheric and corotation radius for ULX-7:

$$R_{\rm m} = 3.3 \times 10^7 \xi_{0.5} B_{12}^{4/7} L_{39}^{-2/7} R_6^{10/7} M_{1.4}^{1/7} \,{\rm cm} \tag{2.5}$$

$$R_{\rm co} = \left(\frac{GM}{\Omega^2}\right)^{1/3} \simeq 1.5 \times 10^8 \left(\frac{M}{\rm M_\odot}\right)^{1/3} P^{2/3} \,{\rm cm} \tag{2.6}$$

where P is the spin period of ULX-7 in seconds, B_{12} its magnetic dipolar field strength in units of 10^{12} G, L_{39} its luminosity in units of $10^{39}\,{\rm erg\,s^{-1}}$, R_6 its radius in units of 10^6 cm, and $M_{1.4}$ its mass in units of $1.4\,{\rm M_\odot}$. ξ is a parameter that takes into account the geometry of the accretion flow and in the case of an accretion disk is $\approx$0.5 (Ghosh and Lamb, 1979b; Wang, 1987; Campana et al., 2018). From our spectral analysis, we know that the 0.3–10 keV luminosity of ULX-7 is $L_{\rm X} \simeq 5.3 \times 10^{39}\,{\rm erg\,s^{-1}}$. We assume for the radius and mass $R_6 \simeq M_{1.4} \simeq 1$, which are considered typical values for a NS, and for the spin period $P \approx 2.78$ s. If we plug these values into eq. (2.6), we obtain $R_{\rm co} \simeq 3.3 \times 10^8$ cm. In the BFM, a QPO frequency of $\nu_{\rm QPO} \approx 1$ mHz would correspond to a disk (truncated by the magnetosphere) whose inner radius $R_{\rm in}$ is only slightly smaller than $R_{\rm co}$. For simplicity, we can assume $R_{\rm m} \approx R_{\rm in} \approx R_{\rm co}$. From eq. (2.5), we derive a magnetic dipolar field $B \simeq 1.3 \times 10^{14}$ G, inconsistent with previous estimates ($10^{12}\,{\rm G} \lesssim B \lesssim 10^{13}$ G, see Rodríguez Castillo et al. 2020). Another problem with the BFM scenario is that with $R_{\rm m} \approx R_{\rm co}$ we would expect frequent drops in the X-ray luminosity (which we do not detect in ULX-7), since even a small fluctuation in the accretion rate would lead to $R_{\rm m} > R_{\rm co}$ and therefore to the propeller regime. Additionally, a disk's inner radius so close to the corotation radius would require a high level of fine-tuning.

but if R_m is smaller than R_co you will have still accretion and a lower B.
Why should we have an equilibrium rotator with R_m~R_co?
R_M~0.1-0.3 R_co would be enough

For the Lense-Thirring scenario, on the other hand, we follow M19, particularly the values reported in their Table 1. In their work, the mHz-QPOs originated from a precessing inflow with period $P_{\rm inflow}$, and they can be linked with the period of a precessing wind $P_{\rm wind}$. The latter is set equal to the superorbital period we observe in various PULXs, including ULX-7, which shows a superorbital period of $\approx$44 d (Brightman et al., 2022). We can scale the values reported in the first two columns of Table 1 of M19 by the observed superorbital period. By doing so, we find that the frequencies we observe for ULX-7 are consistent with the ones expected for a NS-ULX with a high fraction of energy dissipated to launch the winds ($\epsilon = 0.95$ case). ULX-7's QPO frequency could therefore arise from Lense-Thirring precession of the inner accretion flow. The detection of winds from ULX-7 with a precessing period equal to the superorbital period could further strengthen the hypothesis, particularly if they show up mainly during the observations with QPOs rather than pulsations detected.

You can report these formula also here to ease the reader

Problems with this interpretation arise once we consider the temperature of the cold component of the disk ($T_{\rm sph}$ in M19) and the $P_{\rm wind}/P_{\rm inflow}$ ratio. According to M19, the two quantities can help constrain the magnetic field of the accreting NS powering the PULX (see Fig. 5 in their work). In brief, given $T_{\rm sph}$, the higher $P_{\rm wind}/P_{\rm inflow}$, the lower the magnetic field (see orange curve in Fig. 5 of M19). With $T_{\rm sph} = kT_{\rm soft} \simeq 0.3$ keV (from the spectral analysis of observations LPB and LPC) and $P_{\rm wind}/P_{\rm inflow} \simeq 3800$ (assuming $P_{\rm wind} \simeq 44$ d and $P_{\rm inflow} \simeq 1$ ks), ULX-7 would have an unrealistically low magnetic field $B \ll 10^9$ G. Whilst it is difficult to reconcile such a low field strength with the fact that we see pulsations from the NS, $P_{\rm wind}/P_{\rm inflow}$ is highly sensitive to assumed parameters related to the wind-launching (Middleton et al., 2018, 2019) which may yet permit higher field strengths as a solution.

what is it?

?

The QPO presence is in any way related to the source luminosity?

Conclusion? No model works?

QPOs and pulsed fraction of the spin signal

One interesting feature of the 2021-2022 *XMM-Newton* observations is the non-detection of ULX-7 2.8-s spin pulsations. For this part of the discussion, we will only consider *XMM-Newton* observations, since *Chandra* time resolution (3.14 s in the analysed observations) is not good enough to detect the ULX-7 spin signal. PULXs are known to show transient pulsations, even within the same observation (see e.g. Bachetti et al. 2020, and observation LPB in Fig. 4 of Rodríguez Castillo et al. 2020). Nevertheless, our analysis did not detect the spin pulsations in any intervals of the three observations. Given the high spin derivative $\dot{P}$ typical of PULXs, which can change from observation to observation, we could only compute the 3σ upper limit on the PF considering the single observations. The single-trial value we derived of $\simeq$6% is consistent with the minimum PF detected in 2018 by Rodríguez Castillo et al. (2020), suggesting that, if present, we should have detected the spin pulsations. One could argue that the lack of pulsations may be due to the source being in a different spectral state. The 2021-2022 *XMM-Newton* observations were all performed at the peak of the super-orbital modulation, and our spectral analysis in Sect. 2.4.2 confirms that we observed ULX-7 in a similar state to the 2018 *XMM-Newton* campaign. All the spectral parameters are consistent between the two epochs, with only a 6% difference in the 0.3–10 keV observed luminosity (with respect to 2018 pointing A having a similar flux level). Interestingly, the only difference between the two sets of observations is the presence of the QPOs in 2021-2022. In 2018 the PDSs showed no significant features at the mHz-range. Moreover, after comparison with Tab. 1 of Rodríguez Castillo et al. (2020), we conclude that the QPOs are not present in any of the *XMM-Newton* observations in which the spin pulsations were detected; vice versa, when the QPOs were detected, we do not detect the spin signal. We therefore suggest that, whatever mechanism is responsible for the QPOs, is also responsible for a significant decrease in the pulsed fraction of the spin pulsations, but at the same time does not produce a significant change in the spectral state of the source.

Is this suggestion also true for the other PULX?

The detection of mHz-QPOs in both M82 X-2 and ULX-7 has profound implications for the ULX population as a whole. First of all, it demonstrates that this feature is not exclusive to BH-powered ULXs. The derivation of the mass of the accreting BH from the frequency of the QPOs, therefore, must be treated with extreme caution. Heil et al. (2009) already pointed out that, if the ULX state is

When there is a QPO here you do not need a PL. Is a PL present when there is the pulsation?

different from the sub-Eddington accretion state, mass estimates from the QPO frequencies and PDS features are unreliable. Similarly, Poutanen et al. (2007) had noted that QPOs at mHz-range are also known for Galactic BHs like Cygnus X-1 (Vikhlinin et al., 1994) and GRS 1915+105 (Morgan et al., 1997), weakening the association of mHz-QPOs in ULXs with type-LPC QPOs. Lastly, Middleton et al. (2011) reanalysed *XMM-Newton* observations of NGC 5408 X-1 (one of the ULXs showing mHz-QPOs) and demonstrated that both timing and spectral analysis do not support the IMBH scenario proposed by Strohmayer et al. (2007). Nevertheless, even after these works and the discovery of PULXs, the vast majority of works on ULXs showing QPOs assumes (IM)BH accretors (see e.g. Atapin et al., 2019; Majumder et al., 2023, and references therein).

If QPOs are indeed a PULX signature, they might represent an additional element to single out a candidate PULXs. It is interesting to note, for example, that among the ULXs showing QPOs, there is also IC 342 X-1 (Agrawal and Nandi, 2015), later identified as a PULX candidate by Pintore et al. (2017) based on its hard energy spectrum. Another ULX that shows a similar combination is M74 X-1, with flaring activity in the light curve, high variability among different observations and mHz-QPOs in the PDS (Krauss et al., 2005). The downside is that, apparently, the presence of the QPOs is concurrent with a significant decrease in the pulsed fraction of the spin pulsations. The detection of the spin signal from a PULX is notoriously a difficult task, often involving the use of accelerated search techniques to compensate for the PDS loss of power (at the spin frequency) caused by the huge spin-up of these sources together with orbital Doppler effects (see e.g. the analysis and discussion in Rodríguez Castillo et al., 2020). A QPO could further hinder the process of detecting spin signals.

2.4.4 Conclusions

We have reported on the discovery of persistent QPOs in the mHz-range in three *XMM-Newton* observations of M51 ULX-7 performed in 2021–2022. Concurrently, we did not detect the 2.8 s-long spin signal, with a 3σ upper limit on the pulsed fraction PF $\lesssim 10\%$. These findings represent the second time QPOs are detected in a PULX at super-Eddington luminosities, the first being M82 X-2. We searched for other occurrences of the mHz-feature in M51 ULX-7 archival observations of *XMM-Newton*, *Chandra* and *NuSTAR* and found other 5 *Chandra* observations during which the mHz-feature is significantly ($> 3\sigma$) detected. Our spectral analysis of the 2021–2022 *XMM-Newton* observations shows that the source was observed in a similar state with respect to the 2018 *XMM-Newton* observations when the spin pulsations were first detected (Rodríguez Castillo et al., 2020).

We considered different models proposed to explain similar variability patterns in other ULXs. A disk puffing up and launching winds with a quasi-periodic recurrence could explain the flaring-like light curve and the broad feature in the PDS. Another viable explanation for the mHz-QPOs is Lense-Thirring precession of an outflow from the inner regions of the disk. We note, however, that the latter needs a high level of fine-tuning in the case of M51 ULX-7. Regardless of the correct scenario, the detection of mHz-QPOs from both M82 X-2 and M51 ULX-7 further confirms that one should avoid constraining the mass of the accretor in the ULX from the

observed QPO frequency. The QPOs from both PULXs show little to no evolution in different epochs: more detections from other PULXs are needed to confirm that this is a property of PULXs at super-Eddington luminosities.

In conclusion, we suggest that the presence of mHz-QPOs might also be a common feature of PULXs. However, the drop of the pulsed fraction when QPOs are present further complicates the detection of spin pulsations. This could also mean that the fraction of PULXs over the whole ULX population could be even higher than estimated and that the phenomenology of PULXs is more complex than previously thought. New observations targeting known as well as candidate PULXs will help us better understanding these new phenomena and testing our hypothesis.

2.5 NGC 7793 P13

The discovery of QPOs in M51 ULX-7 has opened a new window on the complex phenomenology of PULXs. At the time of writing (October 2024), I am checking for the presence of QPOs in the mHz range in the X-ray flux of other PULXs, testing the hypothesis advanced in the previous section that the mechanism responsible for the aperiodic feature is also responsible for a significant drop in the pulsed fraction of the spin signal. The search has already been successful, since I found a mHz-QPO with similar properties to the one described in Sect. 2.4 in the X-ray flux of another PULX, that is NGC 7793 P13 (Imbrogno et al., in prep.). The work is still in progress, thus after a description of the source I will only summarise the main results I obtained so far.

2.5.1 The fastest known PULX: spin and orbital parameters

NGC 7793 P13 (hereafter P13) is a PULX located in the outskirts of NGC 7793, a galaxy in the Sculptor group (Fabbiano et al., 1992) at a distance $d \simeq 3.4\,\mathrm{Mpc}$ (Zgirski et al., 2017). First discovered and identified as a ULX by Read and Pietsch (1999) thanks to *ROSAT* observations, it is regularly observed by all the major X-ray observatories, such as *XMM-Newton*, *NICER*, *NuSTAR* and *Swift* at luminosities $L_\mathrm{X} \simeq 5 \times 10^{39} - 10^{40}\,\mathrm{erg\,s^{-1}}$. It has a companion of spectral type B9I (Motch et al., 2011) and it was initially classified as a super-Eddington BH with $M \lesssim 15\,\mathrm{M_\odot}$ (Motch et al., 2014). Two years later, Fürst et al. (2016) and Israel et al. (2017b) independently discovered pulsations at a period $P \simeq 420\,\mathrm{ms}$ in its X-ray flux (see Fig. 2.12) by analysing *XMM-Newton* and *NuSTAR* observations. Such a short period makes P13 the fastest known PULX. Israel et al. (2017b) discovered P13's spin signal thanks to a systematic and automated search for new pulsators in the *XMM-Newton* archival data. I am currently involved in the continuation of this data mining project, as I will describe in Chap. 3.

P13 has a particularly low spin-up rate for a PULX. Both Fürst et al. (2016) and Israel et al. (2017b) could only put an upper limit on the instantaneous spin-period derivative of $|\dot{P}| \lesssim 10^{-10}\,\mathrm{s\,s^{-1}}$. By studying the secular evolution of the spin period with data ranging from 2013 to 2016, they both estimated a secular spin-up rate $\dot{P}_\mathrm{sec} \simeq -3.5 \times 10^{-11}\,\mathrm{s\,s^{-1}}$. Later, Fürst et al. (2021) presented a detailed study of the long-term evolution of P13 from 2013 to 2021. They found that after 2016 $\dot{P}_\mathrm{sec}$ had remained constant and that the NS is continuously spinning up. This latter

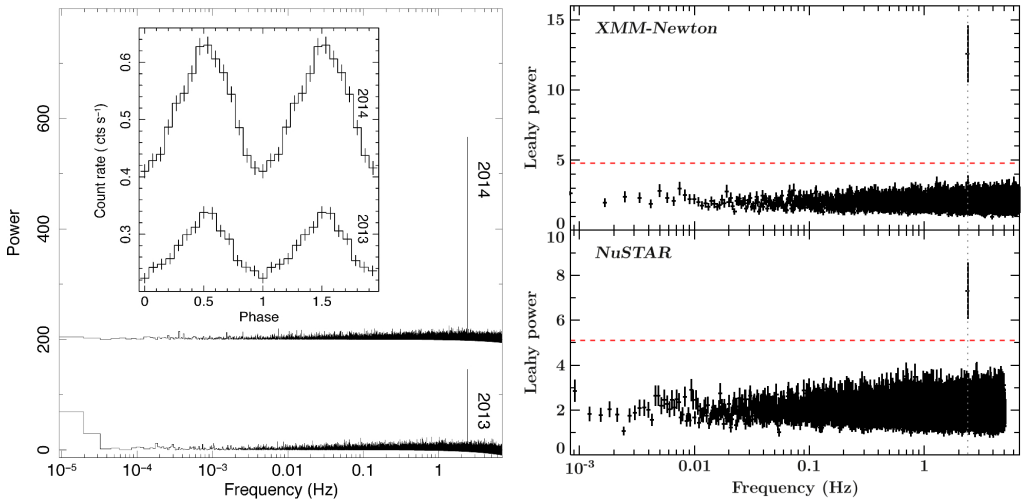

Figure 2.12. Top panel: PDSs of the 2013 (bottom) and 2014 (top) *XMM-Newton* EPIC PN data, analysed within the framework of the EXTraS project. It is clear the signal peak at approximately 0.42 s (2.4 Hz). The 2014 PDS was shifted along the y-axis for visual purposes. The inset shows the background-subtracted, folded pulse profile during the two observations. Plot taken from Israel et al. (2017b). Bottom panel: PDSs of the 2016 *XMM-Newton* (top) and *NuSTAR* (bottom) data. The red dashed lines represent the 5σ detection threshold. The grey dotted line marks the frequency of the pulsations at $\simeq 2.4$ Hz. The *XMM-Newton* and *NuSTAR* PDSs are the result of the average of 39 and 34 independent PDSs, respectively. Plot taken from Fürst et al. (2016).

discovery was quite puzzling, since the observed X-ray flux had dropped significantly in 2019, with the source remaining in an "off-state" in 2020 and 2021. The flux recovered to intermediate levels only in 2022.

Unlike other PULXs, P13's spin signal is easily detected in almost every observation with sufficiently good time resolution. Fürst et al. (2021) found an anti-correlation between the X-ray flux and the pulsed fraction PF of the spin signal, which can be as high as $\sim 60\%$ (and usually $\gtrsim 10-20\%$, see Table 1 of Fürst et al. 2021). As for ULX-7, the PF increases with energy, although the growth flattens above 5 keV (see Figure 3 of Fürst et al. 2016 and Figure 2 of Israel et al. 2017b).

Fürst et al. (2018) performed a study to determine the orbital ephemeris of the system, later refined in Fürst et al. (2021), trying to solve a long-standing issue. The optical/UV and X-ray light curves, in fact, show a modulation at two similar but different periods, with $P_{\rm opt} \simeq 64$ d and $P_{\rm X} \simeq 65$ d. It is usually assumed that the orbital period of this system is the one estimated by the optical/UV data $P_{\rm opt}$. The X-ray modulation at period $P_{\rm X}$ would then be super-orbital in nature, as observed in other PULXs. Timing analysis of the spin pulsations initially found that the spin period shows a modulation at a period $P_{\rm Doppler}$ consistent with $P_{\rm opt}$: this consistency is easily explained in terms of orbital Doppler, supporting the scenario where $P_{\rm opt}$ is the true orbital period of the system (Fürst et al., 2018). However, a few years later Fürst et al. (2021) refined the estimate of $P_{\rm Doppler}$ and found a value inconsistent with their previous work, obtaining a period closer to $P_{\rm X}$. At the moment, $P_{\rm opt}$ is still considered the best estimate of the orbital period of the system, but a physical interpretation of this inconsistency is still lacking.

2.5.2 A work in progress: mHz-QPOs in NGC 7793 P13

Last year, we organised a campaign of quasi-simultaneous observations of P13 in the optical and X-ray bands. The primary objectives were to characterise the multi-wavelength emission of P13 and to search for the first time for optical pulsations from a PULX. The latter objective is made possible thanks to the fast optical photometers SiFAP2 (Ghedina et al., 2018), mounted at the Telescopio Nazionale Galileo (TNG), and HiPERCAM (Dhillon et al., 2021), mounted at the Gran Telescopio CANARIAS (GTC). Such a search is the first of its kind in the study of PULXs. In this campaign, I am the PI of the TNG and *NICER* observations for the optical and X-ray observations, respectively. The optical observations are still being analysed and will be the subject of a separate work (Imbrogno et al., in prep.).

While preparing for the campaign, I checked the archival observations of P13 and found a mHz-QPO in the X-ray flux of *XMM-Newton* observation 0804670601, performed in June 2017. Fig. 2.13 shows the averaged PDS of the corresponding EPIC PN data, binned at the maximum available time resolution of $\delta t = 73.4\,\mathrm{ms}$. The PDS in the figure was obtained by dividing the observation into 18x1600 s intervals and computing the average of the PDSs of each interval. It is clear the presence of a QPO at a frequency $\simeq 0.01\,\mathrm{Hz}$.

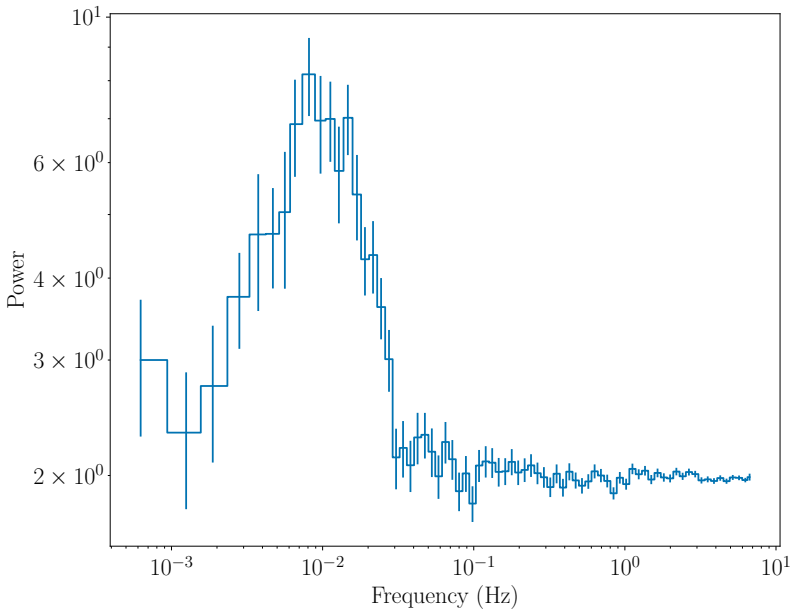

Figure 2.13. Averaged PDS in the 0.3–10 keV band of the EPIC PN data from *XMM-Newton* observation 0804670601. The PDS is computed using the Leahy normalization.

After this discovery, I checked for other occurrences of (mHz-)QPOs in P13's archival observations. I focused on *XMM-Newton*, *Chandra*, *NICER*, and *NuSTAR* observations during which P13 was detected with at least 100 counts. I excluded those observations lasting less 3 ks, unless other observations from the same satellite, for a total combined exposure $> 3\,\mathrm{ks}$, were available less than a day later. The choice was guided by the need to detect a significant number of QPO cycles, as done for ULX-7. 45 observations (6 from *Chandra*, 18 from *XMM-Newton*, 13 from *NuSTAR*,

and 8 from *NICER*) passed this selection phase. Table 2.6 reports the observations during which P13's X-ray flux shows a QPO. I grouped observations separated by less than approximately one month in the same epoch. With this division, I found 5 epochs during which a QPO was detected by *XMM-Newton*, *NICER*, and *NuSTAR*. The detection of this feature in three different telescopes, with different time resolutions and electronics, at different epochs assures us that the mHz-QPO is real and not due to instrument-specific issues. The centroid frequency, in fact, is in a range in which spurious signals can be present in *XMM-Newton* data, due to a counting mode issue (see Chap. 3). This possibility could already be excluded, since, when present, these spurious signals are detected for every source in the field of view, which is not our case. However, the simultaneous detection by different instruments further supports an astrophysical origin of the QPO.

Table 2.6. Log of the analysed observations of NGC 7793 P13 that show the QPO.

Satellite	Epoch[a]	ObsID	Start Date	Exposure Time (ks)
XMM-Newton	X1	0804670401	2017 May 31	34.0
XMM-Newton	X1	0804670501	2017 Jun 12	35.1
XMM-Newton	X1	0804670601	2017 Jun 20	32.5
NICER	XNNu2	1050420101	2017 Oct 30	1.2
NuSTAR	XNNu2	90301326002	2017 Oct 31	51.9
NICER	XNNu2	1050420102	2017 Oct 31	10.5
XMM-Newton	XNNu2	0804670701	2017 Nov 25	53.0
XMM-Newton	X3	0823410301	2018 Nov 27	28.0
NuSTAR	Nu4	50401003002	2019 Nov 18	43.2
NICER	XN5	6050420101	2023 Nov 6	2.6
NICER	XN5	6050420102	2023 Nov 7	4.0
NICER	XN5	6050420103	2023 Nov 8	3.7
XMM-Newton	XN5	0922840201	2023 Dec 6	60.4

Notes.
[a] Observations less than approximately one month apart were considered as part of the same epoch. X = *XMM-Newton*, N = *NICER*, Nu = *NuSTAR*.

I have shown in Sect. 2.4 that the mHz-QPO of ULX-7, whenever it is present, is persistent and has a constant centroid frequency. P13's QPO has very similar properties. When present the feature always shows the same centroid frequency $\nu_{\rm QPO} \simeq 10\,{\rm mHz}$. This mHz-QPO is also persistent: during epoch XN5 it was detected during *NICER* and *XMM-Newton* observations separated by one month. Fig. 2.14 shows the mHz-QPO in two different epochs. The top panel shows the average PDS of *NICER* observations 1050420101, 1050420102, and 1050420103 from epoch

XN5. The joint *NICER* dataset was divided into 8x1024 s intervals, with a time resolution of $\delta t = 0.01$ s. The PDS in the figure is the average of the PDSs computed for each interval. The bottom panel, on the other hand, shows the average of 44 PDSs computed from as many 512 s-long intervals of the *XMM-Newton* observation 0823410301 ($\delta t = 73.4$ ms).

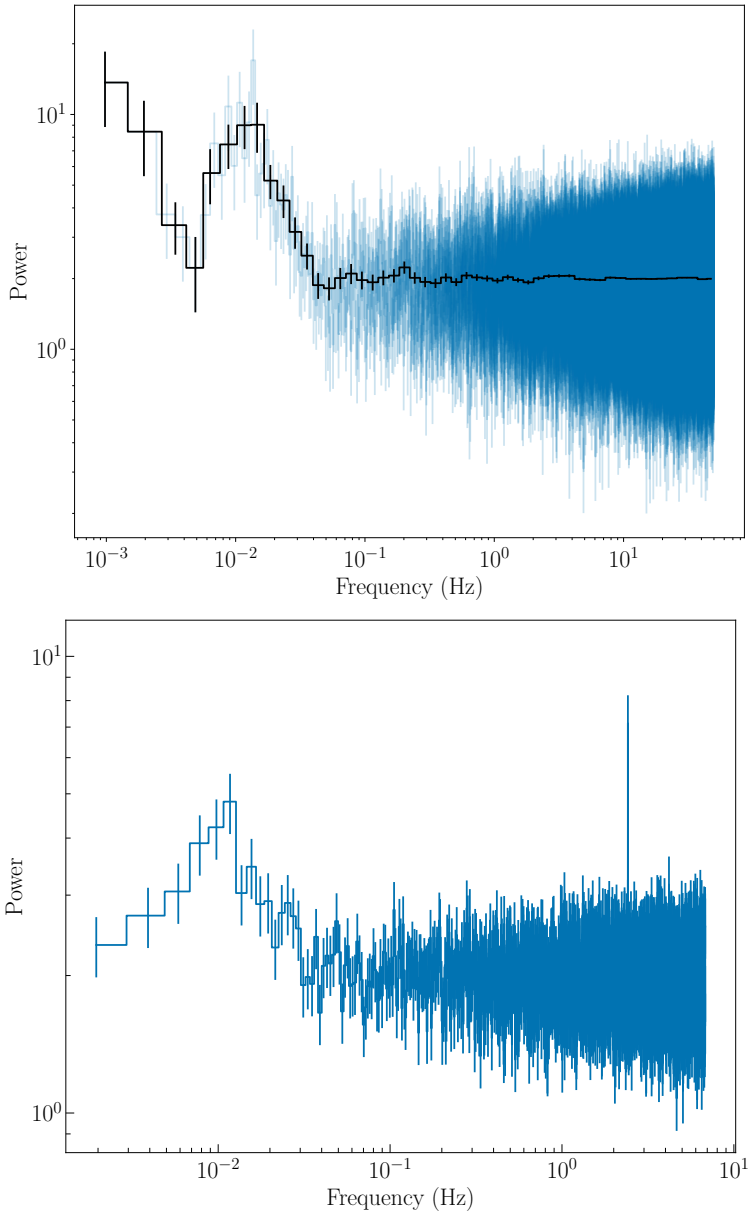

Rebin

Figure 2.14. Top panel: Averaged PDS in the 0.3–10 keV band of the joint data from *NICER* observations 1050420101, 1050420102, and 1050420103. Both the original average of the 8 PDSs (blue) and a rebinned version (black, rebinning factor 1.20) are shown. Bottom panel: PDS in the 0.3–10 keV band of the EPIC PN data from *XMM-Newton* observation 0823410301 ($\delta t = 73.4$ ms). In this observation, both the QPO at 0.01 Hz and the spin signal at 2.4 Hz are detected. All the PDSs are computed using the Leahy normalization.

It is interesting to note that during observation 0823410301 both the mHz-QPO and the spin signal are present (bottom panel in Fig. 2.14). A comparison with Table 1 of Fürst et al. (2021) shows that when the QPO is detected the pulsed fraction PF of the spin signal is $\simeq 10-15\%$, lower than usual ($> 20\%$). This further supports the hypothesis that the mechanism responsible for the production of the mHz-QPO, whatever it is, is also responsible for a significant decrease in the PF. The higher mean PF with respect to ULX-7's spin signal ($\simeq 5-10\%$) could explain why in this case we can still detect the pulsations. If the initial PF is already small, as in the case of ULX-7, a decrease can easily lead to a misdetection. If the initial PF is high enough, on the other hand, the signal can still be detected, but at a much lower pulsed fraction. At the same time, however, the mHz-QPO is also present in two observations (50401003002 from *NuSTAR*, 0823410301 from *XMM-Newton*) during which the PF of the spin signal is $\simeq 63\%$ and $\simeq 46\%$, respectively (Fürst et al., 2018). These two observations were performed during the onset of the off-state, which could indicate that something had changed in the physical properties of the system, but a deeper analysis is needed to understand if it also affected the QPO properties.

I would say that your suggestion about the mutual exclusion of QPOs and spin period should be at least toned down, since one observation is enough to invalidate it.
Indeed, the XMM observations would eventually suggest for a decrease in the PF, not a firm exclusion. Then, the NuSTAR observation would, in my opnion, definitely state that they can coeaxist.

Chapter 3

The power of data mining

The most exciting phrase to hear in science, the one that heralds new discoveries, is not "Eureka!" but "That's funny..."

Isaac Asimov

In parallel with the study of PULXs, in the last three years I have been taking part in data mining projects whose goal is to identify serendipitous pulsators in the X-ray missions archives. Projects like these are becoming increasingly crucial in order to exploit the ever-growing X-ray astronomical archives. In this chapter, I will first focus on one of these projects, mainly developed by the high-energy groups at the astronomical observatories of Rome (OAR) and Brera (OAB), which led, among other results, to the discovery of NGC 7793 P13's spin signal in the archival data of *XMM-Newton* (Israel et al., 2017b). Finally, in the last section of the chapter I will describe my contribution to this and other data mining projects during these years.

3.1 Mining the *XMM-Newton* archive

The last version of the *XMM-Newton* catalogue, that is 4XMM–DR14[1], was released on 2024 July 9th and contains 13 864 observations with more than 10^6 detections of 692 109 sources. With respect to the previous version (4XMM–DR13[2]) the catalogue contains 621 new observations and 35 112 new sources. Until the release of eRASS1 at the beginning of 2024, the *XMM-Newton* catalogue represented the largest archive for an X-ray telescope and it has been steadfastly growing over the years, as shown in Fig. 3.1.

XMM-Newton has a unique combination of properties that makes this telescope particularly suited for the temporal variability characterization of even the faintest sources in the 0.2–12 keV band[3]:

- 3 European Photon Imaging Cameras (EPIC; 1 EPIC PN and 2 EPIC MOS)

[1] http://xmmssc.irap.omp.eu/Catalogue/4XMM-DR14/4XMM_DR14.html.
[2] http://xmmssc.irap.omp.eu/Catalogue/4XMM-DR13/4XMM_DR13.html.
[3] See the user manual available at the following website: https://xmm-tools.cosmos.esa.int/external/xmm_user_support/documentation/uhb/index.html.

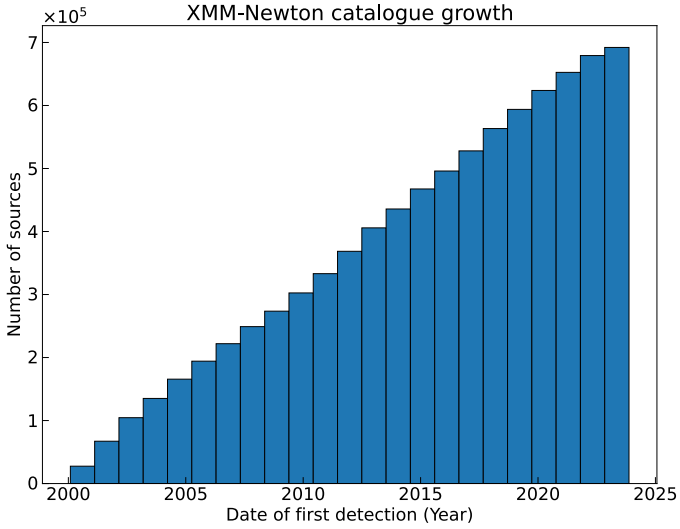

Figure 3.1. Evolution in time of the number of unique sources detected by *XMM-Newton*. Based on the 4XMM–DR14 version of the *XMM-Newton* catalogue.

with imaging capabilities. The three cameras can work simultaneously, for a field of view of $\simeq 30$ arcmin;

- a good angular resolution, with a full width at half maximum of $\simeq 6$ arcsec;
- a high effective area ($\simeq 2500\,\mathrm{cm}^2$ at 1.5 keV), which at the time of the launch in 1999 was the highest effective area ever for an X-ray telescope (see Fig. 3.2 for a comparison with other telescopes);
- the possibility for a long, continuous visibility of the target, thanks to a highly elliptical orbit with exposure times as long as $T_{\mathrm{max}} \simeq 130$ ks.

The combination of long exposure times and high effective area allows for the detection of sources down to a flux of $\sim 10^{-16}\,\mathrm{erg\,cm^{-2}\,s^{-1}}$. The three cameras can operate with different science modes. In this and the following chapter, we are interested in those modes with imaging capabilities, for which typical sample times for the three cameras are $\delta t_{\mathrm{pn}} \simeq 73.4$ ms and $\delta t_{\mathrm{MOS}} \simeq 2.6$ s. By looking at the relations in Sect. 1.5.2, in particular eq. (1.28), one can see that *XMM-Newton* potentially allows for the Fourier analysis and the search for periodic signals in a wide range of frequencies, from $\nu_{\mathrm{min}} \simeq 10\,\mu$Hz (for an observation with length $T \sim 100$ ks) to $\nu_{\mathrm{max}} \simeq 6.7$ Hz (for the EPIC PN).

3.2 The EXTraS project

The standard identification procedure performed by the *XMM-Newton* Survey Science Center does not include a search for short-term periodic variability in the flux of the newly discovered sources. An *XMM-Newton* field of view can include up to $\sim 100 - 200$ sources, most of them serendipitous. Many new X-ray pulsators, therefore, can end up in the *XMM-Newton* archive without being recognised as such.

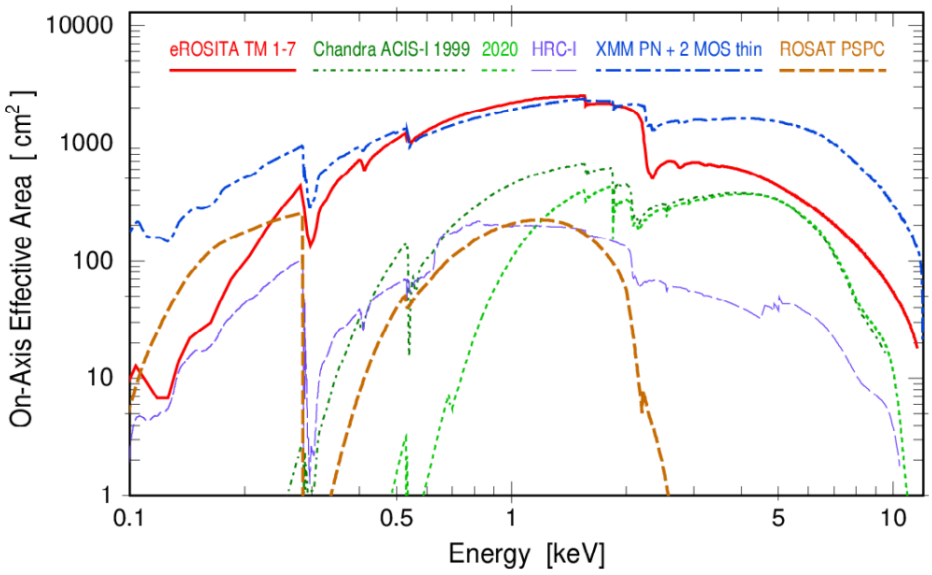

Figure 3.2. *XMM-Newton* effective area (blue dot-dashed line) compared to other X-ray telescopes. Plot taken from Predehl et al. (2021).

The Exploring the X-ray Transient Sky (EXTraS) project (De Luca et al., 2014, 2021) was designed to fill this gap and to characterise from a temporal point of view the unidentified sources in the *XMM-Newton* archive. EXTraS was funded from 2014 to 2016 by the European Union within the Seventh Framework Programme (FP7-Space) and it was the result of the collaboration of six partners:

- **INAF** (Istituto Nazionale di Astrofisica), which was the coordinator of the project with three involved institutes: IASF (Istituto di astrofisica spaziale e fisica cosmica) in Milan, the Astronomical Observatory of Rome (OAR) and the Astronomical Observatory of Brera (OAB);
- **IUSS** (Istituto Universitario di Studi Superiori) from Pavia;
- **CNR–IMATI** (Consiglio Nazionale delle Ricerche – Istituto di Matematica Applicata e Tecnologie Informatiche);
- **University of Leicester**, whose Leicester Database and Archive Service (LEADAS) provided the bases for the public EXTraS archive. EXTraS provided also a public science gateway[4] to retrieve the EXTraS products (D'Agostino et al., 2019);
- **MPG–MPE** (Max Planck Gesellschaft zur Foerderung der Wissenschaften E.V.– Max Planck Institute for Extraterrestrial physics), involved in the development, test and calibration of *XMM-Newton*'s onboard instruments;
- **FAU-ECAP** (Friedrich–Alexander Universitat Erlangen-Nuremberg - Erlangen Center for Astroparticle Physics).

[4]The archive and the science gateway, due to IT security issues, is not available anymore to the public. The EXTraS products can be accessed by contacting the original coordinators at OAB. IASF

Both the OAR and the OAB had previously coordinated two similar data mining projects, also aimed at characterizing the temporal variability of X-ray sources in the *Swift* and *Chandra* archives: the *Swift* Automatic Timing Survey at Brera And Rome astronomical observatories (SATS@BAR, Esposito et al. 2014b, 2015), and the *Chandra* ACIS Timing Survey at Brera And Rome astronomical observatories (CATS@BAR, Israel et al. 2016b). Both projects applied systematic and automated searches for new X-ray pulsators, based on the Fourier analysis of the *Swift* and *Chandra* archival data. In particular, CATS@BAR led to the identification of 41 new X-ray pulsators, with spin periods ranging from $P \simeq 8\,\mathrm{s}$ to $P \simeq 60\,\mathrm{ks}$ (see Table 1 from Israel et al. 2016b).

The EXTraS project included 4 different lines of research:

- **short-term, aperiodic variability**, aimed at detecting aperiodic phenomena, such as bursts, flares, and dips, on timescales from the time resolution δt of the cameras up to the length T of the analysed observation;
- **coherent pulsations**, which is going to be the subject of the next section;
- **transient sources**, usually missed by the standard image analysis performed by the *XMM-Newton* Survey Science Center since these sources are above the detection threshold only for a short time interval;
- **long-term variability**, combining multiple observations of a source whenever available.

The version of the *XMM-Newton* catalogue analysed within the framework of the EXTraS project was 3XMM–DR4, which included all the *XMM-Newton* observations performed by December 2012. More than $\sim 400\,000$ source detections were analysed, resulting in a total of ~ 20 millions product files (light curves and PDSs among the others).

3.2.1 EXTraS search for coherent pulsations

Although the project officially ended in 2016, the developed pipelines are still routinely applied to the newly available *XMM-Newton* observations (typically once a year). This extension is known as the post-EXTraS phase of the project. In this section, I will briefly describe the aforementioned pipeline (see also Section 4 of De Luca et al., 2021).

Data from all the *XMM-Newton* cameras, the EPIC PN and the two EPIC MOS, are analysed. To optimize the search for periodic signals, only time series with more than 50 counts are considered. As already discussed in Chap. 1 and shown by eq. (1.32), the higher the detected photons, the lower the minimum detectable pulsed fraction of a periodic signal. Additionally, the search is performed directly on the photon arrival times rather on the binned light curve. This choice maximises the range of analysed frequencies, typically from a minimum detectable period of $\sim 150\,\mathrm{ms}$ up to the highest value allowed by the length T of the observation.

First of all, the time series are ordered in decreasing time resolution δt. If the ratio $T/\delta t > 2 \times 10^6$, that is the time series binned at the maximum time resolution has more than 2 million time bins, the analysis is splitted in two modes: the maximum

Fourier resolution (MFR) mode, in which the time resolution is decreased so that $T/\delta t \simeq 2 \times 10^6$; and the maximum Nyquist frequency (MNF) mode, in which the original sampling time is fixed but the observation is divided in two or more intervals, each with $\lesssim 2 \times 10^6$ time bins.

For each time series, the pipeline computes the PDS using the XRONOS task `powspec` (Stella and Angelini, 1992). The pipeline includes also a logarithmic smoothing algorithm that computes the frequency-dependent detection threshold following the prescriptions outlined by Israel and Stella (1996). The threshold is set at a significance of 3.5σ. In case of detection, the script saves the Fourier period $1/\nu_j$ of the signal, its pulsed fraction, computed according to eq. (1.32), and the probability of the associated peak arising from noise. In case of a non-detection, the pipeline computes the 3σ upper limit on the pulsed fraction. Finally, in case of a detection, the code refines the signal characterization and saves all the information in a database that the user can use later to check for the presence of new signals.

There are some known downsides and/or limitations to this approach, as for any algorithm. First of all, the background contribution is not subtracted from the time series before the computation of the PDSs. This does not affect the search for periodic signals, since a constant background rate does not affect the signal power and the smoothing algorithm deals with the non-Poissonian noise. However, it does affect the computation of the pulsed fraction, which must be considered a lower limit and evaluated differently.

Another issue is the number of trials considered for the computation of the significance of a detection. In principle, the significance probability should take into account all the frequencies of all the PDSs computed for all the sources analysed. This is, however, impractical in our case. (Post-)EXTraS is a living project, whose pipelines are still routinely applied. The total number of analysed frequencies is and will be unknown as long as the project continues. The statistical properties are therefore computed for each individual time series. A good number of these sources have been or can be observed by multiple telescopes (*Chandra*, *NuSTAR*, *Swift* just to name a few), therefore the presence of the signal can be independently confirmed with the data coming from other missions. Additionally, since *XMM-Newton* has 3 EPIC cameras that can independently observe the target, the presence of the signal in more than one camera offers a check for the goodness of the candidate.

Finally, instrument artefacts can always be present and difficult to avoid. In particular, the distribution of periods of the signals discovered by EXTraS shows a peak at $\sim 20 - 200\,\mathrm{s}$. Most of them are spurious signals arising from an issue with the EPIC cameras switching back from the counting mode (a safe mode triggered by very high count rates). Older versions of the data reduction software (SAS, Gabriel et al. 2004) could not manage this mode properly and produced an incorrect reconstruction of the arrival time of the photons. Most of the spurious signals disappears when the data are reduced with newer versions of the software (v13.5 or later, see Appendix A in De Luca et al. 2021). However, some of these artefacts can still be present. A visual check is always recommended to check the goodness of the detection. In this case, the spurious signals can be recognised by the fact that multiple sources in the same observation show pulsations at the same period, a strong suggestion that they are instrumental artefacts.

3.2.2 A selection of notable EXTraS discoveries

When EXTraS ended in 2016, more than 5×10^5 time series had been analysed, leading to the discovery of 40 new X-ray pulsators. Among them, there are two PULXs: NGC 7793 P13 (Israel et al., 2017b), which is the fastest known PULX, and NGC 5907 ULX-1 (Israel et al., 2017a), the most luminous and most distant known PULX. Now that we are in the post-EXTraS phase and the pipeline has also been applied to the new observations, the number of new X-ray pulsators discovered is 60 (Rodríguez Castillo et al., in prep.). In this section, I report a selection of notable examples, to show the potentialities of the project.

I do not think it is needed here.
It is work done by others before this thesis.

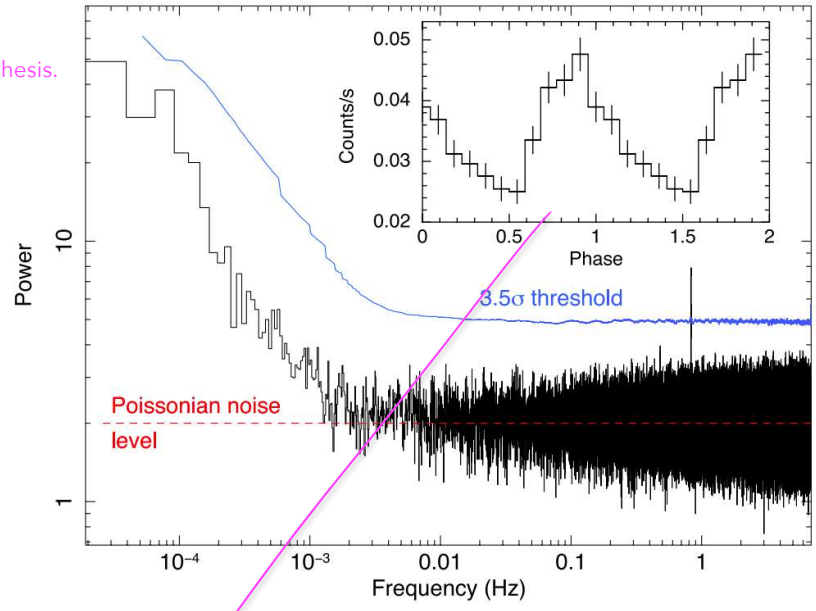

Figure 3.3. PDS of the whole EPIC PN dataset, spanning from 2000 December to 2013 February, of 3XMM J004301.4+413017. The 1.2-s signal is recognisable above the detection threshold (blue). The red dashed line shows the Poissonian noise level. The inset shows the signal profile during observation 0650560301, when pulsations were first detected. Plot taken from Esposito et al. (2016).

Despite its proximity, its similarities with the Milky Way and the extensive X-ray monitoring, the first two accreting NSs in M31 were discovered thanks to EXTraS. 3XMM J004301.4+413017 (Esposito et al., 2016) is a NS with a spin period $P \simeq 1.2$ s. The signal was first detected in a *XMM-Newton* observation from 2011 and later found in multiple observations, spanning a time range of 13 years (see Fig. 3.3). Thanks to these multiple detection it has been possible to derive the orbital parameters of the system (see Table 2 of Esposito et al. 2016), which has an orbital period $P_{\rm orb} \simeq 1.27$ d. The lack of a bright optical counterpart suggests that the system is either a low-mass XRB (LMXB), with a companion weighing $M \lesssim 1\,{\rm M}_\odot$, or an intermediate-mass XRB, with a companion with $M \sim 2\,{\rm M}_\odot$.

3XMM J004232.1+411314, instead, is the most luminous hard source in M31 ($L \sim 4 \times 10^{38}\,{\rm erg\,s^{-1}}$ in the 0.5–50 keV band), representing the total emission from the galaxy above ~ 20 keV (Yukita et al., 2017). It was first identified by EXTraS

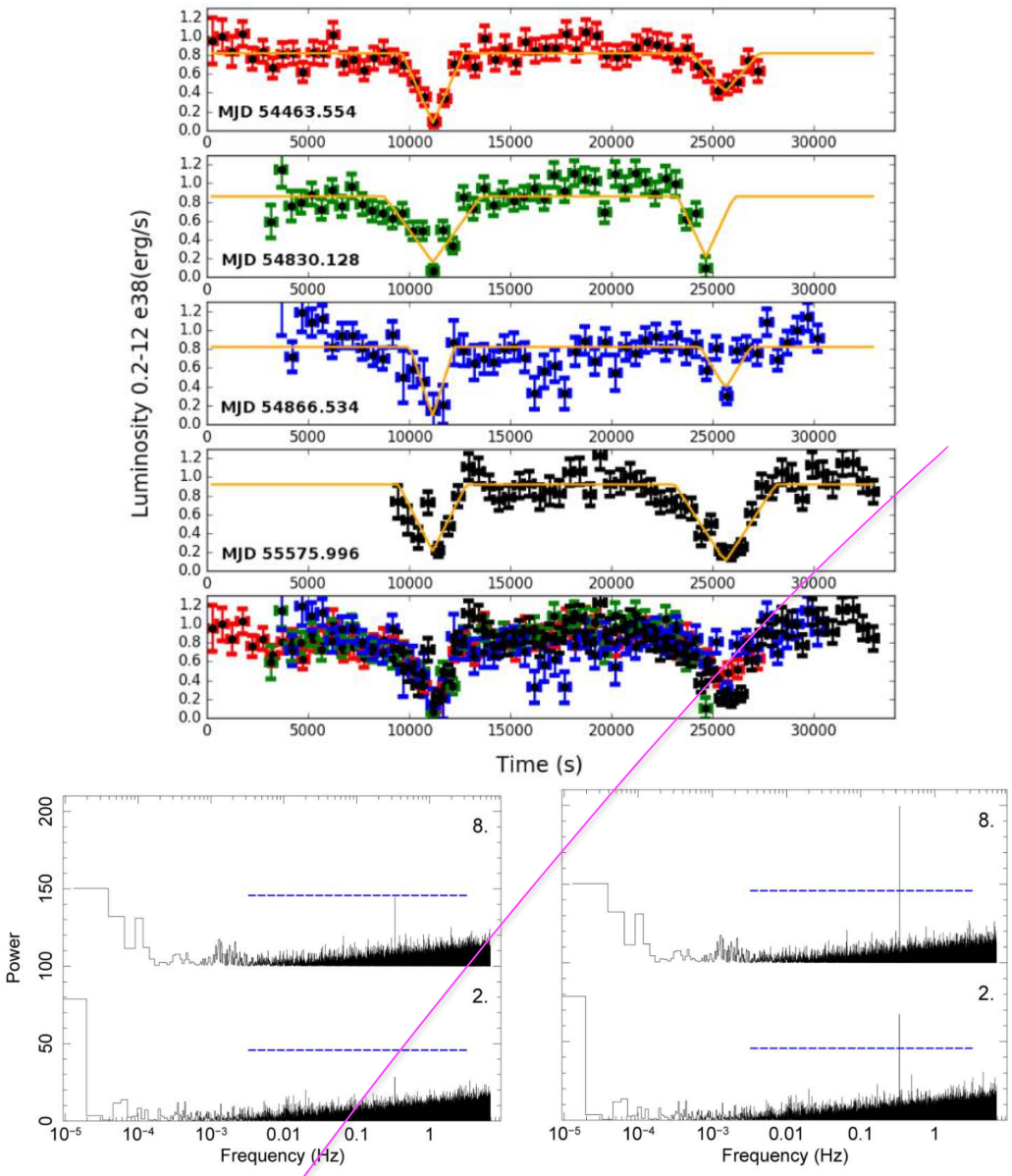

Figure 3.4. Top panel: *XMM-Newton* light curve of 3XMM J004232.1+411314 during observation 0505720201 (red markers), 0551690201 (green markers), 0551690601 (blue markers), and 0650560401 (black markers), during which two dips are visible. A superimposition of the four light curves is also shown. Each light curve is aligned so that the first minimum occurs at the same time. Plot taken from Marelli et al. (2017). Bottom panel: the PDSs on the left are computed from the EPIC PN data of observations 0112570101 (2) and 0764030301 (8). The PDSs on the right are computed from the same data but after correcting the photon arrival times for the orbital solution found by Marelli et al. (2017). The blue dashed line is the 3.5σ detection threshold. Plot taken from Rodríguez Castillo et al. (2018).

as a dipping source, with 13 dips in 40 *XMM-Newton* observations. In 4 of these observations *XMM-Newton* detected two dips separated by a period of $P_{\rm orb} \simeq 4\,{\rm hr}$, as shown in Fig. 3.4 (Marelli et al., 2017). This period is probably the orbital period of the system: together with the lack of massive ($M \gtrsim 3\,{\rm M}_\odot$) stars in the field and the hard spectrum, the most likely explanation is that the system is a LMXB seen at an inclination $i \sim 60° - 80°$. Rodríguez Castillo et al. (2018) later refined the orbital parameters and their results supported the LMXB scenario, suggesting a companion with $M \simeq 0.3\,{\rm M}_\odot$. Thanks to an accelerated search as the one described by eq. (1.31), they also detected the spin pulsations at $P \simeq 3\,{\rm s}$.

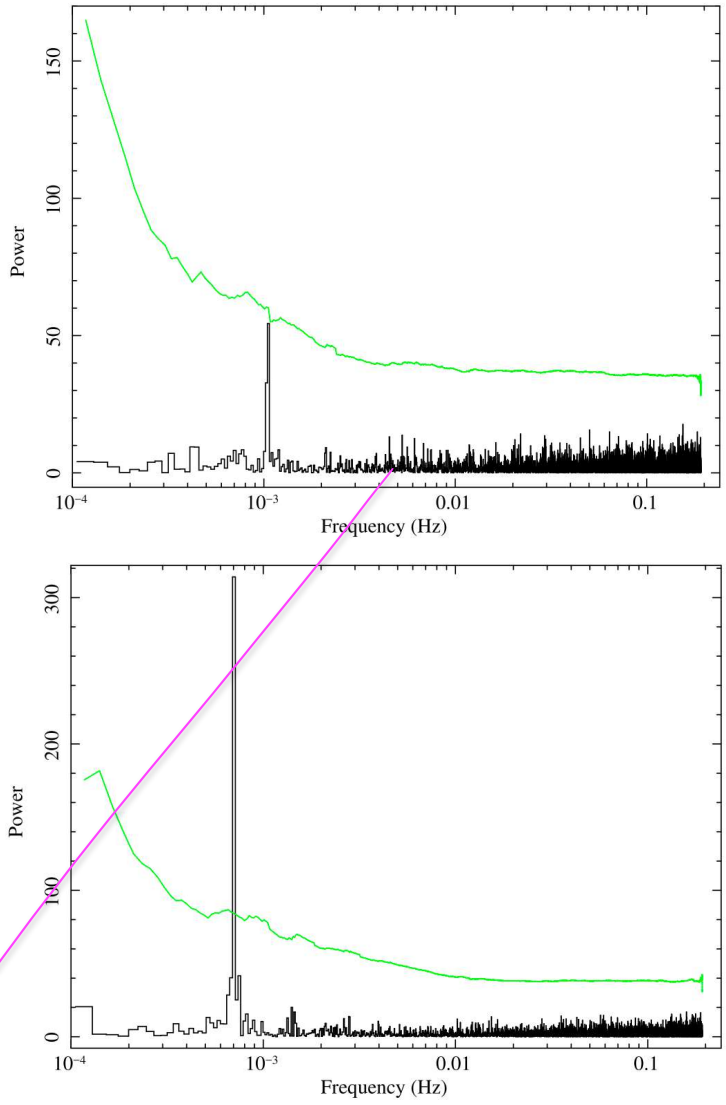

Figure 3.5. Top panel: PDS for 3XMM J051259.8-682640 during *XMM-Newton* observation 0690742601. Bottom panel: PDS for 3XMM J051034.6-670353 during *XMM-Newton* observation 0741800201. The green lines represent the 3.5σ detection thresholds. Plots taken from Haberl et al. (2017).

Finally, EXTraS search for coherent pulsations found two peculiar pulsators in

the direction of the Large Magellanic Cloud[5], that is 3XMM J051259.8–682640 and 3XMM J051034.6-670353 (Haberl et al., 2017). They show coherent pulsations at $P \simeq 956\,\mathrm{s}$ and $P \simeq 1417\,\mathrm{s}$, respectively (see PDSs in Fig. 3.5). 3XMM J051259.8–682640 had been previously identified as a BeXRB, but no pulsations had been detected yet. OGLE (Udalski et al., 2008, 2015) data of the known optical counterpart spanning 15 years show three dips occurring every $\simeq 1350\,\mathrm{d}$. If confirmed as the orbital period of the system, that would make 3XMM J051259.8–682640 the HMXB with the longest known orbital period. At the same time, the optical data strongly support the association of the system with the Large Magellanic Cloud.

3XMM J051034.6-670353 has a super-soft emission dominated by a black body component with $kT \simeq 70\,\mathrm{eV}$ and its spin signal has a pulsed fraction $PF \sim 100\%$, with minima lasting for one-third of the period. Given its similarities with systems like RX J1914.4+2456 (Cropper et al., 1998) and RX J0806.3+1527 (Israel et al., 2002; Esposito et al., 2014a), 3XMM J051034.6-670353 is probably a double-degenerate system, with two WDs orbiting each other (Kalomeni et al., 2016). In this case, the detected period would be associated with the orbital motion.

Although here I focused on the EXTraS search for coherent pulsations, the project has been particularly fruitful also in other research areas. For example, data mining projects like this are particularly useful for statistical studies sources and events. The search for transient events and aperiodic variability has allowed for the first time a characterization of the *XMM-Newton* sample of flares from Supergiant Fast X-ray Transients (SFXTs), a class of HMXBs in which the NS accretes from the wind of an early-type supergiant companion (Martínez-Núñez et al., 2017). The observed properties of the X-ray flares were found to be in agreement with the expectations from the onset of Rayleigh–Taylor instabilities in the accretion flow (Sidoli et al., 2019). A collection of other EXTraS results can be found in the review by De Luca et al. (2021).

3.3 Personal contribution to data mining projects

During these three years, I have been directly involved in the post-EXTraS search for coherent pulsations. Every year the pipeline is applied to the newly public *XMM-Newton* data and I have been visually inspecting the resulting PDSs since my PhD began, looking for new X-ray pulsators. In 2022, I found a periodic signal in the flux of a previously unidentified X-ray source, that is 4XMM J045626.3–694723. I will discuss the discovery of the pulsations and the possible nature of the source in Chap. 4. At the moment, we are also implementing additional software to search for periodic signals, based on machine learning and evolutionary algorithms (Pinciroli Vago et al., in prep.; see also Appendix A in Sacchi et al. 2024b). I am involved in the testing and verification of the results of the new algorithm.

I had a role also in the continuation of the CATS@BAR project, whose pipeline I routinely applied to the newly public *Chandra* data. I discovered a QPO in a source which seems consistent with the central AGN of a Seyfert 2 galaxy. If confirmed, it would represent the first of its kind to show QPOs. The work is still in progress and I will outline the main results in Chap. 5. I am also involved in the further

[5]See Chap. 4 for a more in-depth discussion on this satellite galaxy of the Milky Way.

characterization of the 41 original CATS@BAR pulsators. Among them, there is CXOGlb J002415.8–72043, a cataclysmic variable we recently identified as a polar (Amato et al. 2024; see also Appendix B). As described in Sect. B.2.2, I performed part of the timing analysis of the *Chandra* data of this source. More importantly, I performed the data reduction and timing analysis of the available *eROSITA* (Predehl et al., 2021) data, confirming the period of the periodic signal.

I am also currently involved in the development of a pipeline aimed at searching for variable X-ray sources in the *eROSITA* data. With nearly 930 000 entries, the catalogue of its first six months of observations is already the largest X-ray catalogue ever (eRASS1; see Merloni et al. 2024). I will briefly describe the pipeline, which is still at an early stage, in Appendix A, discussing the workflow and some parts of the code. This pipeline takes up the legacy of the data mining projects described in this chapter in the exploitation of the public archives of X-ray missions carrying imaging instruments.

Chapter 4

A new post-EXTraS pulsator

Oh, mamma mia, mamma mia, mamma mia, let me go
Beelzebub has a devil put aside for me, for me, for me!

Queen, *Bohemian Rhapsody*

4.1 Discovery of a magnetar candidate X-ray pulsar in the Large Magellanic Cloud Imbrogno et al. (2023)

During a systematic search for new X-ray pulsators in the *XMM-Newton* archive in 2022, I discovered a high amplitude ($PF \simeq 86\%$) periodic ($P \simeq 7.25\,\mathrm{s}$) modulation in the X-ray flux of 4XMM J045626.3–694723 (J0456 hereafter), a previously unclassified source in the Large Magellanic Cloud (LMC). The period of the modulation is strongly suggestive of a spinning NS. The source was detected only during one out of six observations in 2018-2022. Based on an absorbed power-law spectral model with photon slope of $\Gamma \simeq 1.9$, we derive a 0.3–10 keV luminosity of $L_{\mathrm{X}} \simeq 2.7 \times 10^{34}\,\mathrm{erg\,s^{-1}}$ for a distance of 50 kpc. The X-ray properties of J0456 are at variance with those of variable LMC X-ray pulsars hosted in high-mass X-ray binary systems with a Be-star companion. Based on *SALT* spectroscopic observations of the only optical object that matches the X-ray uncertainty region, we cannot completely rule out that J0456 is a NS accreting from a late-type (G8-K3) star, an as-yet-unobserved binary evolutionary outcome in the MCs. We show that the source properties are in better agreement with those of magnetars. J0456 may thus be the second known magnetar in the LMC after SGR 0526–66.

absorbed or unabsorbed?

4.1.1 Introduction

The Small and Large Magellanic Clouds (SMC and LMC, respectively) are the two best-studied star-forming satellite galaxies of the Milky Way. Thanks to their recent star formation bursts (in the inner regions) occurred ∼6–25 Myr ago in the LMC and ∼25–60 Myr ago in the SMC (Antoniou et al., 2010; Antoniou and Zezas, 2016), the MCs host a high number of X-ray pulsars, neutron stars (NSs) emitting

in the X-ray band and showing coherent pulsations originated by the NS rotation around its axis. In particular, the MCs host an unusually high number of HMXBs, systems in which the compact object, a NS or a black hole (BH), orbits an early (spectral type O/B) companion.

BeXRBs (HMXBs with a bright Be spectral-type companion; see Coe 2000; Okazaki and Negueruela 2001 for a review) represent the most numerous subclass of HMXBs in the MCs, with ∼150 BeXRBs out of ∼160 HMXBs. A total of ∼80 BeXRBs, in particular, host X-ray pulsars (Coe et al., 2015; Antoniou and Zezas, 2016; Haberl and Sturm, 2016; Haberl et al., 2022a). The recent discoveries of new HMXBs and pulsars in BeXRBs in the outskirts of the LMC suggest that more systems are likely hidden in these regions (Vasilopoulos et al., 2018; Maitra et al., 2021; Haberl et al., 2022a; Maitra et al., 2023). Only one LMXB (i.e. XRB whose companion has a mass $M \lesssim 1\,M_\odot$) hosting an accreting NS is known in the LMC, namely LMC X-2. The source is persistent and shows thermonuclear bursts, testifying to the presence of an old/low-magnetic field strength NS. No coherent or quasi-coherent periodic signals have been reported for LMC X-2 (see Agrawal and Nandi, 2020, and reference therein).

The SMC and the LMC are also known to host two magnetars, CXOU J010043.1–721134 (Lamb et al., 2002, 2003; McGarry et al., 2005; Tiengo et al., 2008; Chatterjee et al., 2021) and SGR 0526–66 (Mazets et al., 1979; Kulkarni et al., 2003; Tiengo et al., 2009; Park et al., 2020) respectively. Magnetars (Duncan and Thompson, 1992) are isolated NSs whose emission is (in the majority of the cases) in excess of their spin-down luminosities. Their emission is thought to be powered (for the most part) by the release of energy by the strong ($10^{14}\,\mathrm{G} \lesssim B \lesssim 10^{16}\,\mathrm{G}$) magnetic fields in their interior (for recent reviews, see Turolla et al., 2015; Kaspi and Beloborodov, 2017; Esposito et al., 2021). Currently, about 30 magnetars are known, all in our Galaxy with the exception of the two magnetars in the MCs. In this paper, we report on the discovery of X-ray pulsations at a period of about 7.25 s from a serendipitous source in the outskirts of the LMC, namely 4XMM J045626.3–694723 (J0456 henceforth). Although an unambiguous classification is still missing, the discovery of the 7.25-s periodicity that we report in this paper is strongly suggestive of a spinning NS. We discuss two competing scenarios capable of accounting for the source's observed properties: an accreting NS hosted in a very rare evolutionary outcome for an XRB or an isolated NS belonging to the magnetar class. In the latter case, J0456 would represent the third known magnetar in the MCs.

when was observed the first time?
was the first obs shorter?
did it detect the source but not the pulsation? If yes, was L comparable?

4.1.2 Observations and data reduction

X-ray observations

J0456 is located in an outer region of the LMC that has been observed twice by *XMM-Newton* (Jansen et al., 2001). The source was detected only during the second pointing (obs. 0841660501, duration $T \simeq 47$ ks) in October 2019. EPIC PN (Strüder et al., 2001) and EPIC MOS1 and MOS2 (Turner et al., 2001) data are available. The source was clearly detected in the three CCD cameras, which were operating in Full Frame mode (time resolution of 73.4 ms for EPIC PN, 2.7 s for EPIC MOS1 and 2.6 s for EPIC MOS2). I used SAS (Gabriel et al., 2004) v.20.0.0 and standard

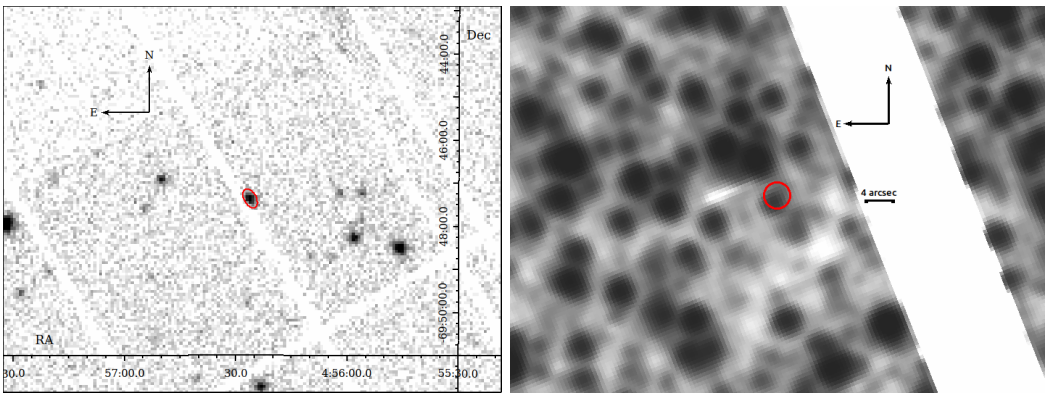

Figure 4.1. Close-up view of the *XMM-Newton* (left panel) and *SALT* (right panel) field of view, obtained during obs. 0841660501 and the night of the 24 November, 2022, respectively. Note the difference in scale between the two images. The *XMM-Newton* image shows both PN and MOSs data and the source region considered for the events extraction in red. The PN chip border is visible on the left of the source. The *SALT* image shows the J0456 position with the associated error at the 3σ level in red. The white gap on the right is due to the CCD border.

data reduction procedures to prepare the raw data for timing and spectral analysis. For the PN data, I considered only events with `PATTERN` ≤ 4, while for MOS data I selected events with `PATTERN` ≤ 12. Since J0456 was observed near the border of a PN chip gap, I selected events for both timing and spectral analyses in a 14×8 arcsec elliptical region aligned with the chip border and centred on the source position RA $= 4^{\rm h}56^{\rm m}26.^{\rm s}36$, Dec $= -69°47'23.''1$. The background was evaluated using a large source-free circular region on the same chip with a radius of 80 arcsec. The same regions were considered for the MOS cameras. The event arrival times were converted to the barycentre of the Solar System using the SAS task `barycen` and the source position. Response matrices and ancillary files were produced using the SAS tasks `rmfgen` and `arfgen`, respectively. For the X-ray timing and spectral analyses I considered events in the 0.3–10 keV band. Unless otherwise stated, the reported errors correspond to 1σ (68.3%) confidence ranges. A total of 776 events (source+background) were collected by the PN (426) and MOSs (350) cameras in the source extraction region, corresponding to a background-subtracted count rate of $(2.71 \pm 0.09) \times 10^{-3}$ count/s.

No pointings covering the source position are present in the *Chandra* (Weisskopf et al., 2000) and *NuSTAR* (Harrison et al., 2013) archives. 20 *Swift* (Burrows et al., 2005) pointings are found, though the XRT throughput and the relatively short exposures provided poor constraints (see Sect. 4.1.3 for more details). Two *RXTE* pointings were found and considered in the timing analysis (see Sect. 4.1.3).

Is it variable or simply exposures were too short to detect it?

Finally, *eROSITA* (Predehl et al., 2021) observed the field of J0456 during the all-sky surveys but the source was always too faint to be detected. Most of our analyses are based on the *XMM-Newton* observation 0841660501 during which the source was detected. The left panel in Fig. 4.1 shows a close-up view of J0456 field as observed by *XMM-Newton* during this observation, together with the extraction region of the source events (highlighted in red).

Optical observations

Following Kirsch et al. (2004) and Webb et al. (2020), we adopted a 2 arcsec uncertainty radius at 3σ confidence level for the positional accuracy. Within the *XMM-Newton* uncertainty region of J0456 we identified only one possible optical counterpart in the *Gaia* DR3 catalogue (Gaia Collaboration et al., 2016, 2023), with a magnitude G∼19.2 mag. We observed this source with the 11-m Southern African Large Telescope *SALT* (Buckley et al., 2006) during two consecutive nights, on November 24, 2022 and November 25, 2022. The right panel in Fig. 4.1 shows a close-up view of J0456 field as observed by *SALT* on November 24, 2022, together with the 3σ uncertainty region of J0456 (highlighted in red). The observations were divided in 5×1200 s exposures, for a total of 6000 s. During both nights the seeing was ∼ 2 arcsec with clear sky condition. We used the Robert Stobie Spectrograph RSS (Burgh et al., 2003; Kobulnicky et al., 2003) in long-slit spectroscopy mode for a spectral classification of the source. The PG0700 grating was used with a tilt angle of 4.6°, which resulted in a wavelength range of 3600 – 7400 Å. The primary reductions, which include overscan corrections, bias subtraction, gain and amplifier cross-talk corrections, were performed with the *SALT* science pipeline (Crawford et al., 2012). The remaining steps, including wavelength calibration, background subtraction and extraction of the one-dimensional spectra were performed with IRAF. The spectrophotometric standard star, LTT1788, was observed with the same grating settings as our target with an exposure time of 60 s. The reduction of the spectrum of LTT1788 was performed using the same procedure described above and a relative flux calibration was applied to our target spectrum.

which magnitude? was it constant?

both nights?

4.1.3 Results

Timing Analysis

Pulsations from J0456 were first detected within the framework of an extension of the EXTraS project[1] (De Luca et al., 2021, Rodríguez Castillo et al., in prep.), described in Chap. 3. I started from the EXTraS discovery parameters: a peak at a frequency $\nu \simeq 0.138$ Hz in the PN data with a confidence level of about 5.6σ. I followed Israel and Stella (1996) to infer the significance of the peak and the detection threshold in the PDS. As reported above, the vicinity of the source to the CCD gap motivated us to extract the events by using an elliptical region with the major axis aligned to the chip edge. The choice of an *ad hoc* region for the extraction was also motivated by the fact that, given the peculiar position of the source, the EXTraS automatic pipeline failed to determine the best circular extraction region.

In Fig. 4.2 we report the 0.3–10 keV PDS of the PN (top panel) and MOSs (bottom panel) data, together with the 3.5σ detection threshold. The peak is detected in the time series of the three EPIC instruments and not in the event lists of the other sources detected in the field of view. Moreover, no significant peaks are detected in the background regions extracted in different parts of the CCDs. Correspondingly, we can exclude that the detected signal is spurious or due to noise fluctuations. Within the combined PN+MOSs PDS the peak has a significance of

[1]The details of the periodic signal-search pipeline can be found in Sect. 4 of De Luca et al. (2021) and in Sect. 3.2.1 of this thesis.

11.3σ (computed over the whole $2 \times 10^{-5} - 0.185$ Hz PDS). The PDS shows no sign of red-noise variability, with a 3σ upper limit on the rms fractional variation of 0.36 from 10 µHz up to 10 mHz.

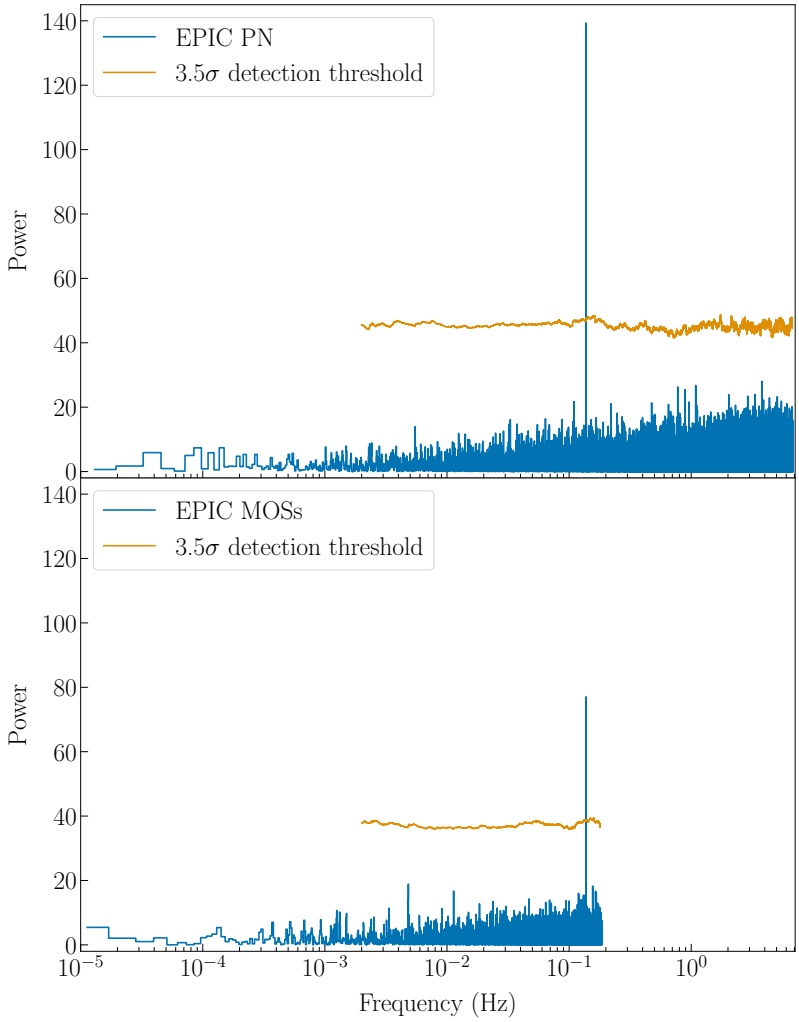

Figure 4.2. PDS (blue) of J0456 light curve in the 0.3–10 keV band obtained from EPIC PN (top panel) and MOSs (bottom panel) data of observation 0841660501, together with the local 3.5σ detection threshold (orange). The peak at frequency $\nu \simeq 0.138$ Hz has a significance of 11.3σ over the whole PN+MOSs PDS.

I refined the period estimate through epoch folding (Leahy et al., 1983) and phase-fitting techniques and obtained a value of the period of $P_{\rm spin} = 7.25243 \pm 0.00004$ s. I derived a 3σ upper limit on its first derivative $|\dot{P}_{\rm spin}| < 2.1 \times 10^{-8}\,{\rm s\,s^{-1}}$. The 0.3–10 keV background-subtracted folded profile is shown in Fig. 4.3 (bottom curve with filled circle markers) and has a pulsed fraction (defined as the semi-amplitude of the sinusoid divided by the source average count rate) of $PF = (86 \pm 6)\%$. No higher harmonics are needed to fit the profile well. I also considered two sub-bands, 0.3–2 keV and 2–10 keV (chosen so that about half of the events fall in each energy interval), to investigate the dependence of the signal shape as a function of energy.

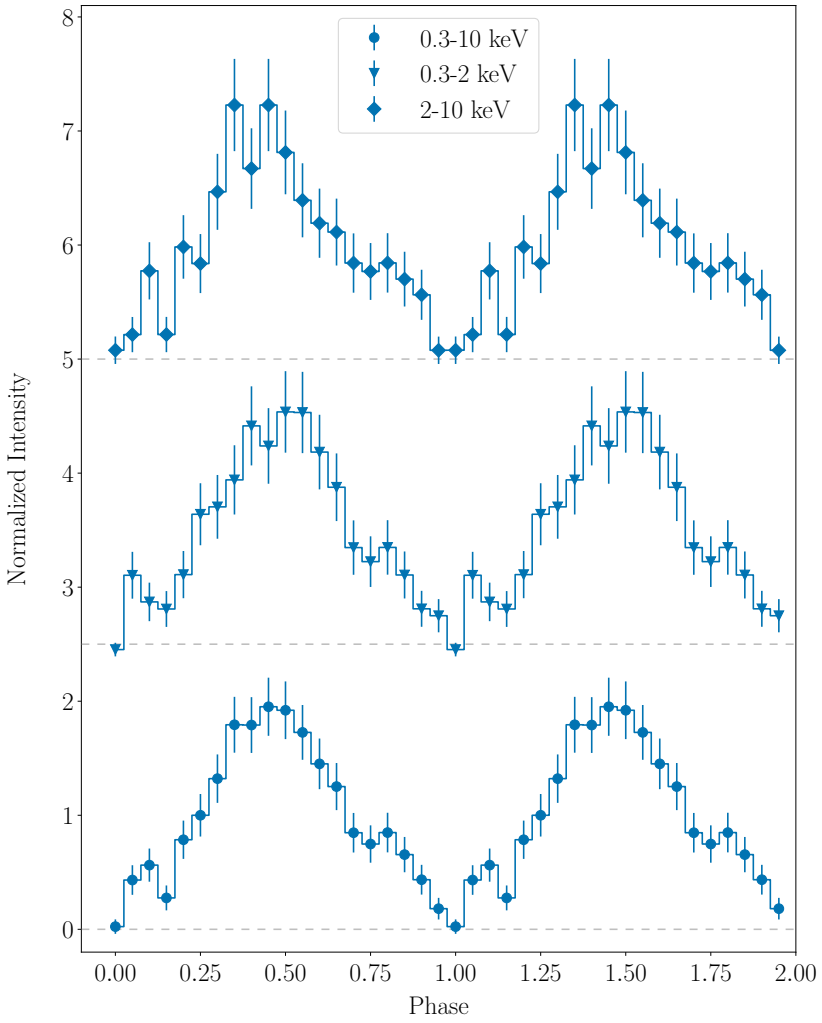

Figure 4.3. Phase-folded profile of the PN+MOSs background-subtracted light curves in the 0.3–10 keV (circles), 0.3–2 keV (triangles) and 2–10 keV (diamonds) bands. For display purposes, the 0.3–2 keV and 2–10 keV light curves are vertically shifted with an offset equal to 2.5 and 5, respectively. The grey dashed lines show the zero-flux level for each energy band.

In Fig. 4.3 we also report the folded profile in the soft (triangle markers, central curve) and hard (diamond markers, top curve) bands, where the pulsed fractions are $PF_{\rm soft} > 88\%$ (1σ lower limit) and $PF_{\rm hard} = (85 \pm 10)\%$, respectively. Even in these two cases, the inclusion of higher harmonics in the model did not significantly improve the fit. The hard and soft pulsed fractions are consistent, within 3σ, with each other and with the same, 100% pulsed fraction. Note that all pulse minima are consistent with having zero counts.

For our timing analysis I also considered two RXTE pointings (ObsID 40087-04-01-00 and 96441-01-01-00) during which the J0456 position was covered. I searched for signals around the *XMM-Newton* detected period (I adopted a maximum $|\dot{P}_{\rm spin}| < 10^{-10}\,{\rm s\,s^{-1}}$) in the Proportional Counter Array (PCA, Jahoda et al., 2006) data, without success. No reliable upper limit on the pulsed fraction could be inferred, being the PCA a non-imaging instrument, in which the background contribution to the count rate could not be reliably quantified.

Spectral Analysis

I performed the spectral analysis of J0456 with the XSPEC package (Arnaud, 1996) v.12.12.0g, which is included in the HEASOFT[2] distribution (v.6.29c). I grouped by three the single bins (to cope with the original spectral resolution) and grouped the data so as to have at least 15 counts in a single spectral bin (to enable a reliable usage of the χ^2 statistics). Different rebinning factors (e.g., 20 counts per bin at least) did not significantly alter the estimated values of the parameters, but we chose a 15-count configuration because it provided a lower uncertainty on the absorption column to the source. The abundances and cross sections were set to those of Wilms et al. (2000) and Verner et al. (1996), respectively. In this section, the uncertainties indicate a 90% confidence range.

I first considered a simple absorbed power-law (PL) model, with two absorption components to account for both the Galactic and the inter-galactic plus LMC absorption: in XSPEC syntax, this model corresponds to `tbabs*tbvarabs*powerlaw`. I set the first absorption component (`tbabs`) to the Galactic value[3] $N_{\rm H,gal} = 8.91 \times 10^{20}\,{\rm cm^{-2}}$ in the direction of the LMC (Dickey and Lockman, 1990). Following Haberl et al. (2022a, 2023b) I set the elemental abundances of the LMC `tbvarabs` component at 0.49 times that of the Solar abundance, and allowed the column density to vary. The PL model provides an excellent description of the spectrum ($\chi^2_r \sim 1$). The associated best-fit parameters are reported in Table 4.1.

How many dof?

I also considered a model with an additional black body (BB) component, since an absorbed BB+PL is often used to fit the spectra of both magnetars and accreting X-ray sources. The addition of a BB component to the PL model did not significantly improve the fit, resulting in a by-chance probability (computed by means of the F-test) of $\simeq 1\%$, which led us to discard the model. I also considered an absorbed BB+BB model, since it is often used to fit the magnetars' spectra (see, e.g., Israel et al., 2016a). Our BB+BB model also provides a good description of the observed spectra, with $\chi^2_r \sim 0.89$, and the values for the temperatures $kT_{\rm BB}$ ($\simeq$0.3 and 0.9 keV,

[2] https://heasarc.gsfc.nasa.gov/docs/software/lheasoft/.

[3] Computed by means of NASA's HEASARC $N_{\rm H}$ web calculator https://heasarc.gsfc.nasa.gov/cgi-bin/Tools/w3nh/w3nh.pl.

respectively) and radii $R_{\rm BB}$ ($\simeq$2 and 0.4 km, respectively) of both BBs are consistent with the ones expected from hotspots on a NS. However, we favoured the PL model given its greater simplicity, since it involves one emission component instead of two while still providing a good description of the spectrum. Both the best-fit parameters of the BB+PL and BB+BB model can be found in Table 4.1. I also tested a single component BB model, but the fit is significantly worse, as shown by a large $\chi^2_r \sim$1.5.

The PN and MOSs spectra, together with the best-fit PL model, are shown in Fig. 4.4. The intrinsic $N_{\rm H} \simeq 4.8 \times 10^{21}\,{\rm cm}^{-2}$ we derived by adopting the PL spectral model is consistent with the source being of extragalactic origin and the only known system along the line of sight is the LMC. Assuming a distance of 50 kpc for the LMC (Pietrzyński et al., 2013) and correcting for the total absorption, I derive an unabsorbed luminosity of about $L_{\rm X} \simeq 2.7 \times 10^{34}\,{\rm erg\,s}^{-1}$ in the 0.3–10 keV band.

For those observations in which J0456 was not detected I computed the 3σ upper limit on its count rate by means of the `sosta` tool in XIMAGE[4]. Exploiting the best-fit parameters reported in Table 4.1 for the PL model, I converted the 3σ upper limits on the count rate in 3σ upper limits on the unabsorbed flux of J0456 in the 0.3–10 keV band[5]. Most *Swift* pointings lasted less than 300 s, too short to derive meaningful upper limits. From the longest observation (obs. 00033492002, $T \simeq 630$ s, October 2014) I derived a 3σ upper limit on the unabsorbed flux $F_{\rm X} = 9.2 \times 10^{-13}\,{\rm erg\,cm}^{-2}\,{\rm s}^{-1}$. The two most stringent upper limits come from the first *XMM-Newton* pointing (obs. 0823790301, May 2018) and *eROSITA* (May and November 2021, May and November 2022). We derived a 3σ upper limit on the count rate in the EPIC MOS cameras of 9×10^{-4} counts/s, corresponding to a 3σ upper limit on the unabsorbed flux $F_{\rm X} = 1.5 \times 10^{-14}\,{\rm erg\,cm}^{-2}\,{\rm s}^{-1}$. In the latter, considering the first four *eROSITA* all-sky surveys (eRASS1-4), the derived 3σ upper limit for the unabsorbed flux is $F_{\rm X} = 3.8 \times 10^{-14}\,{\rm erg\,cm}^{-2}\,{\rm s}^{-1}$ for each survey (F. Haberl, private communication).

you provide here a flux, but before you gave an unabsorbed luminosity. To ease the comparison you should provide a flux, too

This indicates that the source is variable! Is it possible to have a flux variation by a factor of >6 in a TBD time, before the first and second XMM obs for a magnetar?

Optical Analysis

High-quality spectra were obtained in the 3800–5850 Å range for the optical object consistent with the X-ray position and are shown in Fig. 4.5. The red end of the spectrum (wavelength $\lambda > 5850$ Å) was dominated by diffuse emission of the surroundings during both nights. Therefore, we did not consider this range for our analysis. We derived a relative magnitude of $V \sim 18.9$ mag.

No emission lines usually associated with X-ray reprocessing by the companion and/or an accretion disc, such as the Balmer lines and He II (4686 Å), are found in the spectra. We first checked that the wavelengths of the few absorption lines present in the spectra are shifted by an amount equivalent to a radial velocity of $v_r \sim 250$ km/s ($\Delta\lambda \sim 3.2 - 4.9$ Å in the 3800–5850 Å range), which is consistent with the star being in the LMC (Piatti et al., 2018). Therefore, we associate this star with the LMC. Assuming a distance modulus $\mu \sim 18.5$ mag for the LMC (Subramanian and Subramaniam, 2013) and an extinction coefficient[6] $A_V \sim 0.2$ mag (Schlafly and

[4] https://heasarc.gsfc.nasa.gov/xanadu/ximage/.

[5] All the upper limits have been computed using the WebPIMMS tool: https://heasarc.gsfc.nasa.gov/cgi-bin/Tools/w3pimms/w3pimms.pl.

[6] Computed with the NASA/IPAC Extragalactic Database (NED) Extinction Calculator available online at https://ned.ipac.caltech.edu/extinction_calculator.

Ideally, as far as I know, the MOS is calibrated down to 0.3 keV
the pn should be down to 0.2 keV (or 0.3 keV depending on who you are talking with)

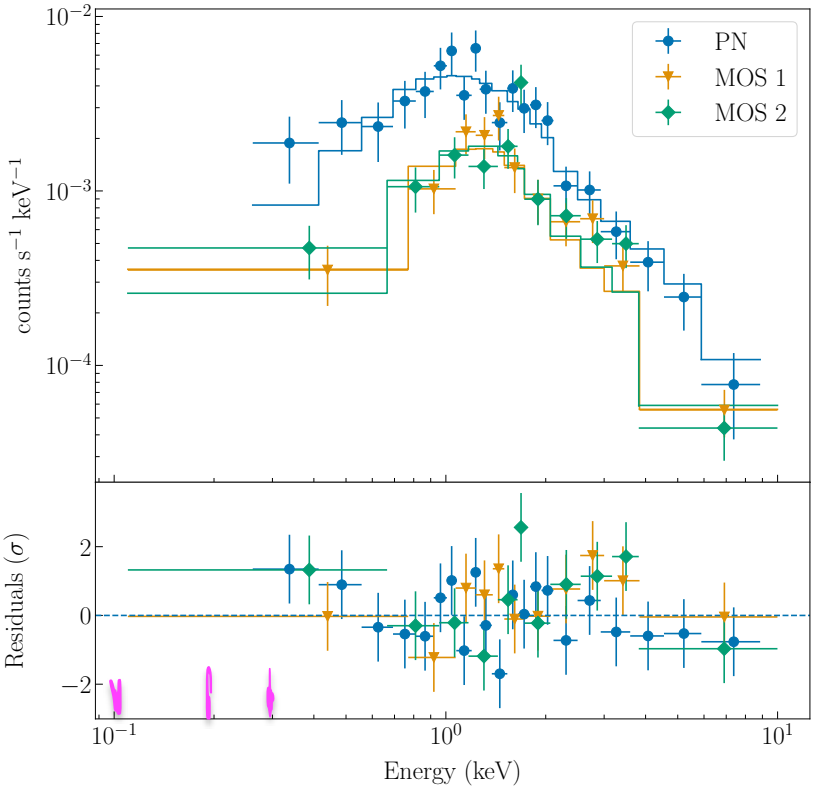

Figure 4.4. Top: EPIC spectrum of J0456 from observation 0841660501 (blue circles: PN data; yellow triangles: MOS 1 data; green diamonds: MOS 2 data), together with the best-fit absorbed power-law model (same colour scheme). Bottom: fit residuals in units of standard deviation (same color and marker scheme as above).

Table 4.1. Best-fit parameters of the models considered for the phase-averaged spectrum of J0456. PL: power-law component. BB: black body component. Γ: power-law photon index. The reported errors show the 90% confidence region. When only one black body component was adopted in the model we reported the temperature $kT_{\rm BB}$ and the radius $R_{\rm BB}$ under the cold ones column ($kT_{\rm BB}^{\rm cold}$ and $R_{\rm BB}^{\rm cold}$).

Parameter	PL	BB + BB	PL + BB
$N_{\rm H}^{a}$ ($10^{21}\,{\rm cm}^{-2}$)	$4.8^{+2.5}_{-2.0}$	$< 1.2^{d}$	$< 2.9^{d}$
Γ	$1.93^{+0.23}_{-0.21}$	–	$1.4^{+1.2}_{-0.5}$
$kT_{\rm BB}^{\rm cold}$ (keV)	–	$0.30^{+0.10}_{-0.09}$	$0.63^{+0.26}_{-0.12}$
$R_{\rm BB}^{\rm cold}$ (km)	–	$1.9^{+3.2}_{-1.5}$	$0.63^{+0.53}_{-0.56}$
$kT_{\rm BB}^{\rm hot}$ (keV)	–	$0.86^{+0.18}_{-0.14}$	–
$R_{\rm BB}^{\rm hot}$ (km)	–	$0.43^{+0.28}_{-0.40}$	–
$F_{\rm X}^{b}$ ($10^{-14}\,{\rm erg\,cm^{-2}\,s^{-1}}$)	$6.10^{+0.73}_{-0.71}$	$5.27^{+0.55}_{-0.66}$	$5.87^{+0.84}_{-0.82}$
$L_{\rm X}^{c}$ ($10^{34}\,{\rm erg\,s^{-1}}$)	$2.73^{+0.45}_{-0.33}$	$1.58^{+0.17}_{-0.20}$	$1.9^{+1.0}_{-0.2}$
χ^2/dof	40.03/40	33.68/38	31.80/38

Notes.
[a] The Galactic absorption component was fixed to $N_{\rm H,gal} = 8.91 \times 10^{20}\,{\rm cm}^{-2}$ (Dickey and Lockman, 1990).
[b] Absorbed flux in the 0.3–10 keV band.
[c] Unabsorbed luminosity in the 0.3–10 keV band, assuming a distance of 50 kpc.
[d] 90% confidence level upper limit.

Finkbeiner, 2011), the absolute magnitude in V-band for this star is $M_V \sim 0.2$ mag. This excludes any O or B spectral type star. The optical spectra, in particular, show the Ca II K line at 3933 Å and the Ca II H + Hϵ blend at 3969 Å, together with the CH G-band at 4300 Å, the Fe I at 4383 Å and the Mg I triplet at 5167, 5172 and 5183 Å (all the absorption lines are reported to their restframe wavelengths). For our classification, we considered spectral features that were visible in both observations. For instance, the lines at 4100–4150Å, which appeared in emission during the first night (blue spectrum) and in absorption during the second night (yellow spectrum), were excluded as they probably arose from incorrect background subtraction. We can exclude that the source is a late-F star by the absence of lines such as Hγ (4340 Å), H8 (3889 Å) and H9 (3835 Å). The spectral shape, absolute magnitude M_V and identified lines are all consistent with the source being a late-type G (G8) or early-type K (K0–3) star of luminosity class III.

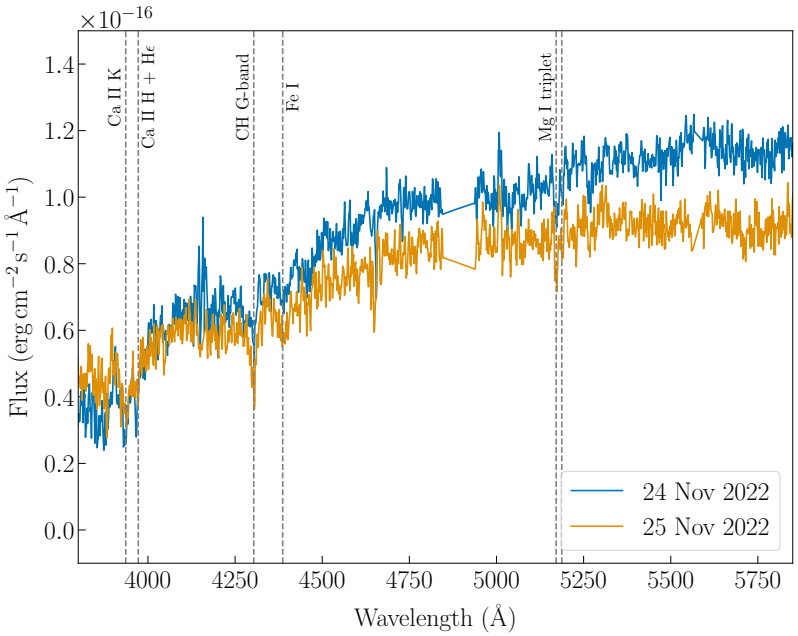

Figure 4.5. Optical spectra in the 3800–5850 Å band of the candidate optical counterpart of J0456 during the first (blue) and second (yellow) night of observations. The features in the spectra we used for our classification are marked by the gray dashed lines.

4.1.4 Discussion

The 7.25-s coherent period of the pulsations strongly suggests that J0456 is a spinning NS. However, the data currently available for J0456 are not sufficient for an unambiguous classification. In fact, without a further measurement of the spin period $P_{\rm spin}$ it is not possible to derive its secular first derivative $\dot{P}_{\rm spin}$ and therefore to determine whether the pulsar is isolated (spin-down) or in an accreting binary system (spin-up). Therefore, we attempted a classification of the source based on the available information from the observations we analysed in the previous section and the MCs environment. J0456 may be identified as either (i) an accreting X-ray

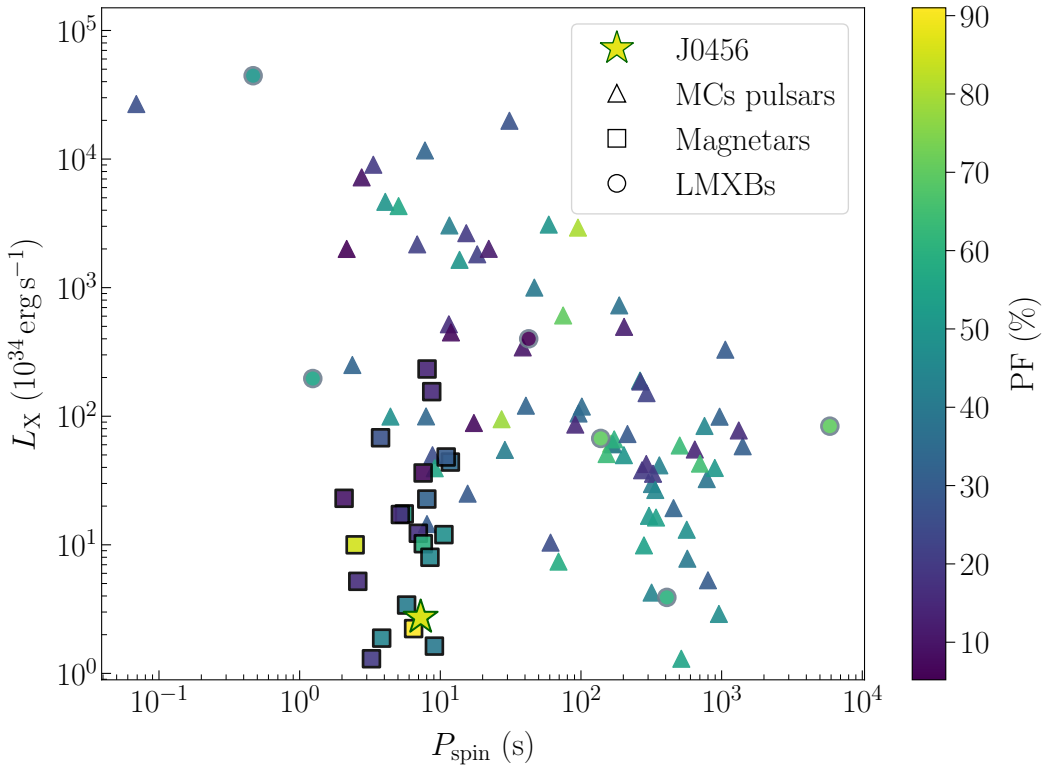

Figure 4.6. Luminosity in the 0.3–10 keV band in units of 10^{34} erg s^{-1} as a function of the spin period P_{spin}. In this plot, we show J0456 (star marker), the magnetars (square markers) included in the MOOC catalogue (Coti Zelati et al., 2018), the BeXRBs (triangle markers) in the Magellanic Clouds (Coe et al., 2015; Antoniou and Zezas, 2016; Bartlett et al., 2017; Boon et al., 2017; Haberl et al., 2017; Kennea et al., 2017; Vasilopoulos et al., 2017; Koliopanos and Vasilopoulos, 2018; La Palombara et al., 2018a,b; Maitra et al., 2018, 2021; Carpano et al., 2022; Haberl et al., 2022a,b; Maitra et al., 2023; Haberl et al., 2023a, and references therein) and the pulsars in LMXBs (circle markers) Her X-1, GRO J1744-28, IGR J16358-4726, 3XMM J181923.7-170616 and Swift J1843.5-0343. For these sources, we refer to the LMXBs XRBCat (Avakyan et al., 2023) and references therein. The color of each marker shows the pulsed fraction of the spin signal of the corresponding source, as indicated by the colour bar in the middle. To compute the luminosities, we assumed a distance of 50 kpc (Pietrzyński et al., 2013) and 62 kpc (Graczyk et al., 2014) for the LMC and the SMC, respectively.

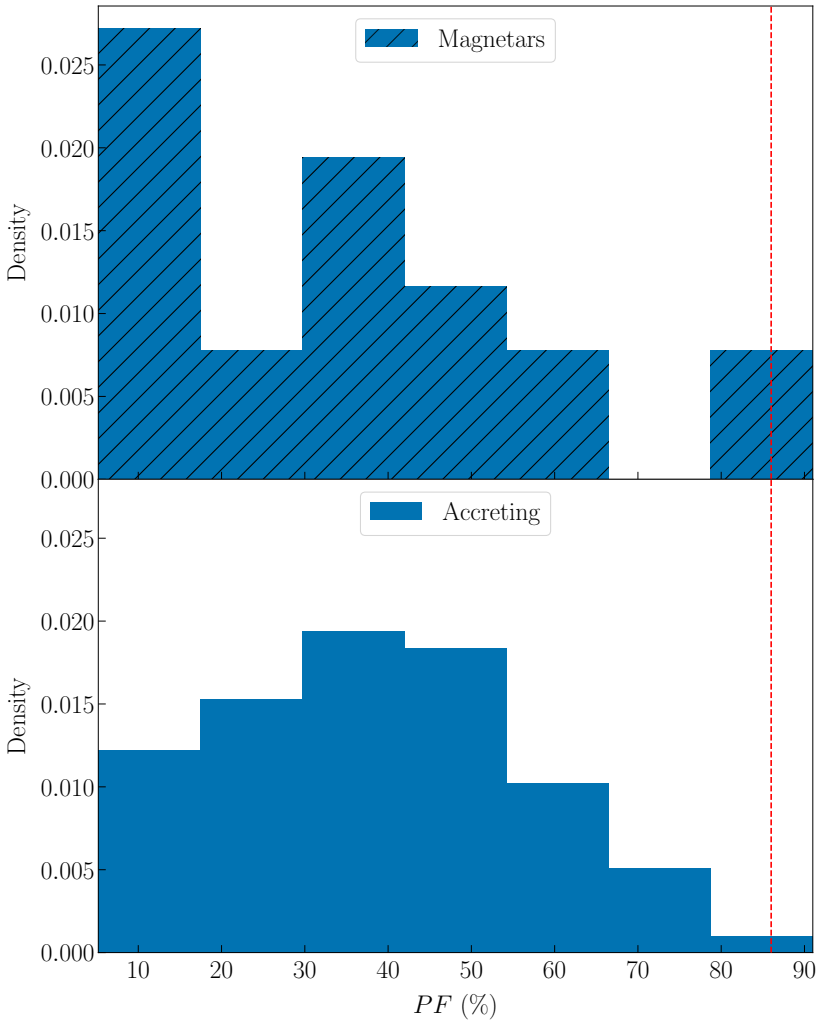

Figure 4.7. Top panel: distribution of the pulsed fraction of the magnetars reported in the MOOC catalogue (Coti Zelati et al., 2018) at the peak of the outburst. Bottom panel: distribution of the pulsed fraction of the same accreting X-ray sources considered for Fig. 4.6. In both panels, the red dashed line marks the pulsed fraction of the signal found in J0456 flux.

pulsar with a G8-K3 III companion or (ii) an isolated NS of the magnetar class.

Concerning the first scenario, we note that we do not have any information on the X-ray activity state of the source at (or around) the time of the optical observations of J0456. Therefore, the absence of the optical emission lines, characteristic of X-ray reprocessing, does not rule out the accreting scenario, as J0456 could be a transient binary system in quiescence at the time of the *SALT* observations.

Given that no LMXB X-ray pulsars are known in the MCs, we started considering the properties of the known X-ray pulsars in the MCs, i.e. those in HMXBs, under the hypothesis that they are coeval with J0456. Christodoulou et al. (2016) presented an analysis on all accreting X-ray pulsars with $P_{\rm spin} < 10^3$ s in both the LMC and the SMC. By looking at the relation between the minimum X-ray luminosity $L_{\rm X}$ shown by these sources and their spin periods $P_{\rm spin}$ and following Stella et al. (1986), they were able to derive a typical lower limit on the magnetic field $B > 3 \times 10^{11}$ G for NSs with $P_{\rm spin} < 15$ s. Assuming that J0456 is an accreting NS we can use the standard expression to derive the corotation radius $R_{\rm co}$

$$R_{\rm co} = \left(\frac{GM_{\rm NS}}{\Omega^2}\right)^{1/3} \simeq 1.5 \times 10^8 \left(\frac{M_{\rm NS}}{M_\odot}\right)^{1/3} P^{2/3}\,{\rm cm} \tag{4.1}$$

and the magnetospheric radius $R_{\rm m}$

$$R_{\rm m} = 3.3 \times 10^7 \xi_{0.5} B_{12}^{4/7} L_{39}^{-2/7} R_6^{10/7} M_{1.4}^{1/7}\,{\rm cm}, \tag{4.2}$$

where the X-ray luminosity L, the magnetic field B, the radius R of the NS and its mass M are in $10^{39}\,{\rm erg\,s^{-1}}$, 10^{12} G, 10^6 cm and $1.4\,{\rm M_\odot}$ units, respectively. In our case $P \simeq 7.25$ s, $L_{\rm X} \simeq 2.7 \times 10^{34}\,{\rm erg\,s^{-1}}$. Assuming a standard value for $M_{\rm NS} \simeq 1.4\,{\rm M_\odot}$, we derived $R_{\rm co} \simeq 6.3 \times 10^8$ cm. In order to have accretion onto the NS $R_{\rm m} < R_{\rm co}$. Assuming $\xi = 0.5$, we find that the magnetic field of J0456 should be $B < 9.1 \times 10^{11}$ G. Moreover, assuming that the non-detection of the pulsar at a luminosity level a factor of about 4 lower ($L_{\rm X} \simeq 6.7 \times 10^{33}\,{\rm erg\,s^{-1}}$) is related to the onset of the propeller phase, it converts to a magnetic field lower limit of $B > 4.5 \times 10^{11}$ G. Both limiting values are consistent with those obtained by Christodoulou et al. (2016), suggesting that the assumed coeval hypothesis is likely reliable.

Only two LMXBs are known in the MCs. eRASSt J040515.6-745202 (Haberl et al., 2023b) showed a Type-I X-ray burst, indicative of low ($B \lesssim 10^8$ G) magnetic fields, and is not pulsating. LMC X-2, likewise non-pulsating, shows a blue optical spectrum and it is a persistent source (see Lavagetto et al., 2008; Agrawal and Misra, 2009; Agrawal and Nandi, 2020, and references therein). Few Galactic LMXBs, such as Her X-1, GRO J1744-28, IGR J16358-4726, 3XMM J181923.7-170616 and Swift J1843.5-0343, host X-ray pulsars with similarly high ($B \gtrsim 10^{11}$ G) magnetic fields, though they represent an exception among LMXBs. In fact, the greatest part of known pulsars in LMXBs are usually old NSs spun up to ms-long spin periods by accretion and, therefore, possess low magnetic fields $B \lesssim 10^8$ G (Bahramian and Degenaar, 2023), inconsistent with our findings. Furthermore, the latter class of LMXBs very often shows aperiodic variability in the form of non-Poissonian power spectrum noise components (likely originated by the accretion process itself). The latter is simply not detected in the *XMM-Newton* dataset (see the PDS shown in Fig. 4.2). Note that, following the recently released LMXB Cat[7] (Avakyan et al.,

4U 1626-67?

[7] http://astro.uni-tuebingen.de/~xrbcat/ and references therein.

2023), for our discussion we included the symbiotic X-ray binaries (SyXBs, XRBs composed of an accreting NS and a late-type K1-M8 companion; see Tab. 1 in Yungelson et al. 2019 for a list of confirmed and candidates SyXBs) among the LMXBs. Summarizing, within the accreting X-ray pulsar scenario, J0456 might be a new member of the rare class of relatively young pulsars in LMXBs/SyXBs, the first ever in the MCs, with very peculiar properties.

The XRB scenario is also challenged by a previous work of Antoniou and Zezas (2016). Starting from the LMC star formation history reconstructed by Harris and Zaritsky (2009) and the data coming from the Magellanic Clouds Photometric Survey (MCPS, Zaritsky et al., 2004), they estimated the chance coincidence probability for an optical source to be found in the uncertainty region of an X-ray source in the LMC as a function of both the absolute magnitude M_V and the reddening-corrected colour index $B-V$. As one can see from Fig. 2 in the original paper, for a source with $M_V \sim 0.2$ mag like ours this probability is always $\gtrsim 62\%$ within a 5 arcsec region. Their results are probably (at least partially) driven by the fact that they included the central region of the LMC, where more massive (O/B-type) stars are expected. Even considering this effect and the fact that they considered a bigger uncertainty region than us, we expect this probability to be only a factor of a few higher than the chance coincidence probability for J0456, especially considering how crowded the *SALT* field is (as can be seen in Fig. 4.1).

It is worth noticing that a period of 7.25-s might be still compatible with the spin period of an accreting white dwarf (WD). For example, the fastest-spinning accreting WDs, i.e. AE Aqr, LAMOST J024048.51+195226.9 (though X-ray quiet) and HD 49798[8], show a spin period of about 33 (Li et al., 2016), 25 (Pelisoli et al., 2022) and 13 s (Israel et al., 1997), respectively. Correspondingly, in the accreting WD scenario J0456 might be associated to an intermediate polar (IP) system similar to those above cited. If so, J0456 would be simultaneously the fastest and brightest (typical luminosities[9] are $L_X \lesssim 10^{32} - 10^{33}\,\mathrm{erg\,s^{-1}}$) accreting WD of the whole IP class, the first ever in the MCs. The lack of orbital modulation in the spin signal phase is also an indication that, if J0456 were an accreting source, the orbital period should be at least 3–4 times the duration of the observation ($T \simeq 47$ ks). This corresponds to $P_{\rm orb} \gtrsim 40$ h, the second longest orbital period for an IP after GK Per (with an orbital period of ∼2 d, Álvarez-Hernández et al., 2021), if not longer. Finally, IPs often show strong optical emission lines both during quiescence and active phases (Saito et al., 2010). Our *SALT* spectra, on the other hand, do not show similar features. In light of these factors, we consider this scenario rather unlikely. We also took into account the possibility of an isolated (non-accreting) WD like AR Sco (Takata et al., 2018). However, J0456 is 4 orders of magnitude brighter than AR Sco and the alternation of active-quiescent phases is not expected in isolated sources. Therefore, we consider this scenario unlikely too.

If J0456 is not associated with the G8-K3 III star, it might be related to the other class of variable NSs observed in the MCs, e.g. magnetars. In order to further explore this scenario we compared the source X-ray luminosity L_X in the 0.3–10 keV

[8] Although the nature of HD 49798 is still debated, a recent work by Mereghetti et al. (2021) supports an accreting WD scenario.

[9] See the IP catalogue https://asd.gsfc.nasa.gov/Koji.Mukai/iphome/catalog/alpha.html and references therein.

band and the spin period $P_{\rm spin}$ with the ones shown by all the magnetars included in the Magnetar Outburst Online Catalogue[10] (Coti Zelati et al., 2018). We also compared them with the same quantities shown by the BeXRBs in the SMC and the LMC for which both $L_{\rm X}$ and $P_{\rm spin}$ measurements were available during active phases. We considered the BeXRBs reported by Coe et al. (2015) for the SMC and Antoniou and Zezas (2016) for the LMC. We then cross-checked our sample in the Bologna INAF/IAPS catalogue of accreting X-ray binaries[11] to check for missing pulsars not included in the aforementioned catalogues/publications. To convert the flux in luminosity we considered a distance of 50 kpc (Pietrzyński et al., 2013) and 62 kpc (Graczyk et al., 2014) for the LMC and SMC, respectively. We also included the same quantities for the few Galactic high-B X-ray pulsars found in LMXBs. Since J0456 has been detected only once, we probably observed the source during a period of high activity. In order to compare these sources with J0456, we considered their $L_{\rm X}$ and $P_{\rm spin}$ values as inferred during their outburst peak (in the case of magnetars) or during their high luminosity phases (in the case of BeXRBs and LMXBs). We considered the persistent luminosity values for those magnetars for which we do not have detection of an outburst: 1E 1841-045 (Vasisht and Gotthelf, 1997), SGR 1900+14 (Mereghetti et al., 2006), 4U 0142+614 (Rea et al., 2007b), 1RXS J170849.0-490910 (Rea et al., 2007a), CXOU J010043.1-721134 (McGarry et al., 2005), CXOU J171405.7-381031 (Gotthelf et al., 2019) and SGR 0526-66 (Mazets et al., 1979). Finally, for the LMXBs (often showing large flux ranges) we assumed average values of the fluxes, while we assumed the mean distance reported by the LMXB Cat to convert the flux in luminosity.

The results of our analysis are shown in Fig. 4.6, where we plot the X-ray luminosity $L_{\rm X}$ of magnetars (square markers), BeXRBs in MCs (triangle markers) and Galactic high-B LMXBs (circle markers) as a function of the spin period $P_{\rm spin}$, whereas the PF is represented by the filled-in color of the marker itself. J0456 (marked with a filled star) is a peculiar case where both a short $P_{\rm spin}$ and low $L_{\rm X}$ are observed, a combination typically associated with magnetars only. Indeed, the magnetars in our sample are found to have a luminosity $L_{\rm X} \simeq 10^{34} - 10^{36}\,{\rm erg\,s^{-1}}$. Accreting X-ray pulsars at similar ($\sim$7 s) periods, instead, show a luminosity which is at least one order of magnitude higher ($\sim 10^{35}\,{\rm erg\,s^{-1}}$), with the least luminous XRBs at these periods in the MCs being LXP 8.04 at $L_{\rm X} \simeq 1.5 \times 10^{35}\,{\rm erg\,s^{-1}}$ (Vasilopoulos et al., 2014) and SXP 7.92 at $L_{\rm X} \simeq 1 \times 10^{36}\,{\rm erg\,s^{-1}}$ (Bartlett et al., 2017).

A second indication of the magnetar nature of J0456 comes from spectral analysis. As already explained in Sect. 4.1.3, a simple power-law (PL) model was enough to obtain a good fit of the energy spectrum. Although both accreting X-ray pulsars and magnetars can exhibit a power-law component in their spectra, a photon index $\Gamma \simeq 1.9$ is particularly high for an accreting system. A photon index $\Gamma \sim 2$, instead, is in line (although not particularly high) with the values usually found for transient magnetars (Esposito et al., 2021). It is also interesting to note that in the

[10] An online and updated version of this catalogue can be found in the Magnetar Outburst Online Catalogue (MOOC): http://magnetars.ice.csic.es/#/welcome. A catalogue of known magnetars has been compiled also by Olausen and Kaspi (2014) and an updated version can be found at http://www.physics.mcgill.ca/~pulsar/magnetar/main.html.

[11] http://www.iasfbo.inaf.it/~mauro/pulsar_list.html and references therein.

BB+BB model, often employed to describe magnetars' emission in outburst, the radii and temperatures associated with the BBs would be $R \simeq 2$ km and 0.4 km and $kT_{\rm BB} \simeq 0.3$ keV and 0.9 keV, respectively. Both values are compatible with those found for other magnetars (see Esposito et al., 2021, and references therein). In this magnetar scenario, the dipolar magnetic field is expected to be of the order of 10^{14} G.

We further note that high-amplitude pulsed fractions are more common in magnetars than in accreting pulsars. Fig. 4.7 shows the distribution of PFs for the magnetars (blue barred histogram in the top panel) and BeXRBs+LMXBs (blue histogram in the bottom panel) in our sample compared to the PF inferred for J0456 (red dashed line). For the PF we considered the value shown during an outburst/high-active phase as for $L_{\rm X}$ and $P_{\rm spin}$. At $PF > 80\%$ (the range of interest for J0456) the probability of finding an XRB with properties similar to those of J0456 is rather low, while it is not negligible for magnetars. Indeed, 2 out of the 21 magnetars in our sample show a pulsed fraction $PF > 80\%$, while only one XRB, SXP 95.2 (Laycock et al., 2002), out of 80 shows such a high pulsed fraction. We also note that J0456 pulse profiles in Fig. 4.3 show a minimum consistent with a null flux, which is hard to explain in the framework of an accreting X-ray source, where low amplitude modulations are expected due to the presence of the accretion disc. There are no X-ray pulsars in the MCs with average pulse minima consistent with a zero flux level. In the case of isolated NSs, on the other hand, a zero-flux level can be easily explained in terms of geometrical occultation of an emitting region in the proximity of the surface by the NS itself.

Finally, the ($L_{\rm X}$, $P_{\rm spin}$, PF) combination shown by J0456 is very similar to that of the magnetar 1E 1048.1-5937. Tiengo et al. (2005) reported for this source $P_{\rm spin} \simeq 6.46$ s, $PF \simeq 91\%$ at a luminosity level of $L_{\rm X} \simeq 2.23 \times 10^{34}$ erg s^{-1} during *XMM-Newton* obs. 0112780401 (Observation A in Tiengo et al. 2005). Moreover, the spectral parameters they derived for the black bodies in the PL+BB and BB+BB models (first two models in Tab. 2 of the original article) are consistent with the ones we find for J0456 in our spectral analysis. In particular, in the BB+BB model for the hot (cold) component they derive $R_{\rm BB} \simeq 0.3$ km (1.7 km) and $kT_{\rm BB} \simeq 1$ keV (0.5 keV, see Observation A in Tab. 2 of Tiengo et al. 2005).

4.1.5 Conclusions

We have reported on the discovery of a 7.25-s pulsar in the outskirts of the LMC, 4XMM J045626.3–694723 (J0456). Based on *SALT* optical observations, we conclude that the only stellar object present within the X-ray uncertainty region is a faint, late-type (G8-K3 III) star. We discussed two scenarios for J0456: an accreting NS in a binary system with a late-type star companion (the first in the MCs) or an isolated NS, likely of the magnetar class.

When comparing the J0456 properties with those BeXRBs in the MCs and a few known Galactic X-ray pulsars in LMXBs/SyXBs with a similarly high magnetic field, the 0.3–10 keV luminosity $L_{\rm X} \simeq 2.7 \times 10^{34}$ erg s^{-1} of J0456 is too low for an accreting NS spinning at $\sim$7.25 s and with the magnetic field strength reported above. Moreover, the pulsed fraction of the signal $PF \simeq 86\%$ (with pulse minima consistent with null X-ray flux) is rarely observed in any accreting NS considered in

our sample (see Fig. 4.7). All these findings together make the accretion scenario unlikely. Nonetheless, if the accreting nature of J0456 were confirmed, it would represent the outcome of a novel evolutionary path in the MCs.

On the other hand, the characteristics of J0456 ($L_{\rm X}$, PF and $P_{\rm spin}$) are more commonly found in magnetars. In particular, another transient magnetar, 1E 1048.1-5937, shows a very similar spin period $P_{\rm spin} \simeq 6.46\,{\rm s}$ and similar pulsed fraction ($\simeq 91\%$) at low luminosities $L_{\rm X} \sim 2 \times 10^{34}\,{\rm erg\,s^{-1}}$ (Tiengo et al., 2005). If the new pulsar were a magnetar, it would represent the third known magnetar outside our galaxy and the second in the LMC.

An unambiguous classification of the new pulsar is complicated by the lack of a second measurement of the spin period which would have allowed us to infer the first derivative $\dot{P}_{\rm spin}$ of the spin period. Although our findings point to a new member of the magnetar class, we cannot totally exclude, at this stage, the possibility that the source is a peculiar accreting NS in a LMXB/SyXB.

Future observations of J0456 during its active state are needed in order to classify it. I am currently the PI of a *Swift* monitoring campaign of the source, which started in 2023. The field of view is routinely observed (about $\sim 6\,{\rm ks}$ every month), in order to promptly identify an active state of the source or any other uncatalogued source. The goal is to obtain a new estimate of J0456's spin period (and possibly the first estimate of its first time derivative) with other high-energy facilities (such as *XMM-Newton*) and/or to characterise any new source in the field.

At the time of writing (October 2024), the source has not entered the active state again. Two assumptions are needed to estimate the 3σ upper limit of the 0.3–10 keV flux of J0456. The first assumption is that the source has entered a quiescent state which does not change in time. In this case, all the *Swift* observations of the campaign can be merged to derive a single 3σ upper limit on the count rate of $\sim 7 \times 10^{-4}\,{\rm counts/s}$. The second assumption is that the source has entered a quiescent state where the spectral parameters are those derived for the PL model and the only difference is the normalization of the power law. Assuming the spectral parameters in Tab. 4.1 to convert the count rate in unabsorbed flux in the 0.3–10 keV band, the corresponding 3σ upper limit is $\sim 5 \times 10^{-14}\,{\rm erg\,cm^{-2}\,s^{-1}}$.

Chapter 5

Conclusions and future prospects

So long, and thanks for all the fish.

Douglas Adams, *The Hitchhiker's Guide to the Galaxy*

In this thesis, I have presented the two main works I carried out during my Ph.D. They are representative of the two research lines that have defined my activities during these last three years, i.e. the study of (P)ULXs and the search for new X-ray pulsators. For the former, the discovery of mHz-QPOs in a few PULXs has opened a new, fascinating window on the complex phenomenology of these extreme sources. We suggested in Imbrogno et al. (2024) that the presence of such features might be a phenomenon occurring at super-Eddington luminosities. Correspondingly, the study of these mHz-QPOs could represent a turning point in the study of PULXs, in the same way as QPOs in sub-Eddington Galactic X-ray pulsars allowed us to verify the beat frequency model (Lamb et al., 1985). For the latter, the discovery of a new candidate magnetar in the LMC (which, if the classification is confirmed, would represent only the third known magnetar outside our Galaxy; Imbrogno et al. 2023) shows the huge potential held by data mining projects. This discovery represents only the last example of a long list of new X-ray pulsators discovered thanks to EXTraS and CATS@BAR in the *XMM-Newton* and *Chandra* archives, respectively. The two fields are more intertwined than it might seem at first glance: given the small sample of known PULXs, any new addition can add valuable pieces to the puzzle. To do so, we can rely on both new observations and thorough searches in the archives. NGC 7793 P13 and NGC 5907 ULX-1 are two examples of PULXs whose nature as accreting NSs was unveiled thanks to a systematic and automated search for new X-ray pulsators in the *XMM-Newton* archive.

During these years, I also took part as a collaborator in various other projects related to both research lines. I will describe more in detail one of these projects in Appendix A, where I give an outline of eBANDERAS, a data mining pipeline which will collect the legacy of EXTraS and CATS@BAR and apply to the *eROSITA* archive the knowledge acquired in data mining in the last 10 years. In Appendix B, instead, I report a collection of relevant co-authored papers which are representative

of both my lines of research. In the meantime, many additional works started recently, or they need more time to be completed, works that I will carry on after the end of my Ph.D. These are the subjects of the remainder of this last chapter, together with possible expansions and new directions for the following years.

5.1 The study of PULXs

After 10 years from their discovery, the more we study PULXs, the more complex their phenomenology gets. New observations are crucial to better understand their behaviour and to try to comprehend their extreme accretion regime. At the time of writing (October 2024), I am waiting for a new approved *XMM-Newton* pointing (proposal ID 094339, of which I am the PI) of M51 ULX-7. Additionally, I recently (beginning of October 2024) submitted a proposal to continue observing M51 ULX-7 during the next *XMM-Newton* observing cycle. Our goal is to follow and study the evolution of either the spin pulsations after 5 years from the last detections, or the mHz-QPOs we detected during our 2021-2022 observations. At the same time, many ULX observations are contained in the *XMM-Newton* archive. A substantial fraction of this ULX population could be hiding PULXs for which we have not detected the spin pulsations yet. In parallel with new observations, therefore, the exploitation of X-ray archival data can help us in the study of these sources.

5.1.1 Identification of new candidates through machine learning

As described in Chap. 1, the detection of spin pulsations from PULXs is notoriously a difficult task, hampered by (rapidly) variable pulsed fractions, huge spin-up rates, orbital Doppler and a paucity of collected photons in short observations. The accelerated search techniques usually employed for the detection of the spin signals can also rapidly become computationally expensive and time-consuming. Focusing on a few, promising PULX candidates could save a significant amount of time. Still, the problem of how to identify promising candidates remains. From a spectral point of view, new PULX candidates can be singled out thanks to particularly hard energy spectra (Pintore et al., 2017; Gúrpide et al., 2021) and/or the presence of spectral features caused by intense magnetic fields, typical of accreting NSs (Brightman et al., 2018). However, both methods require a high number of collected photons to perform high-resolution spectroscopy.

An alternative approach we are currently testing at the Astronomical Observatory of Rome, in collaboration with the Politecnico of Milan, is the exploitation of machine learning and artificial intelligence techniques. Figure 5.1 shows an example of output from the clustering algorithm we are developing (Pinciroli Vago et al., in prep.) to identify new PULX candidates among ULXs with time series that do not allow to look for coherent signals due to poor statistic. We are applying the algorithm to all the observations available in the latest version of the *XMM-Newton* archive (4XMM-DR14) of the ULXs reported in the catalogue compiled by Walton et al. (2022). The algorithm defines two clusters, one containing (confirmed and candidate) PULXs and one with uncertain observations. The algorithm correctly grouped all the datasets of known PULXs in the PULX cluster, even those observations during

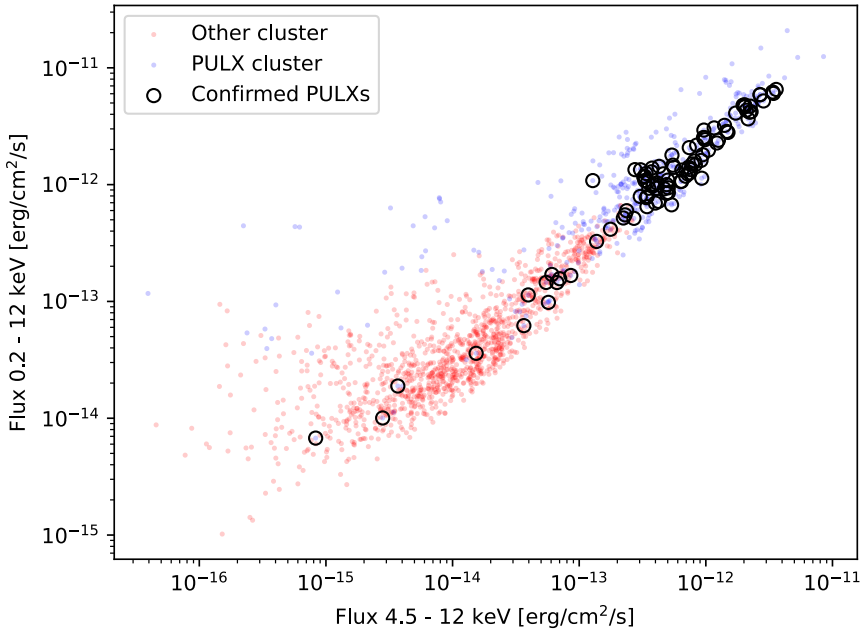

Figure 5.1. Example of output from our clustering algorithm. Each dot represents a different *XMM-Newton* observation of (P)ULXs in the catalogue by Walton et al. (2022). Red (blue) dots represent observations that the algorithm includes in the ULX (PULX) cluster. Black circles highlight the observations of known PULXs. Plot taken from Pinciroli Vago et al. (in prep.).

which the pulsations have not been detected. It also identified new candidates in the PULX cluster, candidates that we are currently verifying.

A further step we plan to add is a refined estimation of the flux and luminosities of the analysed sources. At the moment, we are using as input the values reported in 4XMM-DR14. For the catalogue, a mean absorption column and the same power-law model are used for every source to derive fluxes and luminosities. However, in the case of (P)ULXs this model does not represent well the real energy spectra. A fit with more adequate models could give us the necessary information to take a further step forward and move from the identification of those observations more likely to contain a PULX, to the direct classification of a source as a (P)ULX.

5.1.2 Study of (and automatic search for) mHz-QPOs in other (P)ULXs

In Chap. 2 I have shown that the detection of PULX spin signals could be even harder than previously thought, since the mechanism responsible for the mHz-QPOs in PULXs seems to be also responsible for a significant decrease in the pulsed fraction of the pulsations. At the same time, however, this discovery could have provided us with a new, independent tool to identify new PULX candidates.

The implications of this discovery have been widely discussed in Chap. 2. In Fig. 5.2 I show the ranges of QPO periods shown by the three PULXs for which mHz-QPOs have been detected. Given the small size of the sample, it is difficult

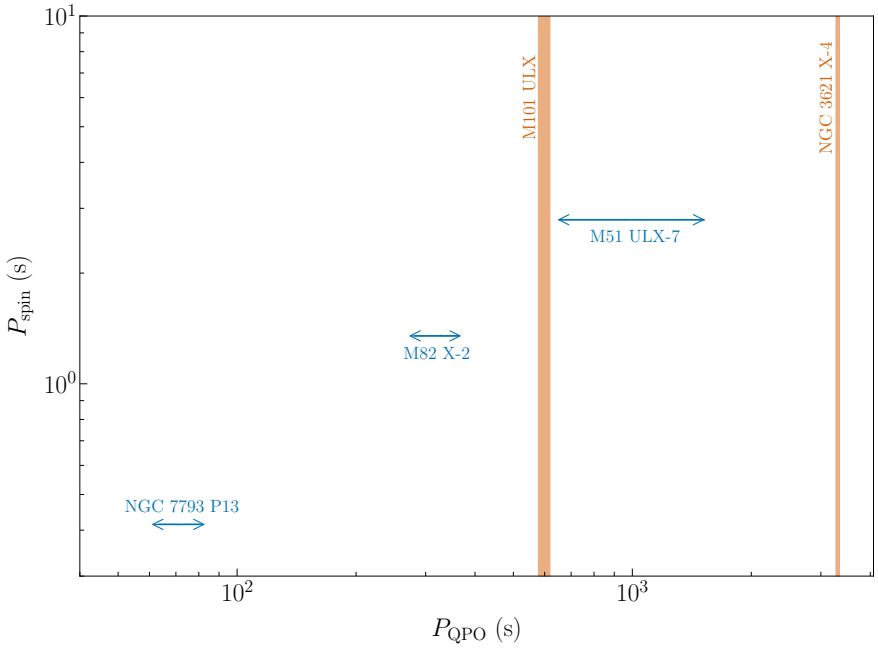

Figure 5.2. Ranges of observed spin periods $P_{\rm spin}$ and QPO periods $P_{\rm QPO}$ for the three PULXs for which both features have been detected. The individual PULXs are labelled in the figure. The orange vertical shaded regions show the observed period ranges of the QPOs detected in two other ULXs, i.e. NGC 3621 X-4 and M101 ULX. The ranges of $P_{\rm spin}$ are smaller than the line width for each PULX of the sample.

to draw definitive (and statistically significant) conclusions. However, there seems to be a tantalizing correlation between the period of the spin signal $P_{\rm spin}$ and the period (the inverse of the centroid frequency) of the QPO $P_{\rm QPO}$. If confirmed, such a relation could be exploited to focus the search for spin pulsations in candidate PULXs in a restricted frequency range. In Fig. 5.2 I also show the period ranges of the QPOs detected in two ULXs, i.e. NGC 3621 X-4 (Motta et al., 2020) and M101 ULX (Urquhart et al., 2022). In both papers the authors, starting from considerations on the time variability and the energy spectra, suggest that these ULXs host accreting NSs, even though they did not detect spin pulsations. These two sources, therefore, remain possible candidate PULXs. They could provide a way to verify this correlation: QPO periods of $P_{\rm QPO} \simeq 3000$ s and $P_{\rm QPO} \simeq 600$ s would correspond to spin periods $P_{\rm spin} \simeq 2$ s and $P_{\rm spin} \simeq 5 - 10$ s, respectively.

Only a handful of QPO detections in (P)ULXs have been reported in the literature. However, many more could be hidden in the X-ray archives. No systematic search for QPOs has been performed in the archival *XMM-Newton* observations of (P)ULXs. Such a search could represent a completely new way to exploit the *XMM-Newton* archive. I plan to carry this search out using STINGRAY, a Python package developed for timing analysis of X-ray data (Huppenkothen et al., 2019). In the meantime, I will start a collaboration with researchers located at Durham University to develop a theoretical model that could explain where the mHz-QPOs in PULXs come from. In particular, we will explore the possibility of an extension of the model proposed in Veresvarska et al. (2024), since a preliminary analysis has shown promising results.

5.2 Data mining of (X-ray) astrophysical archive

The fourth version of the *Uhuru* catalogue (the first catalogue ever of astrophysical X-ray sources; Forman et al. 1978) contained only 339 sources. Less than 50 years later, the last version of the *XMM-Newton* catalogue (4XMM-DR14) contains almost 700 000 sources. eRASS1, the catalogue of the first six months of observations covering the German sky performed by *eROSITA*, contains just under 930 000 sources. Such a fast growth has brought a huge step forward in the discovery and comprehension of high-energy sources and phenomena. At the same time, however, it is now harder and harder to single out new peculiar sources. In Chap. 3 and Chap. 4 I have shown how data mining projects, such as EXTraS and CATS@BAR, can help in the exploitation of the archives of X-ray missions with imaging capabilities. The results presented in those chapters represent only part of my contribution to these projects, with more sources waiting to be analysed. Moreover, given the ever-growing size of the (X-ray) astrophysical archives, data mining projects can only become increasingly crucial. I plan to use the lessons learned with *XMM-Newton* and *Chandra* to design and implement new, similar projects for both existing and future missions.

?? what does it mean

5.2.1 An AGN showing QPOs?

4XMM J045626.3–694723 is not the only source showing interesting time variability I discovered during these three years. During the last run of the post-EXTraS pipeline, when I discovered the new X-ray pulsator in the LMC, we also found other 7 previously unknown pulsators in the *XMM-Newton* archive. Moreover, within the framework of the CATS@BAR project, I found 2 sources in the *Chandra* archive with previously unknown (quasi-)periodic variability. In this section, I will focus on the most interesting of these last two sources.

2MASX J12571076+2724177 is a Sy-2 galaxy at a distance $d \simeq 90$ Mpc, hosting a SMBH (J1257 hereafter) with $\log(M_{\rm BH}/M_{\odot}) \simeq 6.3$ and a 2–10 keV luminosity $L_{\rm X} \simeq 2-4\times10^{41}$ erg s^{-1} (Liu et al., 2021). A search in the *Chandra* archive revealed that the light curve of the source is characterised by a quasi-periodic modulation at a timescale of $\simeq 7$ hr (Imbrogno, Sacchi et al., in prep.). Figure 5.3 shows a close-up view of the *Chandra* light curve of J1257. A total of 8 *Chandra* observations are available in the archive, 7 performed in 2020 and 1 in 2010: the modulation is detected in every observation. J1257 would therefore be the first SMBH in a Sy-2 galaxy with a QPO in the X-ray flux. At the moment, we are analysing all the available *Chandra* and *XMM-Newton* observations in the archives, to characterise both the spectral emission and the temporal variability of the source.

5.2.2 Disseminating data mining techniques: pipelines for all (the wavelengths)

Finally, given the ever-increasing importance of data mining in modern (high-energy) astrophysics, our long-term goal is to release the software we developed during these years to the scientific community. The clustering algorithm for the identification of new PULX candidates discussed in Sect. 5.1.1 is one of the pieces of

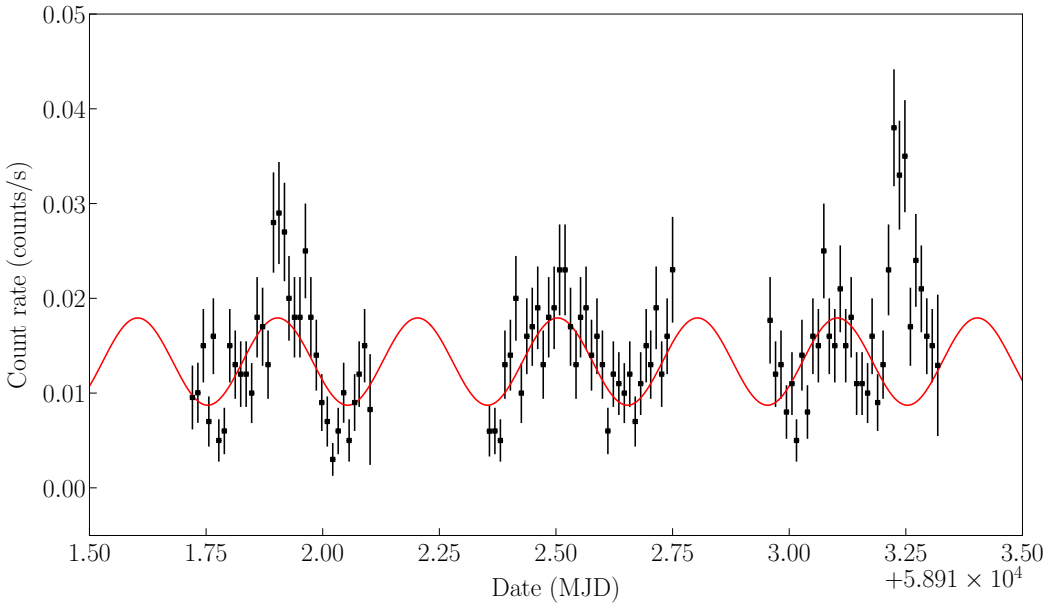

Figure 5.3. Close-up view of the *Chandra* light curve of the central AGN of 2MASX J12571076+2724177. Superimposed in red is the fit of the 7 hr-long quasi-periodic modulation we detected. A few cycles are shown to guide the eye. Plot taken from Imbrogno, Sacchi et al. (in prep.).

code we are considering for future releases. Another example is the pipeline we are developing to analyse *eROSITA* data and, in particular, the `dpspy` module, both described in Appendix A. The different pieces of code are being written in Python and as user-friendly as possible, with the plan to release them through the STINGRAY package (Huppenkothen et al., 2019), which is becoming a standard software for spectral-timing analysis. Our hope is that our effort will make systematic and automated searches in large archives easier and more accessible to non-specialized scientists.

Although we developed these pipelines to analyse the data in the archives of specific missions (*XMM-Newton*, *Chandra*, and now *eROSITA*), they are highly flexible. They are built to be as mission-independent as possible and easy to configure for different missions. We have already tested some of them (e.g. `dpspy`) on data coming from other X-ray telescopes, such as *Swift*, *NuSTAR*, and *NICER*. Preliminary results also show that they can be used to analyse in a short time optical data from optical photometers too, such as SiFAP2 (Ghedina et al. 2018; see also Appendix A). With such versatility, our hope is that this work can represent a crucial legacy for the study of PULXs (and X-ray pulsators in general) with future missions, such as *NewAthena* and *eXTP*.

Appendix A

eBANDERAS: the hunt for variable sources in the *eROSITA* data

It's not a bug; it's an undocumented feature.

Anonymous

Launched in 2019, the extended ROentgen Survey with an Imaging Telescope Array (*eROSITA*) is the soft X-ray telescope on board the Russian-German Spectrum-Roentgen-Gamma (SRG) observatory. Developed by the Max Planck Institute for Extraterrestrial Physics (MPE), it has been designed to follow the path of *ROSAT* (Truemper, 1982). When in survey mode, the spacecraft has a revolution time of 4 h (or, equivalently, a scan rate in declination of $0.025\,\mathrm{deg\,s^{-1}}$), covering a position in the scan path six times per day. A given sky area is observed every six months (see Fig. A.1 for the exposure map of the first all-sky survey). With this strategy and a large field of view (with a diameter of $\approx 1°$), *eROSITA*'s purpose is to collect the most sensitive survey ever of the X-ray sky in the 0.2–2.3 keV band (see Predehl et al. 2021 for a complete review of *eROSITA* specifics) and provide the first ever imaging all-sky survey in the 2.3–8 keV band. Eight all-sky surveys were planned, but only the first four had been completed when *eROSITA* was put in stand-by at the beginning of 2022.

In January 2024, the *eROSITA* German consortium (eROSITA-DE)[1], which has exploitation rights for data with Galactic longitude $l > 180°$ (the "German sky"), released the catalogue of the sources detected in the German sky during the first of the four completed all-sky surveys (eRASS1). Although still partial, eRASS1 is already the largest X-ray archive ever, with almost 930 000 catalogued sources (Merloni et al., 2024). Given the size of the *eROSITA* archive, a data mining approach to search for peculiar sources is the only feasible way to exploit it.

[1] A full list of articles published by eROSITA-DE is available here. Among them, it is worth mentioning the detections of quasi-periodic eruptions (QPEs) from two previously quiescent galaxies (Arcodia et al., 2021), the discovery of various XRBs hosting NSs in both the Small and Large Magellanic Clouds (see e.g. Haberl et al., 2023a,b) and the first detection in the X-ray band of a nova during the initial fireball phase (König et al., 2022).

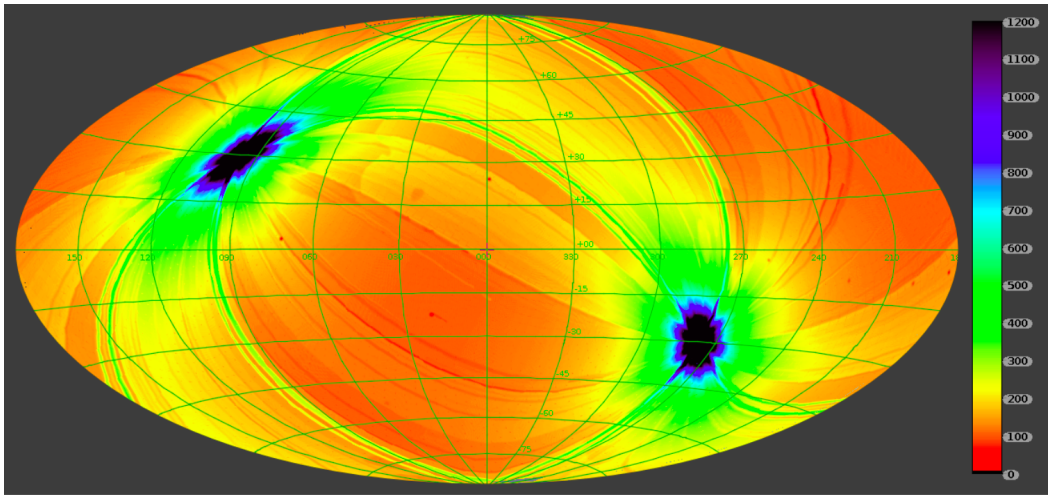

Figure A.1. *eROSITA* effective exposure map in Galactic coordinates, derived from eRASS1 data. The corrected exposure time is expressed in seconds and can vary from ∼100 s at the ecliptic equator to more than 10 000 s close to the ecliptic poles. Plots taken from Predehl et al. (2021).

A.1 Structure of the pipeline

Following the path laid out by the previous data mining projects from our groups (see Chap. 3), we aim to develop a pipeline (eBANDERAS) devoted to an automated and systematic search for X-ray variability in the *eROSITA* data. The pipeline will be the result of a collaboration between the High-Energy Astrophysics Group at the Observatory of Rome and the MAGNESIA group at the Institute of Space Science (ICE) in Barcelona. *eROSITA* has a time resolution of ≈ 50 ms, which potentially allows the detection of coherent pulsations with periods as low as $P \sim 100$ ms. Early Data Release (EDR) observations, moreover, contain pointing observations of selected fields, with exposure times as long as a few tens of kiloseconds. *eROSITA* surveys and EDR data can therefore allow us to study the time scale of the variability of an X-ray source over several orders of magnitude.

A flowchart of the current structure of eBANDERAS is shown in Fig. A.2. The pipeline is being written in Python and exploits packages with proven reliability such as STINGRAY (Huppenkothen et al., 2019) and ASTROPY (Astropy Collaboration et al., 2022). Our goal is to have a pipeline that is as mission-independent as possible and flexible enough to be applied to future missions with as few changes and additions as possible. The mission-independent steps (typically represented by a dedicated module) are highlighted in green in the flowchart. They are associated with the timing/spectral analysis part of the pipeline. Some steps, however, will always rely upon mission-specific software. Blue boxes represent these steps in the flowchart. This is the case, for example, of the data reduction part, for which each X-ray mission (e.g., *XMM-Newton*, *Swift* and *Chandra*) has its own software (SAS, HEASOFT and CIAO, respectively). eBANDERAS requires the prior installation

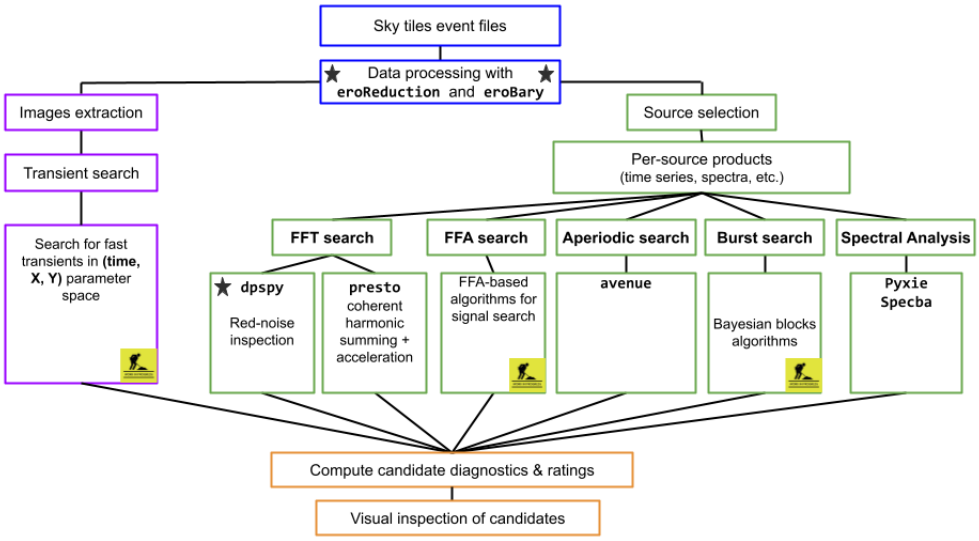

Figure A.2. Flowchart of the pipeline. Blue boxes represent mission-dependent steps and modules. Green boxes represent mission-independent steps and modules. Violet boxes represent the transient search part of eBANDERAS. Orange boxes represent the final checks and storage steps. The modules and tools I am in charge of are marked with a star. A work-in-progress sign has been added near those parts of the pipeline and modules that need further testing.

of HEASoft[2] and eSASS[3] (eROSITA Science Analysis Software System, Brunner et al. 2018). eBANDERAS is also highly configurable thanks to a dedicated YAML configuration file which is read by the pipeline and where the user can customize the pipeline steps (e.g. by defining the energy range of interest, the desired minimum time bin for the light curves and so forth).

A.2 Personal contribution

The pipeline is the result of the effort of many people, each working on different modules. I am in charge of the data reduction module, of the barycentric correction tool and of a Python/Fortran module aimed at the search for periodic signals through Fourier analysis.

A.2.1 Data reduction and barycentric correction modules

`eroReduction` carries out the task of reducing the raw FITS files and extracting the files for the subsequent analysis. The module follows the guidelines reported in the eSASS cookbook[4]. We adopted the convention of starting the name of every mission-dependent module with the name of the associated mission, such as `ero` in the case of *eROSITA*. `eroReduction` can be used both for single sources and in

[2] https://heasarc.gsfc.nasa.gov/lheasoft/download.html
[3] https://erosita.mpe.mpg.de/dr1/eSASS4DR1/eSASS4DR1_installation/
[4] https://erosita.mpe.mpg.de/edr/DataAnalysis/esasscookbook.html.

"pipeline mode". In the first case, the task requires the source regions among other inputs. Otherwise, when in pipeline mode, the user can decide whether to run the source detection chain with customized options or use an external catalogue to select the sources, like eRASS1. For each source, `eroReduction` extracts event files, light curves and energy spectra.

Before the release of the latest version of eSASS, I had also developed a Python module to apply the barycentric correction to *eROSITA* data, i.e. `eroBary`. At the time, eSASS lacked such a tool, crucial for the timing analysis of coherent periodicities. Although eSASS now includes `ebarycen` to perform this task, we found that our tool is more flexible. For example, `ebarycen` requires the user to split the event files into seven different files, one for each telescope module, to work correctly. `eroBary`, on the other hand, automatically checks how many modules were active during the observation, creates a different event file for each telescope module, performs the barycentric correction and merges the files back together. We tested `eroBary` on EDR observations of known pulsars (e.g., PSR B0656+14 and PSR J0537–6910) and found that the derived periods are consistent with those expected using the known timing solution. We also verified that `ebarycen` and `eroBary` give the same result.

The event files produced for each source are then passed as input to the timing analysis modules. These modules can be divided into four groups:

1. search for coherent periodic signals through algorithms based on Fast Fourier Transform (FFT; van der Klis 1989a);
2. search for coherent periodic signals through algorithms based on Fast Folding Algorithms (FFA; for a description of the algorithm, see Morello et al. 2020);
3. search for aperiodic variability in the light curve;
4. search for transient and burst events.

I will focus on group 1, for which I developed the module described in the following section.

A.2.2 `dpspy`: periodicity search through Fourier analysis

`dpspy` is a module dedicated to the detection of peaks associated with periodic signals in a PDS. This module is based on the work by Israel and Stella (1996) and it wraps the original Fortran code in a Python script, allowing for fast computation for PDS with up to $\sim 16 \times 10^6$ Fourier frequencies. The code computes a frequency-dependent detection threshold through a logarithmic smoothing of the original PDS. If a peak is detected, `dpspy` prints the PDS together with the 3.5σ detection threshold. It also prints the frequency, the single-trial probability, and the significance of the peak over the whole analysed frequency range. If no peaks are found above the detection threshold, a 3σ upper limit on the signal's pulsed fraction is computed over the analysed frequency range and printed together with the PDS. An example of the output of `dpspy` is shown in Fig. A.3.

`dpspy` has different options that allow the user to choose the analysed frequency range (the default is a search over the whole PDS) and the bintime of the time series

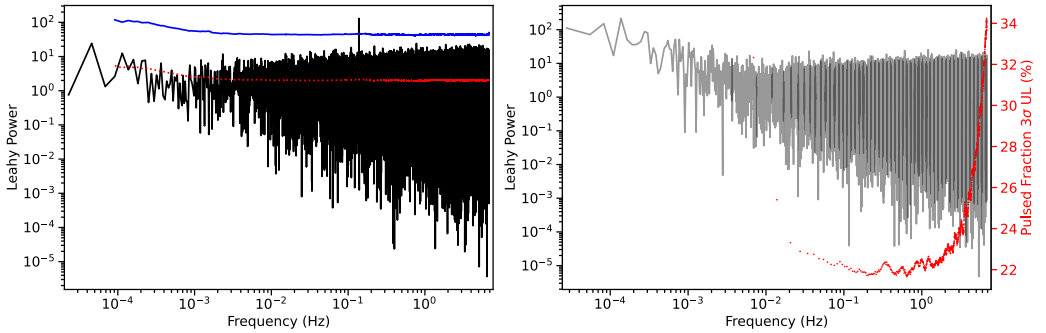

Figure A.3. Left panel: example of `dpspy` output when a signal is detected. The blue line shows the 3.5σ detection threshold, while the red dotted line shows the smoothed PDS. Right panel: example of `dpspy` output when no signal is detected. The red dotted line and the right y-axis show the 3σ upper limit on the pulsed fraction as a function of the frequency.

(the default is the maximum time resolution given by the instrument configuration). The user can also choose to skip the plot visualization and directly save the results of the computation in a PDF file, to speed up the process. This is particularly useful when the module is called multiple times in a systematic search. I tested `dpspy` on event files from different instruments, both in the X-ray (*XMM-Newton*, *Chandra*, *NICER*, *NuSTAR*, *eROSITA*, *Swift*) and the optical (SiFAP2, mounted at TNG; Ghedina et al. 2018) band. Other instruments can be added with ease by simply adding the `TELESCOP` keyword as a key in a dedicated Python dictionary and the associated maximum time resolution.

A.3 Current status and future prospects

At the moment, the pipeline and the tests are being run on the computer cluster "Hidra", owned by the ICE (CSIC-IEEC), made up of 13 independent nodes. The primary disk node has 48 threads and 256GB of RAM, mainly serving as storage. The remaining 12 computing nodes each have 64 threads and 384GB of RAM, dedicated to computational tasks. We will apply eBANDERAS to both EDR and eRASS1 data. EDR data contains pointing observations with long exposure times. These are the *eROSITA* observations for which `dpspy` is expected to find most of the serendipitous pulsators. eRASS1 data, on the other hand, are more suited for the search of aperiodic, long-term variability, given the survey strategy.

We are finalising our work on the modules based on FFA and the search for burst events. We also verified that PRESTO[5] works with *eROSITA* data and we started implementing a PRESTO-based module that includes harmonic summing to search for coherent periodic signals in the PDS. The burst search algorithm will be based on a Bayesian blocks approach (Scargle et al., 2013) and on the algorithm developed for EXTraS. Any source (unidentified or already classified) with previously unknown (a)periodic variabilities could, in principle, lead to future publications.

Moreover, we plan to make the pipeline publicly available. eBANDERAS is also

[5] https://github.com/scottransom/presto.

the first step toward building a multi-mission pipeline that can be used for different X-ray missions. This upgrade could include active missions with imaging capabilities, such as *XMM-Newton*, *Chandra* and *NuSTAR*, whose archives are already public. In the long term, the modular nature of the pipeline could allow us to add future missions, or missions whose archives are not publicly available yet, such as *Einstein Probe*, once the data are released to the public.

Appendix B

Relevant co-authored papers

Okay! One more thing...

Lin-Manuel Miranda as Alexander Hamilton,
Hamilton: An American Musical

The works discussed in this thesis represent the two main projects that have been taking up most of the last three years. In this appendix, I report a selection of relevant co-authored papers. For a full list of publications in which I am involved, see here.

B.1 The restless population of bright X-ray sources of NCG 3621
Sacchi, Imbrogno et al. (2024)

B.1.1 Main results

We report on the multi-year evolution of the population of X-ray sources in the nuclear region of NGC 3621 based on *Chandra*, *XMM-Newton* and *Swift* observations. Among these, two sources, X1 and X5, after their first detection in 2008, seem to have faded below the detectability threshold, a most interesting fact as X1 is associated with the AGN of the galaxy. Two other sources, X3 and X6 are presented for the first time, the former showing a peculiar short-term variability in the latest available dataset, suggesting an egress from eclipse, hence belonging to the handful of known eclipsing ultra-luminous X-ray sources. One source, X4, previously known for its "heart-beat", i.e. a characteristic modulation in its signal with a period of $\approx 1\,\mathrm{h}$, shows a steady behaviour in the latest observation. Finally, the brightest X-ray source in NGC 3621, here labelled X2, shows steady levels of flux across all the available datasets but a change in its spectral shape, reminiscent of the behaviours of Galactic disk-fed X-ray binaries.

B.1.2 Personal contribution

I performed the data reduction and the timing analysis of the *XMM-Newton* observations analysed in the paper. The two panels in Fig. B.1 show the two most

interesting results from this analysis. The top panel shows the background-subtracted light curve of X3 during the 2023 *XMM-Newton* observation. The egress of an eclipse is clearly visible, with the mean count rate of the source being consistent with the zero-flux level in the first 40 ks of observation. This discovery led us to classify this source as one of the few known eclipsing ULXs (Fabrika et al., 2021). The detection of an eclipse allowed us to constrain the inclination of the system $i \lesssim 75°$. The whole observation lasted for ≈ 90 ks, which we set as the lower limit on the orbital period. The eclipse pattern shows some similarities with the two eclipsing ULXs in M51 (Urquhart and Soria, 2016) and LMC X–4 (see Jain et al., 2024, and references therein). Given that all these sources are HMXBs, it is reasonable to assume that X3 is also a HMXB. Unfortunately, the paucity of available data prevented us from a deeper analysis of this source.

The bottom panel of Fig. B.1 shows the PDS of X4 during the 2023 *XMM-Newton* observation. In 2017 the source exhibited a peculiar quasi-periodic oscillation ($P \simeq 1$ hr) in its flux (Motta et al., 2020). The repeating pattern of the modulation was reminiscent of the heart-beat of GRS 1915+105 (Belloni et al., 2000). The dash-dotted line at 0.3 mHz shows the frequency of the central peak of the heart-beat detected in 2017. In 2023, this feature is completely absent, although the spectrum and luminosity level is consistent with those of 2017. The erratic behaviour of X4 feature strengthens the association with GRS 1915+105, whose heart-beats are probably not solely triggered by the accretion rate.

B.2 Investigating the nature of the 2.4 hr-period eclipsing cataclysmic variable W2 in 47 Tuc
Amato, La Palombara, Imbrogno et al. (2024)

B.2.1 Main results

W2 (CXOGlb J002415.8–720436) is a cataclysmic variable (CV) in the Galactic globular cluster 47 Tucanae. Its modulation was discovered within the CATS@BAR project. The source shows all the properties of magnetic CVs, but whether it is a polar or an intermediate polar is still a matter of debate. This paper investigates the spectral and temporal properties of the source, using all archival X-ray data from *Chandra* and *eROSITA* Early Data Release, to establish whether the source falls within the category of polars or intermediate polars. We fitted *Chandra* archival spectra with three different models: a power law, a bremsstrahlung and an optically thin thermal plasma. We also explored the temporal properties of the source with searches for pulsations with a power spectral density analysis and a Rayleigh test (Z_n^2). W2 displays a mean luminosity of $\sim 10^{32}$ erg s^{-1} over a 20-year span, despite lower values in a few epochs. The source is not detected in the latest observation, taken with *Chandra* in 2022, and we infer an X-ray luminosity $\leq 7 \times 10^{31}$ erg s^{-1}. The source spectral shape does not change over time and can be equally well fitted with each of the three models, with a best-fit photon index of 1.6 for the power law and best-fit temperatures of 10 keV for both the bremsstrahlung and the thermal plasma models. We confirm the previously detected period of 8649 s, ascribed to the binary orbital period, and found a cycle-to-cycle variability associated with

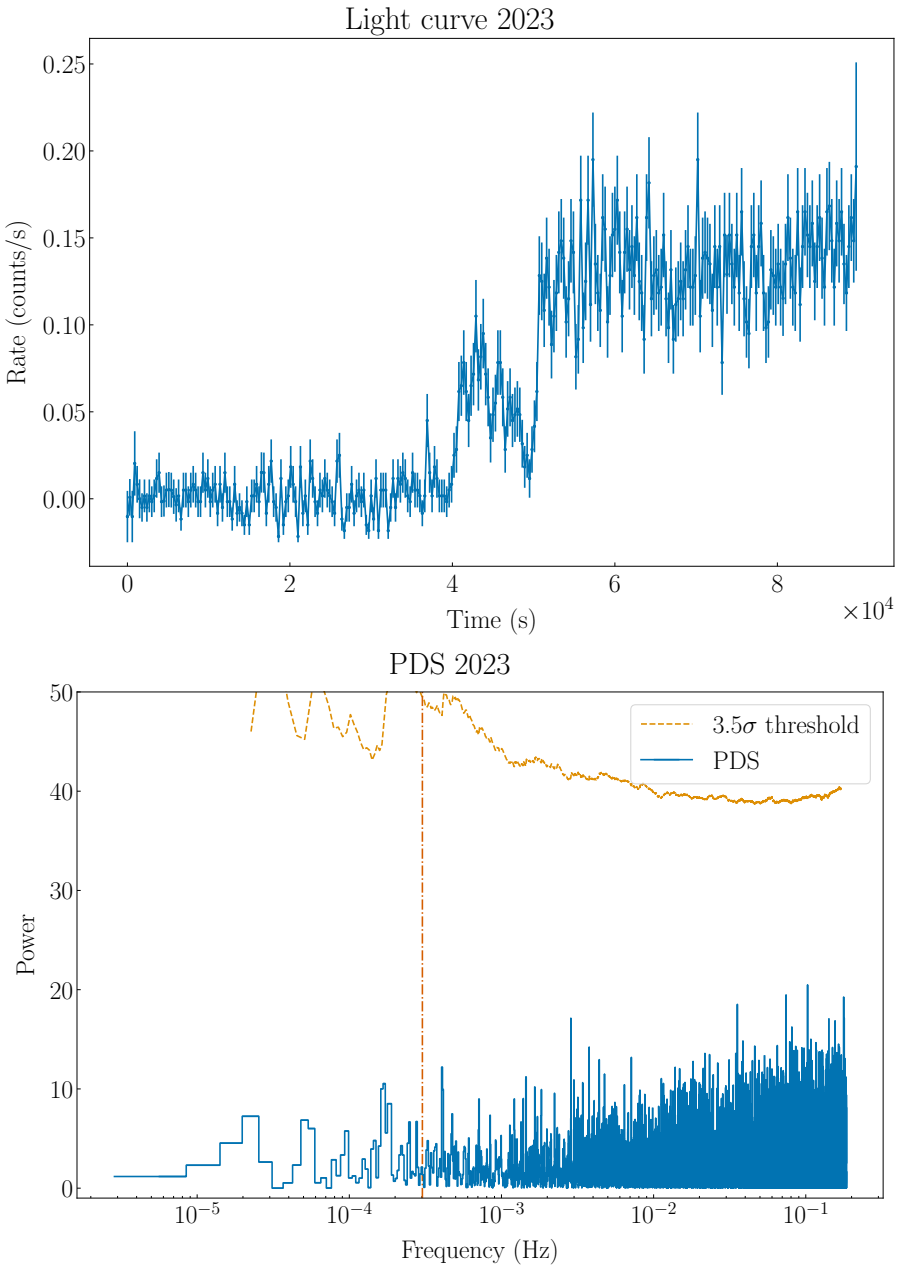

Figure B.1. Top: X3 PN+MOS light curve in the 0.3–10 keV band during the 2023 *XMM-Newton* observation. The bin time of the background-subtracted light curve is 300 s. Bottom: X4 PN+MOS power density spectrum in the 0.3–10 keV band during the 2023 *XMM-Newton* observation. The dash-dotted line at $\simeq 0.3$ mHz shows the frequency of the main peak detected in the PDS in the 2017 *XMM-Newton* observation. The yellow dashed line in the PDS shows the 3.5σ detection threshold. Plots taken from Sacchi, Imbrogno et al. (submitted).

this periodicity. No other significant pulsation is detected. Considering the source orbital period, luminosity, spectral characteristics, long-term evolution and strong cycle-to-cycle variability, we suggest that W2 is a magnetic CV of the polar type.

B.2.2 Personal contribution

The two panels in Fig. B.2 show the main results of my contribution to the paper. Magnetic CVs (mCVs, with $B \sim 10^6 - 10^8$ G) are divided into two main classes, according to the strength of their magnetic fields (see e.g. Section 11 of Page and Shaw 2022 for a review): polars and intermediate polars (IPs). In the case of polars, the B field is strong enough that the interaction with the companion synchronizes the WD spin period $P_{\rm spin}$ with the orbital period ($P_{\rm spin} = P_{\rm orb}$). On the other hand, the lower B fields of IPs prevent this synchronization and typically $P_{\rm spin} \ll P_{\rm orb}$. W2 was unambiguously classified as a CV, i.e. a binary system consisting of a white dwarf (WD) accreting from a companion star, by Israel et al. (2016b), when they detected an 8 minute-long eclipse every $P_{\rm orb} \simeq 8649$ s in *Chandra* ObsIDs 953, 955 and 2735–8. In the previous years, however, different values for this period had been proposed (see e.g. Edmonds et al. 2003). Recently, Bao et al. (2023) used the Gregory-Loredo algorithm (Gregory and Loredo, 1992) on *Chandra* ObsID 2375–8 and reported the detection of two periodic signals from W2, at 8646.78 s and 3846.15 s. They interpreted the first signal as the orbital period and the second as the spin period, and therefore classified W2 as an IP. To solve the controversy on the presence and nature of the different X-ray periods, I performed part of the timing analysis of the *Chandra* observations. In particular, I performed a Z_n^2 search (Buccheri et al., 1983) for periodicity in the 0.1–0.6 mHz range using the `HENzsearch` tool included in the `HENDRICS` package (Bachetti, 2018). The top panel of Fig. B.2 shows the results of this analysis. Both the fundamental ($\nu \simeq 116\,\mu$Hz, $n = 4$) and the second harmonic ($\nu \simeq 231\,\mu$Hz, $n = 1$) of the 8649 s-long period are clearly detected, while the 3846.15 s signal reported by Bao et al. (2023) is below the 3.5σ detection threshold.

We also found that *eROSITA* had observed 47 Tuc in two epochs in November 2019 (ObsIDs 700011, 700163, 700013, 700014 and ObsIDs 700173-175) during the calibration phase. I performed the data reduction and timing analysis for the *eROSITA* EDR data. W2 cannot be resolved by *eROSITA* due to the high source density in the core region of 47 Tuc (Saeedi et al., 2022). Additionally, the 15″-radius region used to extract the source events includes another CV (W1), which might contaminate the data. Nevertheless, epoch folding at the period discovered in *Chandra* data produced the same eclipse profile at $P = 8649$ s as observed in *Chandra* data. The lower panel of Fig. B.2 displays the phase-folded profiles of both *eROSITA* epochs, where the background correction accounts for the anticipated count rate of the other bright source W1 within the source extraction region in the *eROSITA* energy band. This estimation is based on the Heinke et al. (2005) analysis of *Chandra* archival observations where W1 is detected. W2's eclipse profile shape aligns with that found in *Chandra* data, thereby confirming the detection of the source. We also attempted to fold *eROSITA* light curves at the period of $P \simeq 3846.15$ s and found a profile similar to that reported by Bao et al. (2023). However, similar profiles can be obtained with any period within the 3746–3946 s

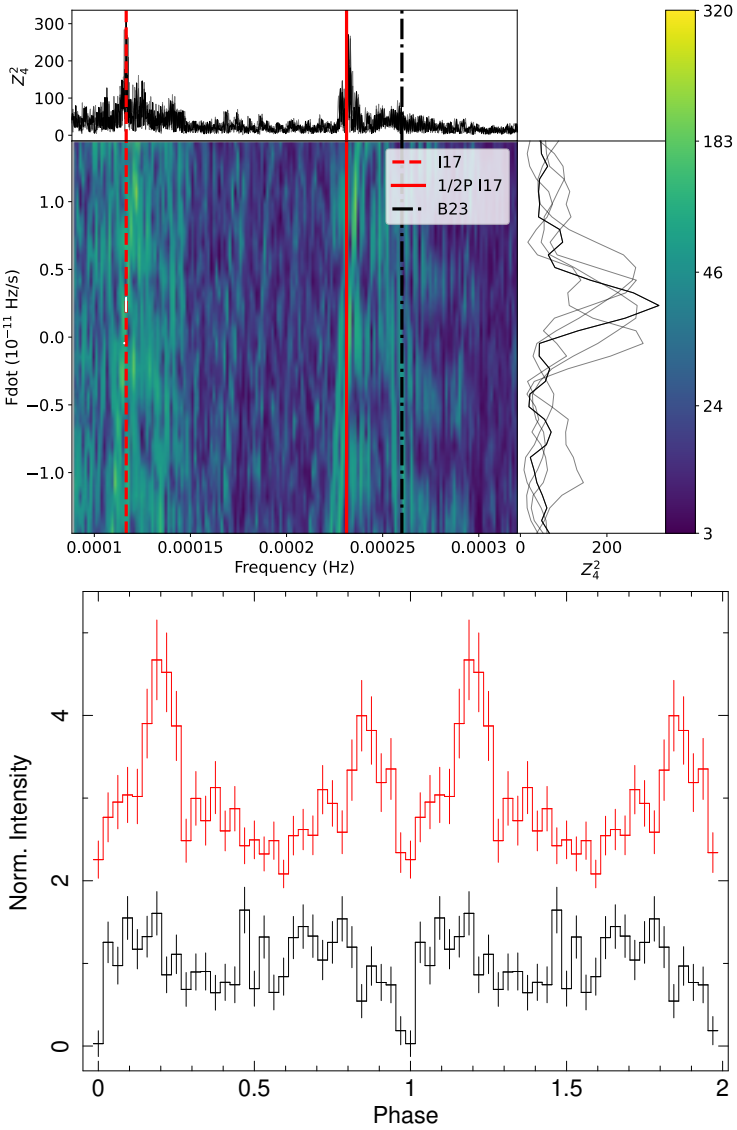

Figure B.2. Top: Z_N^2 search with $N = 4$ harmonics of *Chandra* ObsIDs. 2735–2738. The fundamental and the first harmonic of the period at $P \simeq 8650$ s are marked with red dashed and solid lines, respectively, while the period proposed by Bao et al. (2023) is marked with a black dash-dotted line. Bottom: Phase-folded profile ($P = 8649$ s) in *eROSITA* data from the observations on November 1-2, 2019 (black profile, reference epoch 58787.991(1) MJD, 1σ c.l.) and on November 19, 2019 (red profile, shifted on the y-axis for better visualization). The latter has also been arbitrarily shifted along the x-axis to align the eclipse phase. Plots taken from Amato, La Palombara, Imbrogno et al. (submitted).

range.

B.3 Probing the nature of the low state in the extreme ultraluminous X-ray pulsar NGC 5907 ULX1 Fürst et al. (2023)

B.3.1 Main results

NGC 5907 ULX1 is the most luminous pulsating ultraluminous X-ray source (PULX) known to date, reaching luminosities in excess of $10^{41}\,\mathrm{erg\,s^{-1}}$. The pulsar is known for its fast spin-up during the on-state. Here, we present a long-term monitoring of the X-ray flux and the pulse period between 2003 and 2022. We find that the source was in an off- or low-state between mid-2017 to mid-2020. During this state, our pulse period monitoring shows that the source had spun down considerably. We interpret this spin-down as likely being due to the propeller effect, whereby accretion onto the neutron star surface is inhibited. Using state-of-the-art accretion and torque models, we use the spin-up and spin-down episodes to constrain the magnetic field. For the spin-up episode, we find solutions for magnetic field strengths of either around 10^{12} G or 10^{13} G, however, the strong spin-down during the off-state seems only to be consistent with a very high magnetic field, namely, $>10^{13}$ G. This is the first time a strong spin-down is seen during a low flux state in a PULX. Based on the assumption that the source entered the propeller regime, this gives us the best estimate so far for the magnetic field of NGC 5907 ULX1.

B.3.2 Personal contribution

I performed the data reduction of the *XMM-Newton* observations and contributed to the interpretation of the results. Fig. B.3 shows the long-term evolution of the spin period, where both spin-up and (for the first time in this source) spin-down episodes are visible.

B.4 A soft and transient ultraluminous X-ray source with 6-h modulation in the NGC 300 galaxy Sacchi et al. (2024a)

B.4.1 Main results

We investigate the nature of CXOU J005440.5-374320 (J0054), a peculiar bright ($\sim 4 \times 10^{39}\,\mathrm{erg\,s^{-1}}$) and soft X-ray transient in the spiral galaxy NGC 300 with a 6-hour periodic flux modulation that was detected in a 2014 *Chandra* observation. Subsequent observations with *Chandra* and *XMM-Newton*, as well as a large observational campaign of NGC 300 and its sources performed with the *Swift Neil Gehrels Observatory*, showed that this source exhibits recurrent flaring activity: four other outbursts were detected across ∼8 years of monitoring. Using data from the *Swift*/UVOT archive and from the *XMM-Newton*/OM and *Gaia* catalogues, we

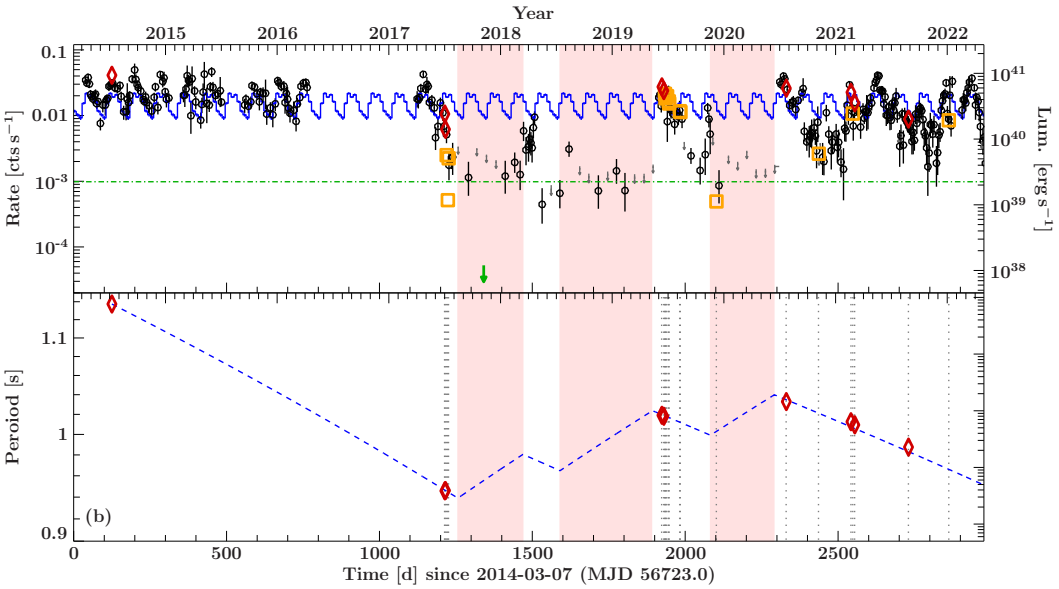

Figure B.3. Flux and period evolution of NGC 5907 ULX-1 between 2014 and 2022. Top: *Swift*/XRT light curve (0.3–10.0 keV). In green the upper limit for the point source luminosity as measured with *Chandra* (Belfiore et al., 2020) is shown, using the right y-axis. The *XMM-Newton* luminosities are shown as red diamonds and orange squares for observations with and without detected pulsations, respectively, also using the right-hand y-axis. The horizontal green line indicates the estimated propeller luminosity based on a magnetic field strength of $B = 2.6 \times 10^{13}$ G. The blue curve shows an extrapolation of the 78 d X-ray period seen from NGC 5907 ULX1 during its ULX state (Walton et al., 2016b). The shaded pink areas indicate where the source was conceivably in the low state and spinning down. Bottom: pulse period measurements, as listed in Table 1 of the original paper and Israel et al. (2017a). The grey vertical dotted lines indicate times of observations with *XMM-Newton*. The blue dashed line shows a possible fiducial model of epochs of spin-up during bright states interspersed with spin-down during off-states. This line is only a suggestion for the evolution of the period. Plot taken from Fürst et al. (2023).

noted the source is likely associated with a bright blue optical/ultraviolet counterpart. This prompted us to perform follow-up observations with the *Southern African Large Telescope* in December 2019. With the multi-wavelength information at hand, we discuss several possibilities for the nature of J0054. Although none is able to account for the full range of the observed peculiar features, we found that the two most promising scenarios are a stellar-mass compact object in a binary system with a Wolf–Rayet star companion, or the recurrent tidal stripping of a stellar object trapped in a system with an intermediate-mass ($\sim 1000\,M_\odot$) black hole.

B.4.2 Personal contribution

I contributed to the data reduction of *XMM-Newton* data analysed for this paper. I also contributed to the timing analysis and characterization of the short-term variability of the *Chandra* data in which the 6 h modulation has been detected. Both the light curve and the PDS of the 2014 *Chandra* observation are shown in Fig. B.4. The modulation was not significantly detected in the last *Chandra* pointing, but the associated 3σ upper limit on the pulsed fraction is particularly high ($\simeq 50\%$).

B.5 The orbit of NGC 5907 ULX-1 Belfiore et al. (2024)

B.5.1 Main results

We report on the orbit of the binary system powering the most extreme ultraluminous X-ray pulsar known to date: NGC 5907 ULX-1 (ULX1). ULX1 has been the target of a substantial multi-instrument campaign, mainly in the X-ray band, but no clear counterparts are known in other bands. Although ULX1 is highly variable and pulsations can be transient (regardless of the source flux), the timing data collected so far allow us to investigate the orbit of this system. We find an orbital period $P_{orb} = 5.7^{+0.1}_{-0.6}$ d and a projected semi-axis $A_1 = 3.1^{+0.8}_{-0.9}$ lts. The most likely ephemeris is: $P_{orb} = 5.6585(6)$ d, $A_1 = 3.1(4)$ lts, and the epoch of ascending nodes passage is: $T_{asc} = 57751.37(5)$ MJD. However, there are 6 similar solutions, acceptable within 3σ. We find further indications that ULX1 is a high-mass X-ray binary. This implies that we are observing its orbit face-on, with an inclination < 5 deg.

B.5.2 Personal contribution

I contributed to the data analysis and the interpretation of the results. Fig. B.5 shows the final estimates of the orbital period and projected semi-axis. I checked the orbital solution using the `ell1fit`[1] code developed by Bachetti et al. (2022) to study the orbital parameters of M82 X-2.

[1] https://github.com/matteobachetti/ell1fit.

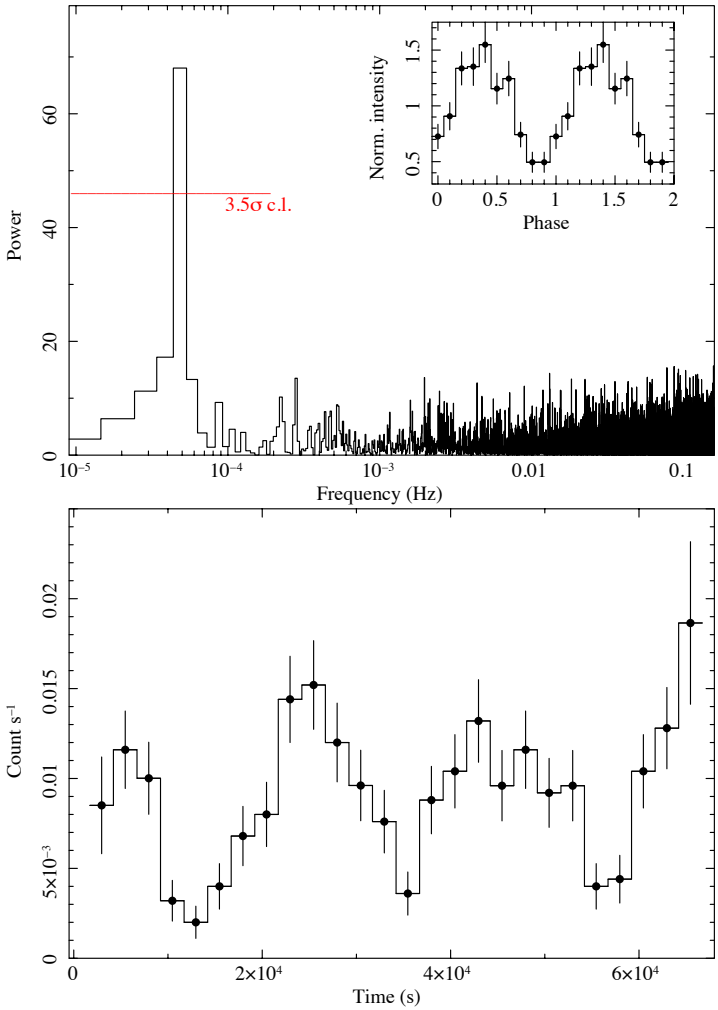

Figure B.4. Timing analysis of J0054. Top panel: Fourier power spectrum of the *Chandra* data of J0054. The red line indicates the local 3.5σ detection threshold adopted in the CAT @ BAR project. The prominent peak well above the threshold (5.9σ) corresponds to the $\sim$6 h modulation of J0054. The inset shows the pulse profile obtained by folding the data at the best period of 5.88 ± 0.12 h. Bottom panel: Light curve (the background is negligible). The bin time is 2500 s. Plots taken from Sacchi et al. (2024b).

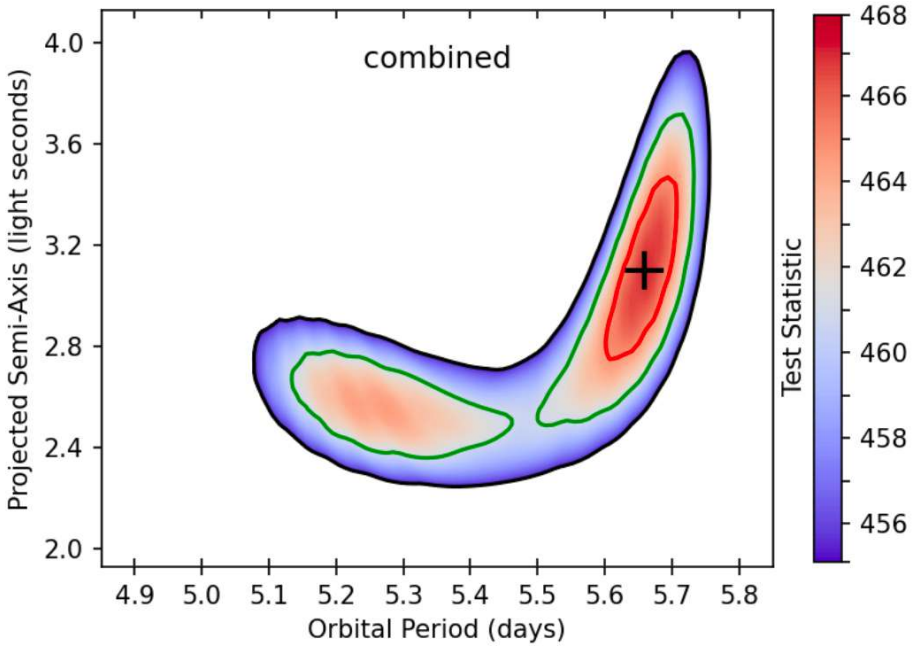

Figure B.5. Estimates of the orbital period (P_{orb}, on the X-axis) and the projected semi-axis (A_1, on the Y-axis) of the orbit of NGC 5907 ULX-1. These estimates are profiled over the orbital phase (T_{asc}). A black cross marks the most likely value of $P_{orb} = 5.66$ d and $A_1 = 3.10$ lts . Level curves indicate the 1σ (red), 2σ (green), and 3σ (black) contours, for 2 degrees of freedom. Adapted from Belfiore et al. (2024).